RHEOLOGY OF HARD METAL PASTES

Alexander MEDINA PESCHIUTTA

Doctoral Programme in Physics and Materials Science

University of Luxembourg

This dissertation is submitted for the degree of Doctor of Philosophy

July 2024

A smooth sea never made a skilled sailor.

Franklin D. Roosevelt

DECLARATION

This dissertation is the result of my own work and includes nothing, which is the outcome of work done in collaboration except where specifically indicated in the text. It has not been previously submitted, in part or whole, to any university of institution for any degree, diploma, or other qualification.

Alexander MEDINA PESCHIUTTA

CONTENTS

List of Tables

List of Figures

List of Abbreviations and Acronyms

Abbreviation	Meaning
B	Bagley
BB	Benbow-Bridgwater
BET	Brunauer–Emmett–Teller
BVC	Binder volume concentration
$BVC_{intercept}$	Binder volume concentration intercepts
CBVC	Critical binder volume concentration
$CBVC_{theo}$	CBVC determined with the theoretical calculation
$CBVC_{titra}$	CBVC determined with the titration method
$CBVC_{Reddy}$	CBVC determined with Reddy's model
$CBVC_{P0}$	Zero-pressure CBVC, determined by the uniaxial die method
$CPVC$	Critical particle volume concentration
n.d	Not defined
PM	Powder Metallurgy
RTP	Ready-To-Press
SEM	Scanning electron microscopy
WC	Tungsten carbide
W_2C	Tungsten semicarbide
WC-Co	Tungsten carbide cobalt hard metal
WR	Weissenberg–Rabinowitsch

Roman	Meaning
A	Die cross sectional area (view from top)
C	Heat adsorption parameter
D	Capillary diameter
d_{10}	Fine particle size fraction (10th percentile)
d_{50}	Median particle size fraction (50th percentile)
d_{90}	Coarse particle size fraction (90th percentile)
$d_{[3,2]}$	Sauter mean diameter

E_L	Lost energy
E_S	Stored energy
F_c	Compression force
G	Modulus
G'	Storage modulus
G''	Loss modulus
h	Powder height in the cavity
h_0	Initial powder height in the cavity
h_t	Powder height in the cavity after certain compression time
K	Fluid consistency coefficient
K	Mixer filling factor
L	Capillary length
L_0	Barrel length
m	Sample mass inserted in cavity for compression
m	Exponential coefficient to quantify velocity's influence on the capillary entry
$\mathrm{m}_{\mathrm{powder}}$	Powder mass used for mixing in the BRABENDER
n	Exponential parameter to quantify velocity's influence in the capillary
P	Driving pressure
P_c	Compression pressure in uniaxial die press
p_{entry}	Entry pressure effect from barrel to capillary
P_{ex}	Total extrusion pressure buildup in capillary rheometry
p_{raw}	Raw measured pressure
P/P_0	Relative pressure for BET measurement
P_1	Pressure drop from capillary entry effect
P_2	Pressure drop from capillary friction
P_3	Pressure drop from friction in the barrel
Δp	Pressure drop resulting from the material's resistance to flow through the capillary
R	Capillary radius
R_0	Barrel radius
v_{true}	True extrudate velocity in the capillary

v_{slip}	Velocity of the slip layer in the capillary
v_{raw}	Velocity in the capillary in the extruding direction
V	Volume
$\dot{V}$	Volumetric flow rate
$\dot{V}_{raw}$	Volumetric flow rate in the capillary
V_c	Control volume
$\text{V}_{\text{bowl}-\text{free}}$	Mixer container volume
X	Number of gas molecules adsorbed
X_m	the number of atoms to form a monolayer of nitrogen on the powder surface

Greek	Meaning
α	Multiplicative parameter to quantify velocity's influence on the capillary entry
β	Multiplicative parameter to quantify velocity's influence on the capillary entry
γ	Shear strain
$\dot{\gamma}$	Shear rate
$\dot{\gamma}_{aw}$	Apparent wall shear rate
$\dot{\gamma}_{slip}$	Shear rate of the slip layer in the capillary
$\dot{\gamma}_w$	Wall shear rate
$tan(\delta)$	Loss factor
η	Viscosity
$\eta_{\dot{\gamma}}$	Shear viscosity
η_{ε}	Elongational viscosity
$\lvert\eta^*\rvert$	Complex viscosity
η_a	Apparent shear viscosity
η_b	Organic binder viscosity
ϕ	Packing density
ϕ_m	Maximum packing density
λ	Flow behaviour index
ν	Kinematic viscosity

ρ_{tap}	Tap density
ρ_{pycno}	Pycnometer density
ρ_c	Compressed density
ρ_{P0}	Zero pressure density
σ_0	Initial bulk stress
τ	Shear stress
τ_{aw}	Apparent wall shear stress
τ_{true}	True shear stress
τ_0	Wall yield stress
τ_w	Wall shear stress

1 INTRODUCTION

Hard metals, also known as cemented carbides, are a class of materials that possess exceptional hardness, strength, and wear resistance. The hard phase is made of tungsten carbide (WC) or other carbides and the soft phase consist of cobalt, iron, or nickel, which act as metallic binding agents that keep together the hard phase. For WC-Co grades, the cobalt content ranges from 3-13 wt% for cutting tools and up to 30 wt% for wear parts. The high hardness of the tungsten carbide hard metals makes them a common choice for metal cutting applications such as replaceable cutting tool inserts, saw tips, drill bits, and end mills. Their high strength and wear resistance make them ideal for use in mining and drilling equipment or even in the aerospace industry due to the stability of their mechanical properties at high temperatures [1].

The tungsten carbide (WC_2) was discovered by Moissan melting tungsten with carbon in an arc furnace back in 1893 [2] and Schröter patented the procedure for fabrication of hard metal alloys in 1923 [3]. Today, the manufacturing of tungsten carbide tools follows the powder metallurgy (PM) process where tungsten carbide and a metallic binder (in powder form) are blended and compacted to create a green compact. The compact is then sintered in a furnace, causing the metallic binder to melt. This promotes the tungsten carbide grains to undergo solid-state diffusion, which leads to the formation of a composite material [1].

The production of tungsten carbide starts with mining tungsten (W) from ores. Thirteen W bearing ores are available, the most common being Wolframite, Scheelite, Ferberite, and Hubnerite. Some of these ores undergo a wet process that includes dissolution in hydrochloric acid to remove calcium and precipitate tungstic acid (H_2WO_4). The tungstic acid is dissolved in ammonium hydroxide and crystallised as ammonium tungstate ($(NH_4)_2WO_4$), which then is boiled to produce ammonium paratungstate (APT) [1].

APT undergoes calcination to yield either tungsten yellow oxide (WO_3) or tungsten blue oxide ($WO_{2.9}$). Following this, reduction under a hydrogen atmosphere at approximately 800 °C is conducted to obtain pure tungsten (W) powder. Essential parameters in this stage include temperature, time, hydrogen flow rate, humidity, and the introduction of doping elements like Na and K. The careful control of these factors allows for the regulation of tungsten carbide grain size within the range of approximately 1 to 20 μm [4].

Moving forward, tungsten and carbon are meticulously combined and subjected to heating at around 1500 °C in a hydrogen environment, forming tungsten carbide powder (WC). The carbides are now mixed in an attritor mill with the metallic binder (cobalt, nickel, or iron) and organic binders like paraffin or polyethylene glycol in the presence of a solvent (water, alcohol, or acetone) forming a slurry. This step significantly influences the carbide grain size and slurry homogeneity [4].

The slurry is then sprayed dried to evaporate the solvent and form Ready-To-Press (RTP) granules. The RTP is a spherical and homogeneous agglomerate of WC, metallic and organic binder. The spherical shaped granules give the powder superior flowability. The green part is shaped via uniaxial die pressing or isostatic pressing [1][4]. The shaping via extrusion or injection moulding requires an increased quantity of organic binder to create a paste; this process is covered in detail in the present work.

The green parts, resulting from shaping, undergo de-binding under a protective hydrogen atmosphere at temperatures ranging from 150 to 300 °C. Following de-binding, the parts are heat-treated under an inert atmosphere at approximately 700-1000 °C, producing the "brown part" which has mechanical properties similar to those of chalk [1][4].

In some cases, "brown" compacts are subjected to soft machining into the desired shape before sintering. Conventional machining methods such as turning, grinding, milling, and drilling are utilized. The subsequent sintering process, conducted at around 1350-1600°C, aims to produce a high-strength and non-porous material. The sintering process involves the formation of a eutectic to consolidate the composite, during sintering the compact experience a volume reduction of 45-60% driven mainly by particle rearrangement and capillary forces [1][4].

Hot isostatic pressing (HIP) can be utilized for parts that have already undergone sintering. This involves applying high pressures of around 50 to 150 MPa and temperatures of about 1300-1500 °C to eliminate residual porosity, as porosity negatively affects transverse rupture strength among others and is undesirable for applications requiring a critically polished surface. A more efficient process, known as 'Sinter/HIP,' performs simultaneously the last two steps, and the required pressures are lower (6 to 10 MPa) [1][4].

While some parts may be ready for delivery, others require machining to achieve final dimensions. However, the cemented carbide material is extremely hard at this stage, necessitating methods such as diamond grinding, electrical discharge machining, or similar approaches to attain the final desired tool shape [1][4].

The present thesis is conducted in collaboration with CERATIZIT Luxembourg S.`a r.l.. A company specialized in the development and manufacturing of hard metal cutting tools and wear parts.

The purpose of this project is to develop a detailed understanding of the physics of hard metal paste. Various pastes, produced with different tungsten carbide (WC) grain sizes and varying cobalt quantities, were studied. The focus of the thesis was a paste composed of nano-grain size powder, used by the industrial partner to produce water jet nozzles via extrusion. The small grain size and minimal metallic binder content characteristic of this system pose challenges for manufacturing and characterization.

The aim of this thesis is twofold. First, it aims to provide a detailed characterization of the paste constituents, study the main parameters affecting paste flow properties, and identify constitutive physical models describing the flow of hard metal pastes. Second, it seeks to implement the findings and transfer the gained knowledge to enhance the processing of these systems in an industrial context.

2 BACKGROUND

2.1 Paste processing in powder metallurgy

Two primary routes for shaping in powder metallurgy are available: direct shaping of the ready-to-press powder or the creation of a paste that facilitates shaping (Figure 1, top). Each route has its distinct advantages and drawbacks. Notably, pastes offer the benefit of enabling injection and extrusion techniques. Injection allows for producing parts with intricate shapes, while extrusion provides a cost-effective technique to manufacture components with regular cross-sections [5]. Figure 1 (bottom) shows an example of products produced by the industrial partner for each shaping method.

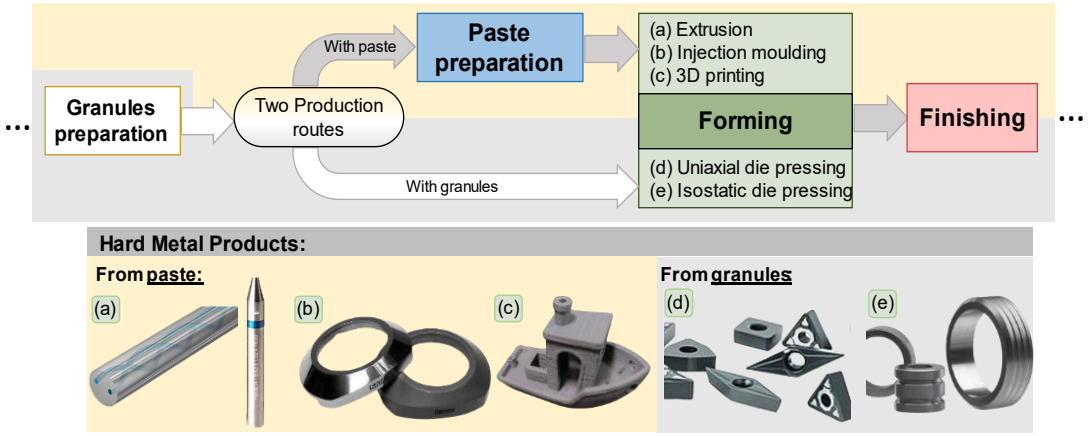

Figure 1: (top) General overview of CERATIZIT Luxembourg S.`a r.l. shaping routes, and (bottom) hard metal products shapes via each route (a) drill blank with helical cooling channels, (a) water jet nozzle, (b) watch case, (c) 3Dbenchy, (d) cutting inserts and (e) hot rolling dies. Product images provided by the industrial partner.

Is it truly necessary to formulate a paste for processing metallic and ceramic powders through extrusion or injection? Consider polymers with high melting points, such as polytetrafluoroethylene (PTFE); attempting to process it as a melt is impractical due to its

high melting temperature (approximately 342 °C) and melt viscosity of about 10 GPa.s. However, creating a paste by mixing PTFE powder with a lubricant (organic binder) in concentrations typically ranging from 16 wt.% to 25 wt.% enables the processing of polytetrafluoroethylene at room temperature and low pressures [6]. Consequently, considering the technical and economic advantages of forming a paste for certain polymers, it becomes evident that for many metals and ceramics, which exhibit higher melting points and melt viscosities, paste processing stands as the sole viable means of shaping via extrusion and injection.

A paste is a material that behaves like a solid under small loads but flows like a fluid when subjected to larger forces. Typically, pastes are suspensions consisting of a solid or granular material (e.g., metal powder) and a fluid binder (e.g., viscoelastic paraffin or polymer). As shown in Figure 2, the paste is created by blending these two phases. The binder displaces the air between powder particles during high-shear mixing to form a cohesive paste [5].

A binder typically comprises at least three components. The backbone, or major component, is crucial for preserving the part's geometry after shaping and ensuring structural integrity. A lower molecular weight filler, or minor component, occupies the space between particles and can be extracted before the backbone, aiding in channel creation to reduce internal stresses during the de-binding of the backbone. Additionally, various additives are incorporated to adjust viscosity, lubricate tooling, enhance binder-powder wetting, and inhibit crystallization during cooling [7–9].

Several factors influence the final properties of a paste, including powder characteristics, binder properties, powder-binder interactions, mixing techniques, and the powder-binder ratio [10,11]. The binder serves primarily to facilitate processing methods such as extrusion or injection moulding. To minimize shrinkage of the produced parts after binder removal, it is desirable to use the least amount of binder necessary for effective processing.

It is essential to recognize that the primary function of the organic binder is to maintain cohesion among the powder particles after the shaping process. The binder serves as a load carrier from the green to the brown stage, aiding in the accurate shaping of a defect-free part. Subsequently, the binder is eliminated, and the composition of the final part consists solely of consolidated (via sintering) metallic or ceramic powder material [5]. The transitory role of the binder in the final product does not make it less important; rather, its characteristics are pivotal for achieving a flawless outcome since the binder is the component which enables the powder to transform from a loose bulk to a malleable material.

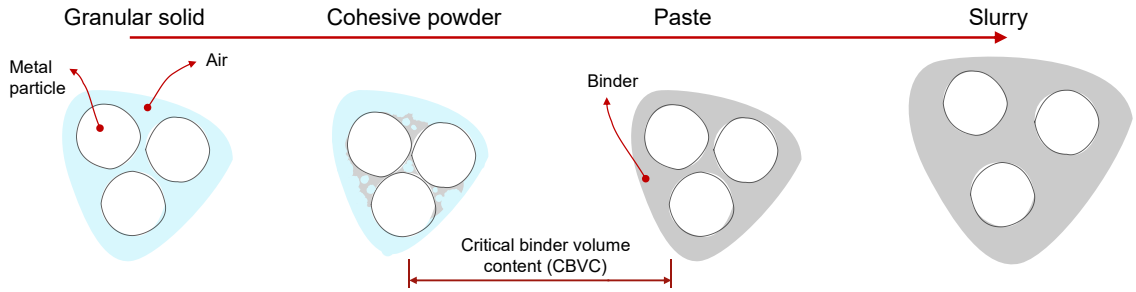

Figure 2: Schematic representation of the paste formation process as the organic binder content increases [5].

Various shaping techniques, including extrusion, injection moulding, and extrusion-based additive manufacturing (EBAM), demand specific binder properties for successful processing. Here, the primary requirements for each technique are outlined. [5].

In extrusion, maintaining the stability of the part's shape after exiting the die is crucial. This necessitates that the paste does not flow under the influence of gravitational forces. For injection moulding, the paste requires low viscosity with a shear-thinning behaviour, allowing it to fill the smallest corners of the mould cavities. Moreover, reducing the mould temperature during the holding time aids in solidifying some components of the paste, facilitating extraction by diminishing sticking forces with the mould.

In the case of extrusion-based additive manufacturing, the small size and mechanical constraints of the extruder demand a low-viscosity paste to flow through reduced-diameter nozzles (0.3 to 0.8 mm). Additionally, the paste must exhibit controlled spreading after being deposited on the printer bed, maintaining its shape without inducing surface defects. Furthermore, it must adhere to the subsequent layer, utilizing the thermal heat of the freshly extruded material [12]. For filament-based extrusion techniques, the paste must have some flexibility at room temperature to allow the filament to be spooled and fed to the extruder mechanism without breaking [13].

2.2 Aspects affecting paste properties

The characteristics of the paste are primarily influenced by the properties of the powder, the binder, and their interaction [14]. While the powder's composition is generally determined by the specifications of the final product, the binder's formulation gives the possibility to adapt the paste properties to the processing requirements.

Powder characteristics significantly influence paste behaviour: smaller particles increase paste viscosity and enhance detail resolution in injection moulding, as demonstrated by Ammosova et al. [15], who observed sharp edges on micropillars of 50 µm size only when using a feedstock with 10 µm powder particles; larger particles 22 µm resulted in rounded pillars edges. Gonzalez et al [12] argue that spherical powder particles are preferable since

they allow for the integration of higher powder loadings to the paste without substantially raising viscosity or reducing flexibility in the green state.

In selecting a binder, critical considerations include ensuring it does not affect the powder's inherent properties (e.g., oxidation). It should also facilitate precise geometry replication by the powder in the mould or die, enable the shape to be preserved during handling, and allow for straightforward removal during the de-binding process without causing defects. In industry, a wide range of binders are used such as water, cellulose, waxes, and polymers, which are often enhanced with additives like surfactants, plasticizers, and emulsifiers [5].

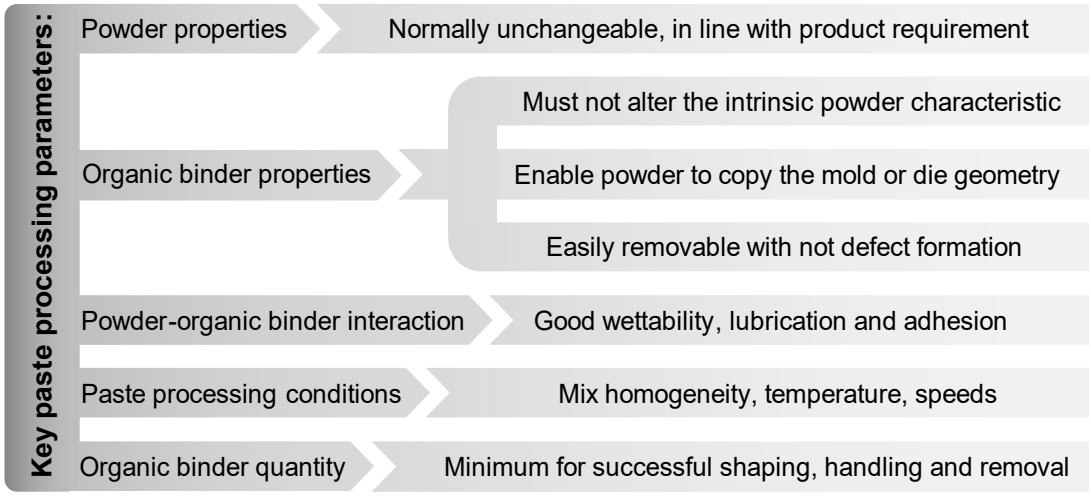

Figure 3: Key parameters for paste development.

Determining powder-binder compatibility is crucial for optimizing paste processing, primarily through evaluating binder wettability and penetration into the powder [12]. The powder-binder interaction depends on the polarity contrast between the powder, which is typically polar, and the commonly used non-polar polymers or paraffines. This polarity mismatch necessitates the employment of surfactants to mediate interactions and enhance compatibility [13]. Hanemann et al. [16] demonstrated by the usage of loading curves that surfactants significantly reduce the viscosity of ceramic powder mixtures, facilitating the compounding of feedstocks with higher solid loadings. Their findings highlighted that surfactants with shorter fatty acid chains (e.g., lauric acid) more effectively decrease viscosity at increased concentrations compared to those with longer chains (e.g., behenic acid). Additionally, they mentioned that the effect of surfactant on feedstock rheology becomes increasingly pertinent as powder grain decreases and approaches sub-micron size.

The backbone is one of the main components in paste formulation, its role is to maintain the structural integrity of the part until its removal. Therefore, having a backbone with a strong adhesion to the powder would enhance effective processing. Inadequate adhesion can cause the powder and organic binder to separate during processing, weakening the interface and degrading the feedstock properties. This separation is particularly problematic in highly

filled composites for Powder Injection Moulding (PIM) and Fused Filament Fabrication (FFF), where it can cause process failures. Examples include filaments with insufficient mechanical strength for FFF machines, compositional inhomogeneities in complex geometries for PIM or phase separation [13].

An innovative method to improve this adhesion involves polymer grafting, a process that chemically attaches molecules that are compatible with the powder (e.g., maleic or acrylic acid) to the polymeric backbone. A notable advantage of grafted polymers over using fatty acids is that the last ones tend to degrade at processing temperatures (creating bubbles in the part) and can present phase separation as the formation of entanglements with other polymers would be low due to their short chain length, which in turn could lead to defects in the part or a process that is difficult to control in an industrial scale.

Cano et al.'s [13] research on nanoparticles demonstrates that polymer grafting significantly improves the adhesion and dispersion of the binder on the powder surface leading to a notable increase in viscosity and mechanical properties of the filament and green part.

Bek et al. [11] studied the effect that organic binder has on the rheology of four powder systems with similar particle size and shape but different chemical nature (Al, 316L, Ti and glass beads). Their research revealed that feedstocks forming chemical bonds between the powder and binder exhibit more uniform flow properties and higher storage modulus than those relying solely on physical interactions. This underscores the significance of increasing binder-powder adhesion through methods such as fatty acid incorporation, polymer backbone grafting, or powder surface coating with silanes. These techniques enhance powder dispersion within the binder, elevate viscosity, and diminish powder agglomeration, which in turn results in green parts with improved strength and flexibility.

The binder content in the paste is a critical factor, as using the minimal amount necessary for defect-free shaping and handling minimizes shrinkage during sintering [7]. While more binder decreases viscosity, it can cause deformation during sintering, whereas too little may result in post-sintering voids.[15]. Gonzalez et al [17] studied gas atomized steel feedstocks with varying powder content (50-60 vol.%), finding that higher powder concentrations (around 60vol%) resulted in extrudates more closely matching the die dimensions, as increased binder content reduced die swell. Additionally, elevated binder levels correlated with increased carbon content in sintered components, subsequently influencing the hardness of the final product.

One common method to optimize binder content in ceramics and powder metallurgy is by determining the critical binder volume concentration ($CBVC$). This parameter has been established through various techniques for materials such as alumina [18–20], kaolin and

alumina [21], zirconia [22], zirconium silicate [23,24], stainless steel [22,25–30], gas atomised Invar 36 alloy [31,32], bronze and Inconel [33–35], carbonyl iron [36], titanium [37,38], tungsten carbide [39–45] and other feedstocks. Section 4.2 introduces this parameter in detail and presents several methods for its determination.

2.3 Rheology

Rheology is the branch of physics and materials science studying the flow of matter. In this context, 'flow' means the deformation of fluids or solids due to external stress. To conduct rheological studies, one must apply a controlled stress to a sample and measure its response or vice versa. With rheological studies, properties such as viscosity, frequency or temperature-dependent shear moduli for a wide range of materials or substances can be investigated.

Figure 4 depicts the viscoelastic spectrum of condensed matter, where materials exhibiting either ideal-liquid (yellow) or -solid (blue) characteristics are at the extremes, while those in between demonstrate viscoelastic behaviour (red), combining liquid and solid attributes. This classification depends on how these materials respond to external stress over time.

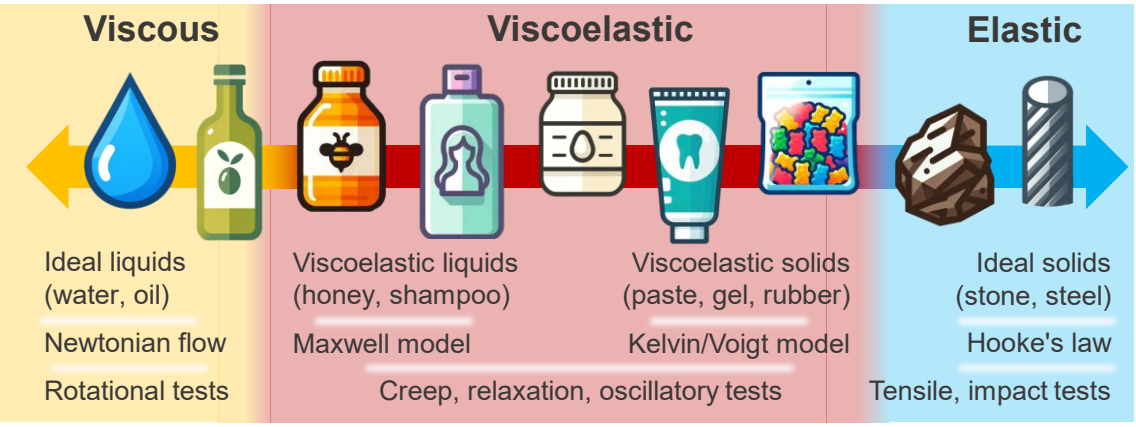

Figure 4: Condensed matter. The viscoelastic spectrum. Adapted and redrawn from [46–48].

In Figure 5 (colour-coded like Figure 4), three scenarios of a material falling by the effect of gravity are portrayed. In the case of a liquid, represented by immediate spreading upon impact (viscous behaviour), all the energy from the fall is rapidly dissipated. In contrast, the viscoelastic material has some resistance to the impact, gradually dissipating the energy while flowing under a gravitational load. The solid also undergoes some degree of deformation upon impact, preventing it from returning to its initial height. This indicates that part of the energy is lost as heat (E_L), but not all energy is lost, causing it to reach a certain height proportional to the energy stored elastically in the material (E_S). The stored energy will keep it bouncing until it is completely dissipated.

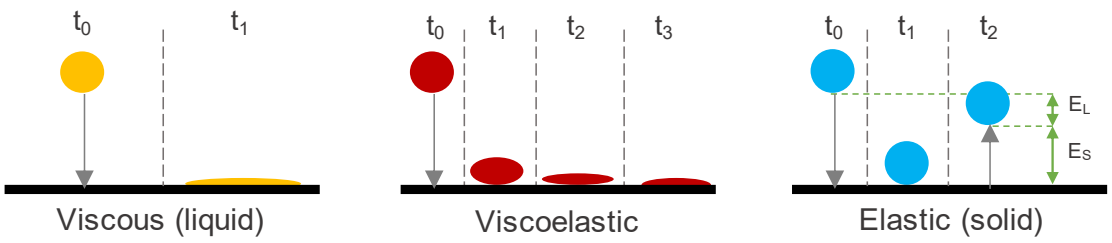

Figure 5: Depiction of viscous, viscoelastic, and elastic characteristics. Illustrates the concept of immediate relaxation in a Newtonian fluid and the time-dependent relaxation in a fluid exhibiting both elastic and viscous properties. Adapted and redrawn from [49], colour-coded like Figure 4.

Illustrative examples of materials exhibiting ideal liquid and solid characteristics at room temperature include water and steel. Visualize a Newton's cradle constructed with steel balls. Due to the steel's molecules resisting plastic deformation, the energy is transferred from one ball to the next, causing the last one to reach the same height as the first ball. Conversely, water behaves as an ideal liquid; its molecules are free and easily deformable, promptly dissipating energy after stress.

The modulus (G) describes the resistance to deformation (Eq. 1). In the example of the solid bouncing, the energy lost due to internal frictional mechanism corresponds to the loss modulus (G'') and the stored or elastic response to the storage modulus (G') [48]. These two components allow the classification of a material as more "solid-like" or "liquid-like". Introducing the concept of G' and G'' leads to introducing a variable called the loss factor (Eq. 2). This factor describes how effectively a material dissipates energy and is defined as the ratio of the loss modulus to the storage modulus.

$$G = \frac{Shear\ stress}{Shear\ Strain} = {}^{\tau}/_{\gamma} \qquad \textbf{Eq. 1}$$

$$tan(\delta) = \frac{G''}{G'} \qquad \textbf{Eq. 2}$$

In rheology, materials are analysed as continuous masses rather than discrete parts. This perspective assumes that the substance in the bulk is continuously distributed, filling the entire space it occupies. Consequently, there is an implicit assumption that the bulk material lacks cracks, discontinuities, or spaces between atoms. In this context, a continuum is a body that can be continually subdivided into infinitesimal elements, reflecting properties consistent with the bulk material. Rheology investigates materials on a larger scale, treating them as continuum bodies subject to external forces [50].

The study of such materials involves three fundamental equations to characterize the flow in isothermal conditions [50]:

- Momentum conservation (equation of motion)
- Mass conservation (continuity equation)
- Deformation-stress relationship (constitutive equation of the material)

The rheological behaviour of a substance depends on several external factors. Key considerations encompass the way external forces or deformations are applied, the preset deformation, velocity, or force magnitude. Additionally, the degree of deformation, whether occurring under low-shear or high-shear conditions and its duration, referring to the periods under load and at rest, play pivotal roles. Furthermore, temperature is a significant factor influencing rheological properties [48].

Viscosity (η) describes the resistance to flow and is the measure of the average internal frictional forces among the molecules and particles within a substance subjected to flow under the influence of external stress. To evaluate viscosity, an external stress is applied to the sample, and the response is measured in the form of strain or deformation. Depending on the type of experiment and stress type the viscosity is named differently, some examples are shear viscosity when a shear rate is applied to the sample ($\eta_{\dot{\gamma}}$), elongational viscosity for an elongational strain rate ($\eta_{\dot{\varepsilon}}$), complex viscosity for an oscillatory strain ($|\eta^*|$), or kinematic viscosity when the viscosity is divided by the density of the sample (ν) [48].

Numerous measurement techniques are available for studying rheological properties. These methods allow the application of a controlled stress to a sample and the measurement of its subsequent response or vice-versa. The selection of a specific technique depends on factors such as the required precision, budget considerations, the property under investigation (elastic or plastic response), and the needed test conditions (amplitude, frequency, or temperature dependency). It also hinges on the inherent characteristics of the sample, including whether it exhibits more solid or liquid-like behaviour, among other criteria.

One method that illustrates very well the idea of rheology is a simple finger test (Figure 6). This method involves placing a small sample between the thumb and index finger, repeatedly compressing, stretching, or pulling the sample until it breaks. While not considered professional or accurate in scientific terms, it provides a tactile sense of a sample's rheological properties. For instance, when testing a sample, it can be classified in various ways. A brittle sample will break into small pieces, while a buttery sample display several short peaks. A long fibre sample stretches out into a single or bundle of fibres similar to Figure 6 (left), whereas a short fibre sample shows a short break-off with evidence of fibres like Figure 6 (right), a stringy sample stretches into fine long threads and a resilient sample endure some degree of compression with no permanent deformation [48].

Figure 6: Tack and stringiness assessment using the finger test [51].

In the field of pastes, measuring devices like rotational rheometers, capillary rheometers, torque rheometers and microinjection devices are commonly used to characterize the flow properties. By changing the measuring geometry (capillary, blades, mould…), a wide range of samples can be assessed with each device.

2.3.1 Capillary rheometry

The first capillary viscometer, conceived in 1839 by hydraulic engineer Gotthilf H.L. Hagen, played a pivotal role in the research conducted by Dr. Jean L.M. Poiseuille on capillary flow of liquids such as water, alcohol, and blood. Through his investigations, Poiseuille discerned a correlation between pressure drop and volumetric flow rate. This relationship of viscosity (η) is derived from the ratio of wall shear stress (τ_w) to wall shear rate ($\dot{\gamma}_w$) has been recognized since 1925 as the Hagen-Poiseuille relation for Newtonian fluids [48].

A capillary rheometer resembles a pressure-driven extrusion process (Figure 7) enabling the measurement of viscosities at elevated shear rates (up to 5000 s^{-1}) [51]. The operational principle is straightforward: the sample is introduced into the barrel cavity, and upon melting the feedstock is forced through the die or capillary by a piston or ram. The piston speed and the pressure above the capillary are recorded.

With the pressure recorded by the pressure transducer located above the capillary (p_{raw}), the apparent wall shear stress (τ_{aw}) is determined following Eq. 3 where L is the capillary length and R the capillary radius. The shear stress is called apparent because some fluids present a non-homogeneous flow from the barrel to the capillary and to obtain the true wall shear stress (τ_w) the Bagley correction must be applied.

The wall shear rate is determined using the piston speed. Eq. 4 delineates the volumetric flow rate in the capillary ($\dot{V}_{raw}$) as the result of multiplying v_{raw} by the cross-sectional area for a cylindrical capillary, represented as πR^2. Here, v_{raw} is the material velocity in the capillary in the extruding direction, which is calculated using the piston speed by assuming that the volumetric flow rate in the barrel is equal to the one in the capillary. Following Eq. 5 the apparent wall shear rate is obtained. In this case, the term apparent is due to the

assumption of the velocity at the capillary wall to be zero. When this is not the case, the $\dot{\gamma}_{aw}$ must be corrected using the Mooney correction to obtain $\dot{\gamma}_w$.

Finally, Eq. 6 presents the ratio of the apparent wall shear stress (τ_{aw}) with the apparent wall shear rate ($\dot{\gamma}_{aw}$) and consequently the apparent shear viscosity (η_a). To obtain the true shear viscosity (η) for a non-Newtonian liquid τ_w and $\dot{\gamma}_w$ must be considered.

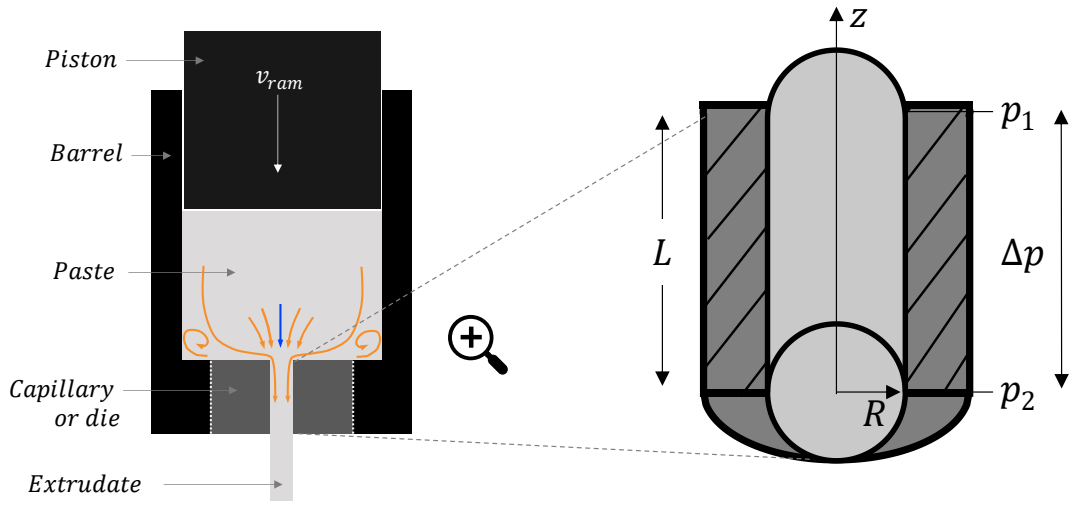

Figure 7: (left) Schematic representation of a capillary rheometer displaying key components. (right) Close-up of the capillary or die highlighting the main variables used in capillary formulas.

$$\tau_{aw} = \frac{p_{raw} R}{2L} \qquad \textbf{Eq. 3}$$

$$\dot{V}_{raw} = \pi R^2 v_{raw} \qquad \textbf{Eq. 4}$$

$$\dot{\gamma}_{aw} = \frac{4\dot{V}_{raw}}{\pi R^3} \qquad \textbf{Eq. 5}$$

$$\eta_a = \frac{\tau_{aw}}{\dot{\gamma}_{aw}} = \frac{\pi \Delta p R^4}{8 L \dot{V}_{raw}} \qquad \textbf{Eq. 6}$$

Eq. 3 and Eq. 5 are based on the following assumption [52]:

- Uniform pressure gradient along the extruding direction
- Fully developed, steady, laminar flow
- No velocity in the radial directions
- Zero velocity at the capillary wall
- Pressure independent viscosity
- Incompressible fluid (fluid volume does not change with pressure)
- Cylindric coordinate symmetry in the capillary
- Isothermal conditions

In capillary rheometry, adherence to specific assumptions is paramount due to the reliance on the principles outlined by Hagen-Poiseuille (Eq. 6). To ensure an accurate representation of material properties, particular attention must be directed towards the following considerations. As elucidated below, the impact of some influences on the experimental results can be minimized like [50,51]:

- Ensure minimal flow variation in the extrusion direction, achieved by maintaining a minimum L/D ratio of $10/1$ to have a fully developed velocity profile.
- Considerations of melt fracture, extrudate swell, accurate temperature control, and entrapped air require careful shear rate selection and meticulous experimental execution.
- Sample pre-compaction before extrusion can reduce the effect of pressure on viscosity and lead to a more uniform pressure gradient and flow conditions.

In contrast, some influences have to be considered by corrections throughout the experimental procedures like [50,51]:

- Capillary entry and exit effects caused by the non-homogeneous flow of the extrudate (addressed through Hagenbach or Bagley correction).
- Shear heating of the material in the capillary (requires dissipation correction).
- Presence of wall slip (addressed via Mooney correction).
- Assumption of a parabolic velocity profile, which applies to pipe flow of Newtonian fluids. However, non-Newtonian fluids exhibit a non-parabolic velocity profile, necessitating a Weissenberg-Rabinowitsch correction of the wall shear rate values.

The sequence in which these corrections are applied significantly impacts the outcome. GOTTFERT, a capillary rheometer manufacturer, suggests beginning with the Bagley correction for systems with viscosities exceeding 1 Pa·s (such as plastic and rubber), followed by the dissipation, Mooney, and Weissenberg-Rabinowitsch corrections. Alternatively, for systems with viscosities below 1 Pas, starting with the Hagenbach correction, followed by Bagley and Weissenberg-Rabinowitsch, is recommended [53]. However, an alternative recommendation is presented by Morrison [54], advocating for a different order: Mooney, Bagley, and Weissenberg-Rabinowitsch corrections.

When conducting experiments with a capillary rheometer, the capabilities of the rheometer, the available geometries, and the properties of the sample will limit the extent to which the rheological study can be performed. For instance, the highest shear rate that can be applied is influenced by both the rheometer's capabilities and the properties of the sample. The rheometer is limited by the maximum force and speed it can apply to the piston during the

test. This motion generates a pressure that is detected by a pressure transducer located just above the capillary, which also operates within its own specified measuring range and accuracy. Adjusting the L/R ratio of the capillary or selecting an appropriate transducer can often overcome the maximum limits of the measuring device. In contrast, the lower limit for the attainable shear rates is determined by the minimum speed that the machine can achieve and measure and the capillary radius (Eq. 5).

In practice, the highest attainable shear rates are often constrained by the intrinsic properties of the sample. Achieving steady flow conditions in the capillary is crucial for obtaining consistent flow curves. A practical guideline to minimize disturbances caused by capillary entry or exit effects is to use capillaries with a length-to-diameter ratio (L/D) greater than 10/1. However, even with an appropriate geometry, flow instabilities (such as sharkskin, slip- stick, drainage, die swell, etc.) tend to emerge at high shear rates, limiting the maximum shear rate that can be effectively recorded for a given sample [51].

In the literature, errors of 20-50% have been reported when using the Hagen-Poiseuille relationship for polymer melts without applying the Bagley and Weissenberg-Rabinowitsch corrections [51]. Consequently, uncorrected values for viscoelastic samples should be considered solely as comparative results and not as absolute rheological properties unless the required corrections are applied [53].

2.3.1.1 Bagley correction

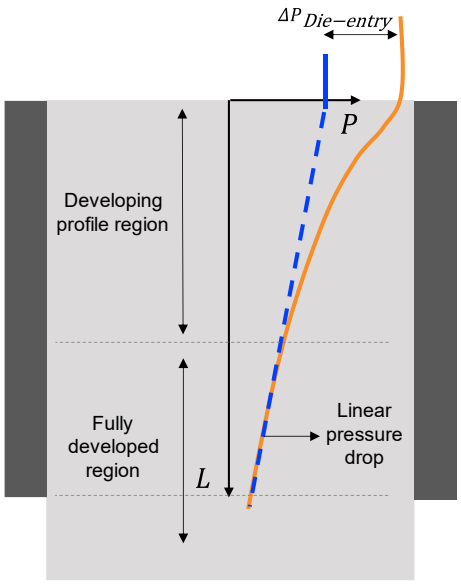

Figure 8: Close-up of capillary flow. Schematic illustrating the Bagley correction. Adapted from [50].

The true viscosity of a material should not depend on the L/R ratio of the capillary or die used for its determination. However, in the case of numerous materials, this assumption does not hold unless the Bagley correction is applied. This is partially caused by the pressure drop due to the non-homogeneous flow resulting from viscous or viscoelastic effects and the inertia of the melt as it travels from the barrel to the die and the pressure drop in the barrel itself. The later one can be neglected for most capillary rheometers since the barrel radius is substantially larger than the capillary radius, leading to a significantly lower paste velocity within the barrel [55]. The former one is addressed by the Bagley correction which assumes that the slip velocity is unaffected by pressure and maintains a constant value along the entire length

of the capillary [56]. The entry effect can be addressed by extruding the sample thought multiple dies (at least 2) with the same radius (R) but different lengths (L) and evaluating the pressure data in function of L/R.

The apparent wall shear stress (τ_{aw}) is determined using Eq. 3 where Δp represents solely the pressure drop resulting from the material's resistance to flow through the capillary. To obtain this, the pressure caused by the entry effect (p_{entry}) is subtracted from the measured pressure (p_{raw}), as per Eq. 7.

$$\Delta p = (p_{raw} - p_{entry}) = 2\tau_{aw}\frac{L}{R} \qquad \textbf{Eq. 7}$$

Rearranging Eq. 7 in the form of Eq. 8 facilitates the isolation of the term p_{entry}, which now can be determined from the intercept of the plot of the measured pressure (p_{raw}) as a function of the L/R ratio for each shear rate. The slope of the plot is equivalent to twice the apparent wall shear stress (τ_{aw}).

$$p_{raw} = \underbrace{2\tau_{aw}}_{Slope}\frac{L}{R} + \underbrace{p_{entry}}_{Intercept} \qquad \textbf{Eq. 8}$$

Finally, the wall shear stress (τ_w) is obtained using the corrected pressure drop ($\Delta p = p_{raw} - p_{entry}$) in Eq. 3, and from this recalculated value, the Bagley-corrected viscosity is determined.

2.3.1.2 Mooney correction

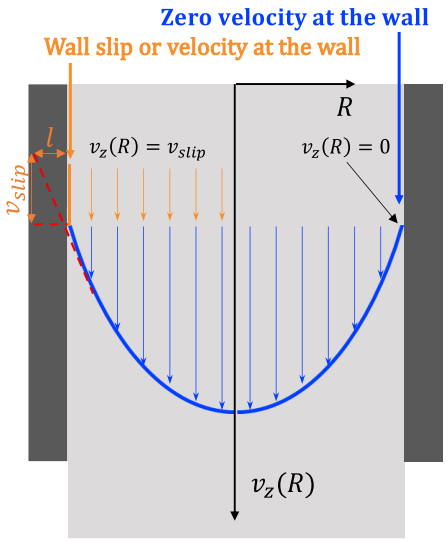

Figure 9: Close-up of capillary flow. Schematic illustrating the Mooney correction. Adapted from [50].

In the Hagen-Poiseuille relationship (Eq. 6), one assumption is the condition of zero velocity at the interface between the capillary and the material being extruded. However, this assumption does not hold universally, as some materials demonstrate a slip condition at the capillary wall (depicted in orange in Figure 9), leading to an overall higher flow rate. This effect can be advantageous for processing, as a lubrication layer at the capillary wall reduces frictional forces, acting as a lubricating effect and diminishing the likelihood of surface defects after exiting the die. Conversely, when precise material data is crucial for process control or simulation, it is essential to consider the contribution of slip during

the process, as it profoundly influences the boundary conditions for the description of the flow [56–59]

Mooney [60] suggests that wall slip could signify an exceptionally steep velocity gradient in a thin layer near the wall. This occurrence can be mathematically addressed as a discontinuity in velocity, i.e., slip, provided that the thickness of the layer is small in comparison to the capillary radius. By recording flow curves using capillaries with the same L/D ratio the volumetric flow rate can be measured maintaining a constant stress at the capillary surface. In this context, any unexpected alteration in wall shear rate ($\dot{\gamma}_w$) that is not related to Eq. 9 is attributed to wall slip and is independent of the material's viscous response.

Drawing upon Mooney's analysis, it can be affirmed that, in the context of capillary rheometry, a noticeable dependence of the flow curve on the capillary diameter strongly suggests the presence of wall slip [61]. The method unfolds as follows:

Eq. 5 can be alternatively expressed in terms of speed, as demonstrated in Eq. 9.

$$\dot{\gamma}_{\mathrm{aw}} = \frac{4\dot{V}_{raw}}{\pi R^3} = \frac{4v_{raw}}{R} \qquad \textbf{Eq. 9}$$

Hence, if the occurrence of wall slip is considered, the true velocity (v_{true}) or true wall shear rate ($\dot{\gamma}_w$) can be obtained by subtracting the slip-induced contribution from the measured wall shear rate ($\dot{\gamma}_{\mathrm{aw}}$), as indicated in Eq. 10.

$$\dot{\gamma}_{\mathrm{w}} = \dot{\gamma}_{\mathrm{aw}} - \dot{\gamma}_{\mathrm{slip}} \qquad \text{or} \qquad v_{\mathrm{true}} = v_{raw} - v_{\mathrm{slip}} \qquad \textbf{Eq. 10}$$

In line with Mooney's methodology [60] and referring to Eq. 11, creating a plot of the wall shear rate against the reciprocal of the radius for different capillary radii facilitates the assessment of slip contribution to the velocity from the slope and the determination of the true velocity from the Y-intercept. This method assumes a linear relationship between $\dot{\gamma}_{raw}$ and $1/R$; however, some researchers have observed instances where this approach is not universally applicable, indicating scenarios where the method fails to provide accurate values for v_{slip} for elastomers or pastes [62].

$$\underbrace{\frac{4\dot{V}_{raw}}{\pi R^3}}_{\dot{\gamma}_{aw}} = \underbrace{4v_{slip}}_{Slope}\frac{1}{R} + \underbrace{\frac{4v_{true}}{R}}_{Intercept} \qquad \textbf{Eq. 11}$$

2.3.1.3 Weissenberg-Rabinowitsch Correction

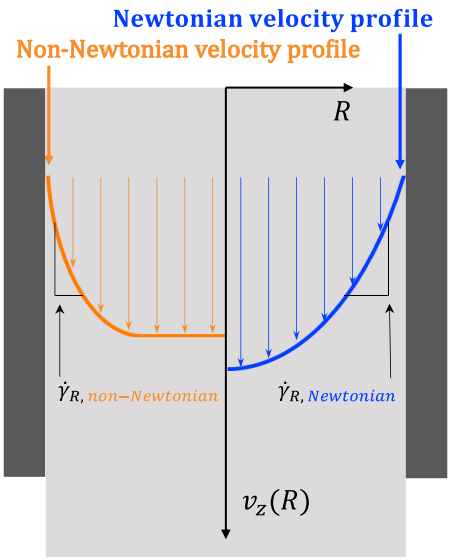

Figure 10: Close-up of capillary flow. Schematic illustrating the Weissenberg-Rabinowitsch correction. Adapted from [50].

The Weissenberg-Rabinowitsch correction (Eq. 12) enables the determination of the wall shear rate ($\dot{\gamma}_w$) without presuming the velocity profile characteristic for the Newtonian fluids. This correction becomes essential when dealing with non-Newtonian fluids, where the assumption of a parabolic velocity profile is invalid. Consequently, the shear rate derived from this non-parabolic profile is considered to be apparent ($\dot{\gamma}_{aw}$), signifying what it would have been if the fluid had conformed to Newtonian behaviour [50,52,63].

$$\dot{\gamma}_w(\tau_w) = \dot{\gamma}_{aw}\left[\frac{1}{4}\left(3 + \frac{dln\,(\dot{\gamma}_{aw})}{dln\,(\tau_w)}\right)\right] \qquad \textbf{Eq. 12}$$

According to Eq. 12, to determine the true wall shear rate ($\dot{\gamma}_w$) for a fluid, one must multiply the apparent shear rate ($\dot{\gamma}_{aw}$) by a factor obtained from the slope of the plot of the natural logarithm of the apparent shear rate ($ln\,(\dot{\gamma}_{aw})$) against the natural logarithm of the shear stress at the wall ($ln\,(\tau_w)$). Subsequently, a function with the form $y = ax^2 + bx + c$ can be fitted to the data to obtain the parameters a and b, from which dy/dx is obtained as depicted in Eq. 13. Is important to notice that for a Newtonian fluid, this factor becomes 1, indicating that $\dot{\gamma}_w(\tau_w) = \dot{\gamma}_{aw}$.

$$y = ln(\dot{\gamma}_{aw}) \qquad \text{and} \qquad x = ln\,(\tau_w)$$

$$y = ax^2 + bx + c \qquad \textbf{Eq. 13}$$

$$\frac{dy}{dx} = 2ax + b$$

2.3.2 Basic rheological models

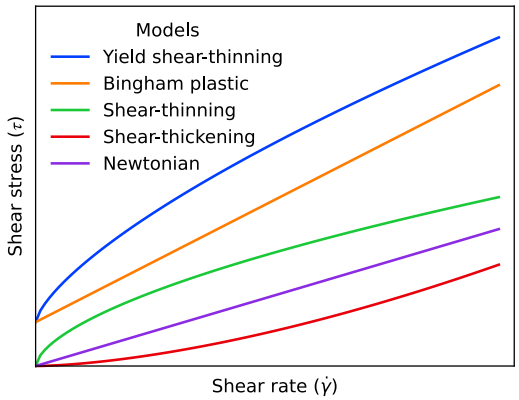

Figure 11: Models that describe flow in rheology. Adapted from [48].

We previously noted that material flow behaviour spans from that of ideal-viscous liquids to ideal-elastic solids, varying widely based on fluid properties, leading to numerous flow types. This diversity is captured in Figure 11, which shows different shear stress responses to shear rates in fluid modelling, as described by the Herschel-Bulkley model (Eq. 14) through adjustments in yield stress (τ_0), flow behaviour index (λ), and fluid consistency coefficient (K) a variety of flow behaviours can de described mathematically with this model [48].

$$\tau = \tau_0 + K\dot{\gamma}^{\lambda} \qquad \textbf{Eq. 14}$$

Ideal-viscous (Newtonian) liquids, like water, exhibit a direct, linear relationship between shear rate and shear stress, signifying a constant viscosity regardless of shear rate ($\tau_0 = 0 \; and \; \lambda = 1$). Shear-thinning fluids, such as polymers, show a decrease in viscosity with shear, as their long-chain molecules align to the flow direction, diminishing resistance and viscosity ($\tau_0 = 0 \; and \; \lambda < 1$). Conversely, shear-thickening substances, exemplified by a cornstarch and water mix, increase in viscosity under shear ($\tau_0 = 0 \; and \; \lambda > 1$) [48].

Substances like pastes, creams, or ketchup exhibit dual solid and liquid characteristics. They behave as solids until a critical yield stress is exceeded, beyond which they flow like liquids. Depending on whether their flow remains constant with shear rate changes or decreases, they are classified as Bingham plastics ($\tau_0 > 0 \; and \; \lambda = 1$) or yield shear-thinning ($\tau_0 > 0 \; and \; \lambda < 1$), respectively [48].

2.3.3 Benbow Bridgwater model

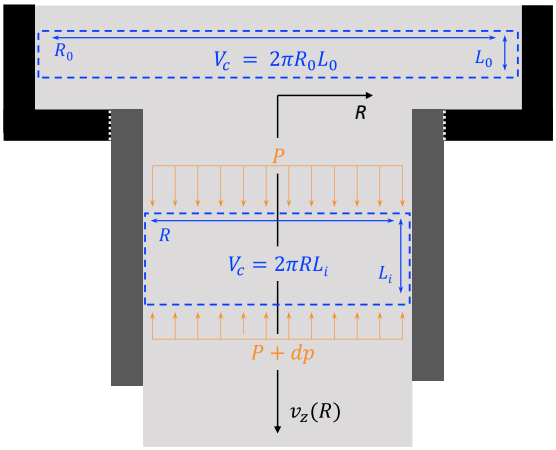

Figure 12: Close-up of flow from barrel to the capillary. Schematic illustrating a control volume for the Benbow Bridgwater model. Adapted from [64].

Benbow and Bridgwater developed a semi-empirical model for characterizing paste extrusion, assuming plug flow in the barrel and capillary with the paste treated as incompressible. The model attributes pressure buildup during extrusion (P_{ex}) to three primary factors (Eq. 15): capillary entry effect (P_1), friction in the capillary (P_2), and friction in the barrel (P_3) [65].

$$P_{ex} = P_1 + P_2 + P_3 \qquad \textbf{Eq. 15}$$

The capillary entry effect's pressure drop (P_1) is determined by equations for the work required to deform a control volume (V_c) from the barrel ($2\pi R_0 L_0$) to the die region ($2\pi R L_i$), assuming volume conservation and ideal work as depicted in Figure 12 in blue. Which means that P_1 neglects any non-uniform flow at the entry region. The work equations lead to Eq. 16, where P_1 is expressed as a function of the initial bulk stress (σ_0) and a velocity-dependent component ($\alpha {v_{raw}}^m$). The parameters α and m quantify the influence that velocity (v_{raw}) has on the capillary entry effect [64,65].

$$P_1 = 2\underbrace{(\sigma_0 + \alpha {v_{raw}}^m)}_{\sigma_y} ln\left(\frac{D_0}{D}\right) \qquad \textbf{Eq. 16}$$

The term for pressure drop from capillary friction (P_2) derived from a force balance, is shown in Figure 12 in orange. The driving pressure (P) encounters resistance from both the wall shear stress (τ_w) and the material friction ($P + dP$). In Eq. 17, τ_0 indicates the initial bulk yield shear stress, while β and n are empirical parameters that describe the velocity dependence of τ_w in the capillary region. The wall shear stress τ_w is considered to be pressure-independent, assuming a slip layer exists between the capillary and the extrudate [64,65]. Notably, the term $\tau_0 + \beta {v_{raw}}^n$ resembles the Herschel-Bulkley model (Eq. 14).

$$P_2 = 4\underbrace{(\tau_0 + \beta {v_{raw}}^n)}_{\tau_w} \cdot \left(\frac{L}{D}\right) \qquad \textbf{Eq. 17}$$

Caution has to be taken when interpreting the static parameters (σ_0 and τ_0) as they are derived from extrapolations of dynamic measurements [65,66]. The pressure drop is attributed to the friction of the paste flowing in the barrel (P_3) is considered to be negligible, this is especially true when the barrel diameter is much larger than the capillary diameter

(10:1 ratio). Additionally, the contribution of P_3 tends to be minuscule compared to the other two pressure drops. For more details on the derivation of equations Eq. 18, see references [64,65].

$$P_{ex} = 2\underbrace{(\sigma_0 + \alpha {v_{raw}}^m)}_{\sigma_y} l\, n\left(\frac{D_0}{D}\right) + 4\underbrace{(\tau_0 + \beta {v_{raw}}^n)}_{\tau_w} \cdot \left(\frac{L}{D}\right) + 0 \qquad \textbf{Eq. 18}$$

Replacing each pressure term of Eq. 15 results in the six-parameter Benbow-Bridgwater model (Eq. 18). This model contains parameters describing the flow from the barrel to the capillary (σ_0, α, m) and the flow through the capillary (τ_0, β, n). The model accounts for the dependency of viscous terms on extrusion rate and it was found to be effective for pastes with high molecular-weight polymer as an organic binder [65]. Additionally, it has been successfully used to characterize hard metal pastes containing particles approximately 1 µm in size, utilizing wax and alcohol binders [66][67].

For materials where the pressure increases linearly with velocity, the model can be simplified to a four-parameter version, by setting the power law terms m and n to 1. This simplified model is particularly useful when the viscous components are minimal. Its simplicity and ease of use make it advantageous for characterizing various formulations, such as assessing the impact of different liquid phase concentrations on the flow properties of pastes [65].

The six parameters can be interpreted as follows: A high bulk yield stress (σ_0) indicates that the paste requires greater force to initiate extrusion, suggesting a stiffer paste that exhibits greater material compaction before extrusion, which can enhance dimensional accuracy. Conversely, a high wall shear stress (τ_0) suggests significant friction at the die wall, indicative of poor lubrication properties of the feedstock, which could cause surface defects. High values of α, β, m, and n signify that the paste's behaviour is highly dependent on velocity, affecting its flow characteristics through the capillary [63].

To evaluate the paste using this model, a capillary rheometer equipped with three dies of identical diameter (D) but varying lengths (L) should be used across at least five extrusion speeds (v). The total extrusion pressure (P_{ex}) versus L/D plots enable extraction of the entry pressure (P_1) component from the y-intercept at each speed, effectively simulating a die of zero length as L/D approaches zero. This approach isolates the entry effect from the overall measured pressure. Once P_1 is identified, P_2 can be determined by subtracting P_1 from the total extrusion pressure (P_{ex}), as outlined in Eq. 15.

3 METHODS AND MATERIALS

3.1 Density measurements

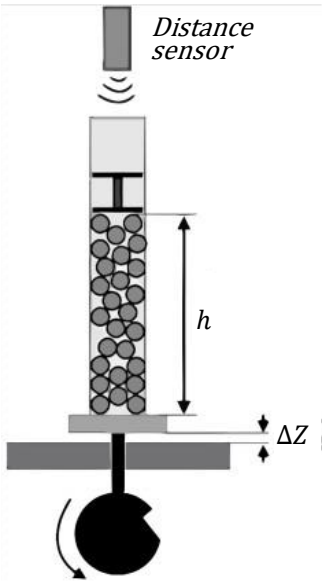

Figure 13: GRANUPACK measuring principle for apparent and tap density [68].

The GRANUPACK instrument by GRANUTOOLS is an automated device designed for the precise characterization of both tap and apparent densities of powders. The tap density is defined as the maximum packing density achievable under conditions of tapping or vibration, illustrating how closely particles can pack together under such external forces. Conversely, apparent density is measured without any external forces applied, relying solely on gravity, and reflects the loose packing of the powder.

Figure 11 shows a schematic diagram of the device and measuring principle. Where h is the initial powder height and ΔZ the tapping height.

The tap density is determined as follows: 35 ml of powder is gently introduced into a cylindrical vessel maintaining a loose fill. This ensures that the measured apparent density accurately represents the powder's natural state without compression. A metallic disc (double T shape), with a specific weight, is then placed atop the powder within the cylinder. This disc acts not only as a lid to guarantee a flat top surface but also as a compacting agent under the action of the device's tapping mechanism. Then, the device is set to a tapping height of 1 mm, with a total of 500 taps applied. This standardized tapping protocol ensures consistency across measurements. As the apparatus performs its tapping sequence, it records the diminishing volume of the powder as it

compacts, reaching a stable density state. The apparent density is calculated based on the initial volume of the powder, while the tap density is determined using the final compacted volume after the tapping process. By dividing the volume by the sample mass, the respective densities are obtained.

The AccuPyc II 1340 helium pycnometer by MICROMERITICS enables the determination of the true volume and pycnometer density of samples. The underlying principle of this technique is the ability of helium atoms, owing to their minuscule size, to infiltrate the smallest pores within a material, facilitating the determination of the true volume of a sample. It is important to note that this method specifically measures the volume accessible to helium, thereby excluding the volume of closed pores from its calculation. The pycnometer density is derived by dividing the mass of the sample by this measured true volume.

The pycnometer density is determined as follows: a predefined mass of powder (approximately 20 mg for hard metals) is filled into the measuring cup and then accurately weighed. The cup is positioned inside the sample chamber and the device initiates its measurement cycle by introducing helium into it, continuing until an equilibrium pressure is reached. The gas is then expanded to the extension which has a known volume. As shown in Eq. 19, the sample volume is obtained with the pressure difference and volume of each chamber.

$$V_{sample} = V_{sample\ chamber} - \frac{V_{expansion\ chamber}}{\frac{P_{sample\ chamber}}{P_{expansion\ chamber}} - 1} \qquad \textbf{Eq. 19}$$

The helium filling process is repeated multiple times to ensure consistency and reliability in the measurement outcomes. The pycnometer then calculates the average volume from these cycles and, by extension, the pycnometer density of the sample, providing these results along with their standard deviation. In both methodologies outlined in this section, the accuracy of weighing is crucial. Consequently, a high-precision balance with a readability of 0.1 mg was always utilized.

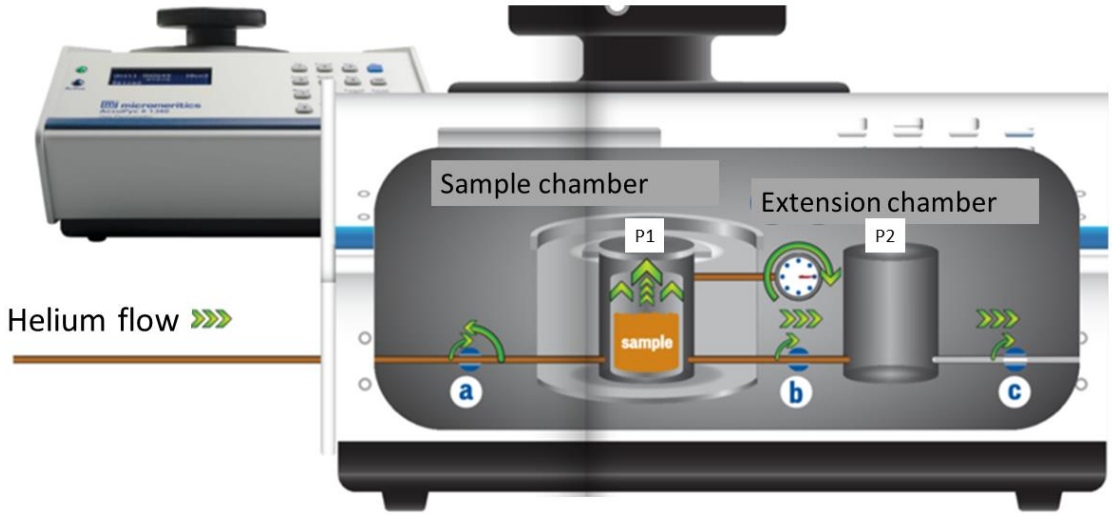

Figure 14: AccuPyc II 1340 helium pycnometer, measuring principle [69].

3.2 Laser diffraction

The grain size distributions of the selected WC powders were measured using laser diffraction. This was carried out with a particle size analyser, the 1090 model from ANTON PAAR (formerly CILAS). The measurements were performed in a liquid medium (distilled water) and the samples were dispersed using an ultrasound to minimize the potential for agglomeration.

Figure 15 shows a schematic representation of the measuring device. The technique is based on the principle that the angle at which the laser beam is diffracted by a particle is directly related to the particle's size. The diffracted laser light is directed to the detector via a series of lenses resulting in a specific intensity diffraction pattern. In the present, the Fraunhofer theory is applied to relate the relative intensity and diffraction angle to a particle radius. This theory assumes particles are spherical and does not account for absorption, refraction, reflection, or scattering of light. Additionally, this mathematical model does not require specific sample information for implementation and works best for opaque samples. This methodology produces a curve that classifies particles into specific size classes based on the volume percentage of particles in each class [70][71].

Key parameters such as the d_{10}, d_{50}, d_{90} and $d_{[3,2]}$ diameters are derived from the curve bellow and their meaning will be explained in the following. The first three represent the diameters below which 10%, 50%, and 90% of the particle sizes fall, in a polydisperse distribution. These metrics provide a comprehensive understanding of the particle size distribution, offering insights into the range and skewness of the particle size distribution.

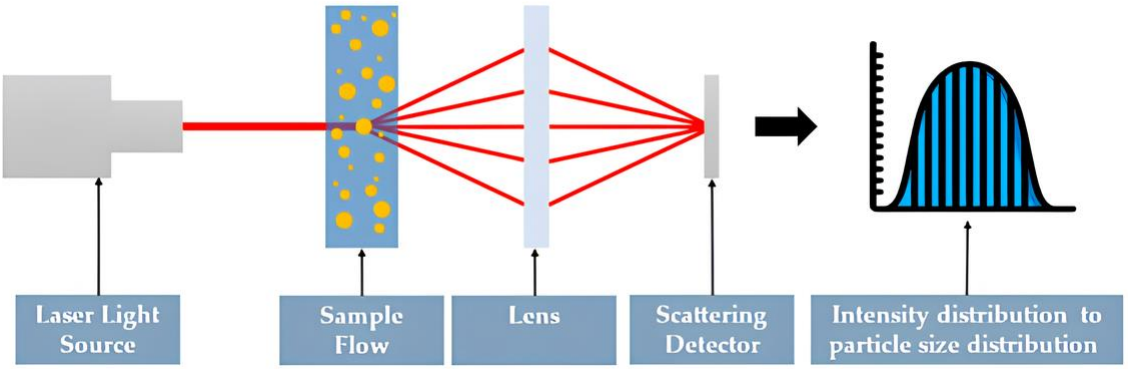

Figure 15: Schematic representation of the laser diffraction for particle sizing [71].

Furthermore, the Sauter mean diameter ($d_{[3,2]}$), representing the volume-to-surface mean diameter of a polydisperse distribution, can be calculated from the size distribution data. The concept behind $d_{[3,2]}$ is to hypothetically transform a polydisperse powder into a monodisperse by adjusting the number of particles while maintaining the total volume, surface area, and energy of the system constant. This powder property is particularly sensitive to the presence of larger particles in the distribution. As a volume-based mean diameter, where the volume of a particle increases with the cube of its diameter, larger particles contribute significantly more to the total volume than smaller particles [72].

$$d_{[3,2]} = \left(\frac{\sum {d_i}^3 \, n_i}{\sum {d_i}^2 \, n_i}\right)^{\frac{1}{3-2}} \qquad \textbf{Eq. 20}$$

3.3 Specific surface area

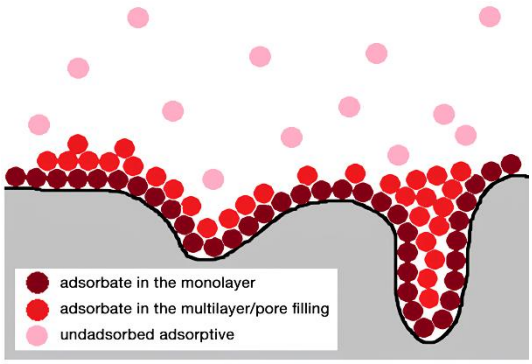

Figure 16: Formation of a monolayer of adsorbate (nitrogen) on the powder surface for BET determination [73].

The Brunauer-Emmett-Teller (BET) method provides information about the specific surface area per unit mass of a powder. The larger the BET values, the larger the surface area and therefore the higher the reactivity. In this study, the BET value was determined using the gas absorption technique, specifically with nitrogen gas. This method involves the adsorption of nitrogen gas molecules onto the surface of the powder particles under controlled conditions. By measuring the amount of gas adsorbed, the total surface area of the powder is obtained [74]. The instrument used for this purpose was the NOVATOUCH LX2 from ANTON PAAR.

The link between the number of gas molecules adsorbed (X) in the powder surface at a given relative pressure (P/P_0) is denoted by Eq. 21. In this relationship X_m represent the number of atoms to form a monolayer of nitrogen on the powder surface and C a heat adsorption parameter. Assuming that within a certain range of relative pressures, the term y behaves linearly in function of x, the surface area (in m^2/g^{-1}) can be determined by dividing the cross-sectional area of the adsorbate (16.2 $Å^2$ at 77 K for nitrogen) by the sum of the slope plus intercept of Eq. 21 [74][73].

$$\underbrace{\frac{1}{X\left[\frac{P_0}{P}-1\right]}}_{y} = \underbrace{\frac{1}{X_m C}}_{\text{intercept}} + \underbrace{\frac{C-1}{X_m C}}_{\text{slope}} \underbrace{\left(\frac{P}{P_0}\right)}_{x} \qquad \textbf{Eq. 21}$$

3.4 Scanning electron microscopy

The morphological characterization of the powder was conducted using Scanning Electron Microscopy (SEM), specifically with the JSM-IT300LV device from JOEL LTD. To obtain intricate details of the powder's surface topography, the Secondary Electron Imaging (SEI) mode was employed, operating at an accelerating voltage of 15kV. This method allowed for a high degree of magnification, up to 10,000x, with a working distance between 8.4-9.4mm, thereby providing a comprehensive and detailed analysis of the powder's microstructure.

3.5 Differential scanning calorimetry

A disk-type heat flux Differential Scanning Calorimeter (DSC) model DSC823e from METTLER TOLEDO was used to characterize the thermal phase transitions of the organic binders and the pastes. A schematic representation of this instrument is presented in Figure 17. This device determines the heat flow rate (by comparing the temperature difference) between two crucibles: one remains empty as a reference, and the other contains the sample under investigation. The DSC monitors the heat absorbed or released by a sample over time or as a function of temperature, producing a curve with peaks corresponding to melting or crystallization events. Conventionally, endothermic events (absorption of heat) are depicted with peaks in the positive y-axis direction, while exothermic events (release of heat) are shown in the negative. Analysis of these curves allows for the determination of several key parameters of thermal transitions: the onset temperature (T_{onset}), indicating the beginning of a transition; the peak temperature (T_{peak}), marking the maximum temperature during melting or crystallization; and the change in enthalpy (ΔH), representing the change of internal energy during the phase transition [75,76].

In this study, the experiments were conducted using sealed aluminium crucibles, loaded with either approximately 10 mg of binder or 20 mg of paste. The calibration of the

instrument was carried out with Indium to establish a baseline, and the zero line was determined by measuring the heat flow from both crucibles when empty, which was then subtracted from the experimental data. Nitrogen gas was utilized to purge oxygen and moisture from the chamber. The flow rate was maintained between 25-30 ml/min.

To ensure consistent thermal history across all samples, a preliminary run involving heating at 10 K/min and cooling at -10 K/min was conducted, with a 3-minute isothermal relaxation period between the heating and cooling phases before the actual measurement. The heating rate was set to 10 K/min, and the temperature range was tailored to the specific measurement needs, typically spanning from -10°C to 90°C.

After data collection, the pre-measured zero line is subtracted from the raw data. This corrected data is then normalized for mass and, if necessary, by the heating rate, yielding the normalized heat flow in Watt per gram (W/g) or Joule per gram kelvin (J/°g K).

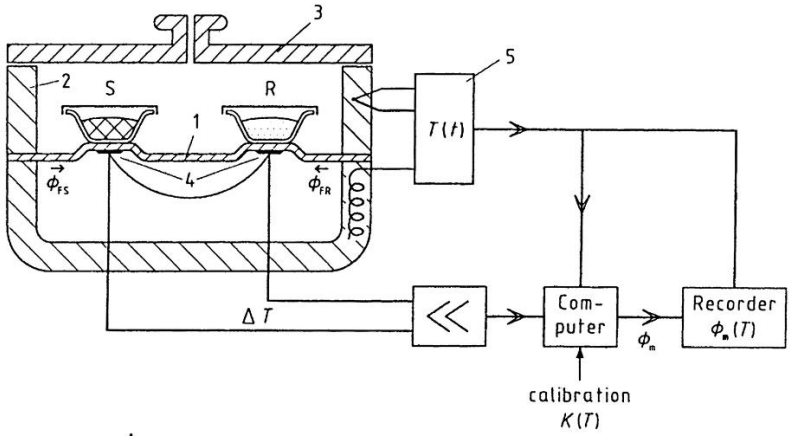

Figure 17: The heat flux DSC with a disk-type measuring system consists of the following components: (1) disk, (2) furnace, (3) lid, (4) differential thermocouple, (5) programmer and controller, (S) crucible with a sample, (R) empty crucible, ($\emptyset_{FS}$) heat flow rate from the furnace to the sample crucible, ($\emptyset_{FR}$) heat flow rate from furnace to the reference crucible, ($\emptyset_m$) measured heat flow rate, and (K) calibration factor [75].

3.6 Capillary rheometer

A PURPOISE P9 capillary rheometer was utilized to establish flow curves of the pastes. The equipment features a barrel with diameters and lengths of 15 mm and 60cm respectively. The pressure transducer is positioned slightly over the die entrance and has a maximum reading capacity of 140MPa. In order to accurately measure the paste with this device, modifications were made to the original brass tip of the piston to prevent upward extrusion, which could result in paste escaping through tolerances between the barrel and piston tip. As a solution, a Teflon-sealed piston was constructed, as recommended by [65]. The redesigned tip replaced the single-piece brass design with three components: a spacer

sleeve, a Teflon sealing ring, and a threaded piston head to secure the assembly together, as illustrated in Figure 18.

The capillary rheometer was employed for generating kneading curves, capillary corrections, and the Reddy model. The capillary was loaded with material and pre-compacted manually, followed by a ram movement at a specified speed until a pressure of 2 MPa was attained. This pre-test procedure facilitated the removal of air and the formation of a continuous mass of material inside the barrel, thereby reducing pressure fluctuations and enhancing reproducibility as all samples underwent a consistent pre-compaction process.

The shear rate sequence consisted of 20 points, ranging from high (50 s^{-1}) to low (2 s^{-1}), spaced logarithmically. This approach ensures that most points were in the low shear rate region, providing a better description of the region with a higher dependency of the viscosity on the shear rate. Moreover, the highest pressures are generated at the highest shear rates, aiding in the pre-compaction of the feedstock and ensuring more stable pressure readings for the subsequent points. The criteria for transitioning to the next shear rate was based on pressure stability; 20 consecutive pressure points had to be within 2% variability to proceed to the next shear rate.

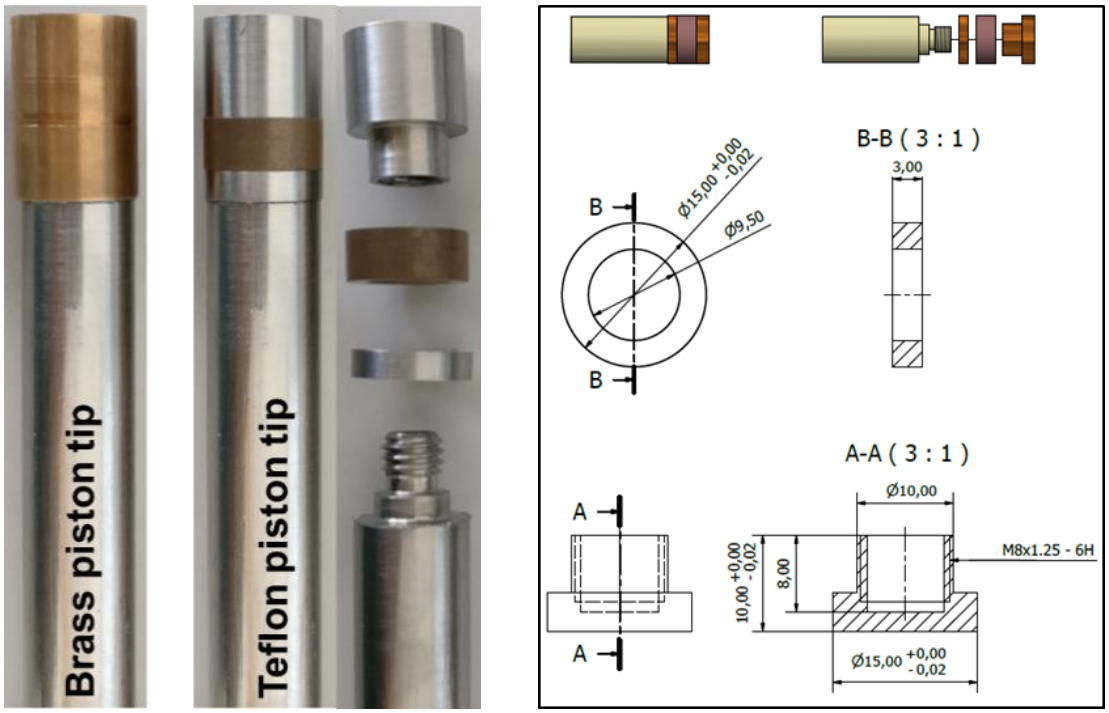

Figure 18: (left) Original brass piston tip and re-designed Teflon piston tip. (right) technical drawing of the Teflon-sealed piston.

For the analysis, several capillaries composed of tungsten carbide were utilized. The standard L/D ratio used in this thesis was 32/2. For capillary corrections, a set with L/D

ratios of 10, 20, 40, and a radius of 2 was employed. The temperature is specific to each feedstock and is accordingly specified in each experiment presented in the results section.

Figure 19 (left) illustrates the impact of the type of piston tip (brass vs Teflon sealed) on the flow curves for a specific paste. The lower viscosity observed for the brass piston is attributed to an upward extrusion of the paste, which impedes the buildup of the correct pressure for a given shear rate, resulting in apparent viscosity values lower than those of the sealed piston. Figure 19 (right) demonstrates the effective sealing effect after a flow curve. When using the brass piston, the paste is extruded upwards about 10 cm, coating the piston and leading to lower pressure readings, and consequently, inaccurate viscosity values.

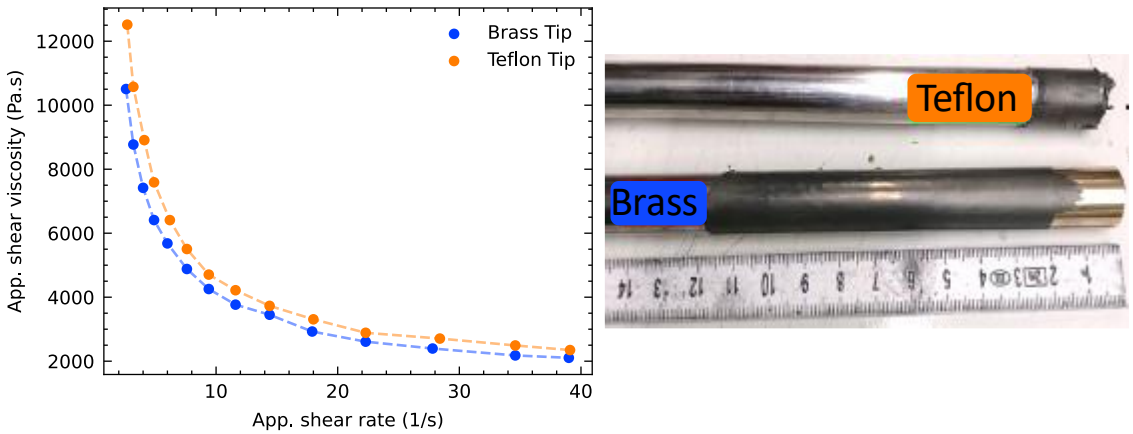

Figure 19: Flow curves of hard metal paste with brass and Teflon tip piston.

3.7 Torque rheometer

A BRABENDER PLASTICORDER kneader equipped with two sigma blades (Figure 20) was utilized for feedstock preparation and titration experiments. The kneader has a volume of approximately 1100 cm^3. Modifications were made to the machine for the purposes of this thesis, including the installation of a cover with an inductive kill switch that activates when the lid is opened. The lid features a visor for inspecting the mixing progress and a dosing chamber that allows the addition of components while the machine is running. Additionally, a thermocouple was placed on the heating chamber, and the rotation speed and torque can be monitored via a PC.

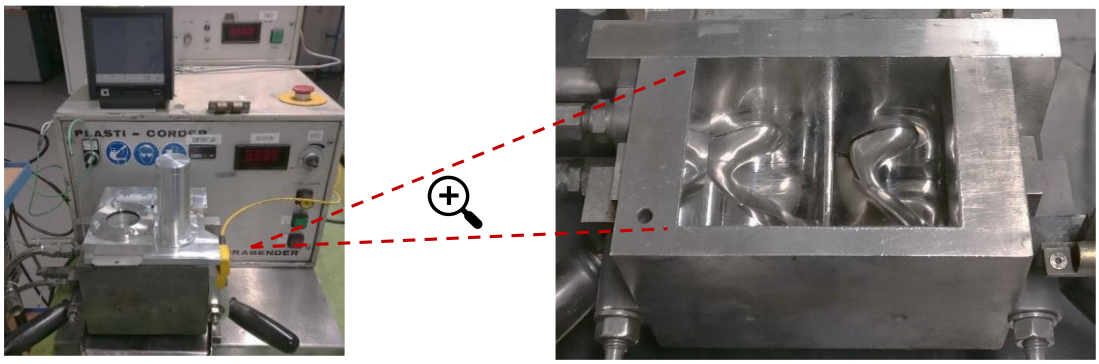

Figure 20: BRABENDER PLASTICORDER kneader equipped with two sigma blades.

Eq. 22 guides the selection of the optimal powder quantity for each mixing batch. This is crucial due to the varying apparent and tap densities of different powders. Using a constant mass of powder for all types could lead to overfilling or underfilling the mixer. The ideal powder quantity is the one that covers both blades, facilitating material exchange across the mixer, while avoiding overfilling that could result in material loss.

In Eq. 22, the optimal powder mass (m_{powder})) is calculated by multiplying the mixer container volume ($V_{bowl\text{-}free}$) by the powder tap density (ρ_{tap}) and a filling factor (K), which was experimentally determined to be 0.6 for this mixer. $V_{bowl\text{-}free}$ is obtained by subtracting the volumes of the blades ($2V_{blades}$) from the full volume of the container (V_{bowl}). For this mixer, V_{bowl} is 1133 cm^3, calculated using the dimensions and volume formula of the cavity geometry, and $2V_{blades}$ is 80 cm^3, measured as the volume displaced when the blades are immersed in water.

$$m_{\text{powder}} = V_{\text{bowl-free}} \cdot \rho_{\text{tap}} \cdot K \qquad \textbf{Eq. 22}$$

3.7.1 Feedstock preparation

The feedstocks for the measurements with the capillary rheometer underwent mixing in the BRABENDER through a three-stage program: melting, kneading, and crushing. Initially, melting occurred at 80 °C and 60 rpm until a paste is formed (approximately 1 hour). Subsequently, kneading at 30 °C and 60 rpm for 5 hours, followed by crushing or grinding the paste at 15 °C and 5 rpm for roughly 1 hour.

Typically, studies on hard metal pastes, as documented in the literature [39,40,43–45], have found that a mixing time under 1 hour is sufficient to distribute the binder across the powder surface uniformly. The parameters used in the laboratory mixer in this thesis result from a series of experiments to optimise mixing speed, time, and temperature. The extended mixing time of 7 hours for the utilized powder is attributed to the nano-sized tungsten carbide particles, which necessitate more time for proper dispersion within the mixture.

3.7.2 Critical binder volume concentration by titration method

The titration method involves systematically adding a controlled quantity of binder in a kneader or internal mixer equipped with rotating blades capable of recording the torque or resistance of the mixing process. The procedure commences by introducing the powder into the mixer, followed by the gradual addition of the organic binder. The average torque for a specific composition is recorded over a set period. As more organic binder is added, the torque increases, indicating the adherence of powder particles to each other. Using this principle, the $CBVC$ is determined at the point of maximum average torque reading.

The $CBVC$ is influenced by various factors, including the powder's surface chemistry, the titration media's viscosity, and its wettability on the powder surface [30], [31]. Hence, in this study, $CBVC$ was determined using linseed oil and a proprietary binder mixture as titration media. Linseed oil, in a liquid state at room temperature, was dosed using a pipette, while the proprietary binder, being a soft solid, was dosed with a spoon, leading to differences in dosing methodology and quantity, as illustrated in Figure 21.

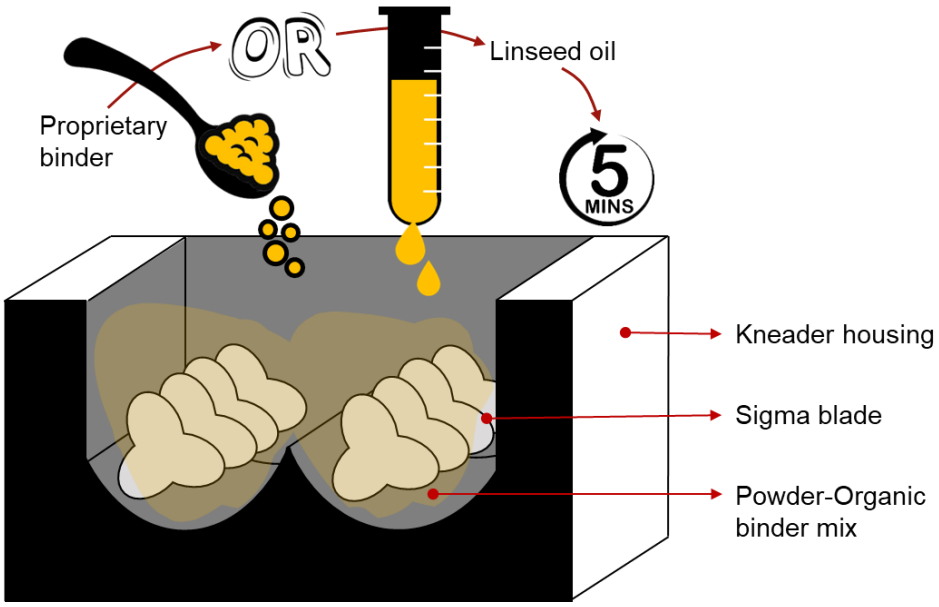

Figure 21: Diagram of the titration methodology used in this research.

In the oil titration process on the nano powder, the de-bindered RTP powder undergoes continuous mixing at 30 rpm and 30 °C in the mixer, while small quantities of oil are systematically added at 5-minute intervals. The duration and precision of the experiment depend on the titration step size. Consequently, the mixing began with 2060 g of powder and 100 ml of oil. Larger initial oil aliquots of 5 ml were introduced into the mix, and when the powder started to exhibit signs of being wet (as depicted in Figure 37, at 51.2 vol.%), the step size was reduced to 2.5 ml to enhance the test resolution.

For the titration involving the proprietary binder and the nano powder, given the multi-component nature of the binder, a mother batch was prepared using a heat plate and a magnetic stirrer. Initially, all the organic components were weighed and combined in a beaker. Subsequently, the components were mixed in a molten state for 5 minutes and cooled until solidification occurred. The mother batch was then utilized as the titration media, incrementally adding it to the bulk (2060 g of powder) in steps of 1.5 g, ranging from 4.00 to 6.10 wt.% (39.1 to 49.9 vol.%). To facilitate this, the mixing temperature was set above the melting points of all organic components (80 °C) at a speed of 30 rpm, with an equilibrium time of approximately 5 minutes between successive aliquots.

For the titration with micro systems, the test conditions were aligned with those for the nano powder. The mixing temperature was set to 30 °C, the speed to 30 rpm, and the titration step size to 0.8 vol% of linseed oil. The powder quantity inside the mixer was calculated to maintain the same initial powder volume as the nano system, ensuring that both blades remain covered with material during titration, thus facilitating efficient mixing. Given the similar tap densities of both systems, using the same mass is appropriate (Eq. 22).

3.7.3 Critical binder volume concentration by the uniaxial die press method

The $CBVC$ assessment procedure for the uniaxial die press method is a systematic process that begins with the addition of an initial concentration (for instance, 10 vol.% organic binder) of WC-Co powder and an organic binder (either linseed oil or a proprietary binder) to a double-arm sigma blade kneader (BRABENDER PLASTICORDER). The total weight of the powder remains constant as the binder is added to achieve the desired concentration. The components are mixed for 30 minutes at a temperature above the organic binder's melting point (30 °C for linseed oil and 80 °C for the proprietary binder).

A 200 g sample is then extracted from the mixer and allowed to cool to room temperature before undergoing pycnometer density measurement and uniaxial die pressing. Each pressing cycle applies a pressure of approximately 7000 kg/cm^2 (686 MPa) to a 15 g portion of the mixture at a steady compression speed of 2 mm/s.

Following testing, the powder samples are returned to the mixer to maintain mass balance. The pressed sample is then ground back into powder using a mortar and pestle before being reintroduced to the mixer. Subsequently, an additional portion of the organic binder is added to the mixer to increase the concentration (e.g., to 20 vol.%), and the process is repeated.

To facilitate the present analysis, it is recommended, based on experience, to include at least four concentrations significantly below the $CBVC$. This ensures a comprehensive and accurate assessment of the $CBVC$.

This study utilized two types of uniaxial die presses, a manual hydraulic press (Figure 22, left) and a DORST TECHNOLOGIES EP16 electric press (Figure 22, right), to develop the methodology for $CBVC$ zero-pressure assessment ($CBVC_{P0}$). Both presses feature rectangular prism cavities with dimensions of 24.40 mm (length), 8.20 mm (width), and 46.00 mm (height), with a precision of ± 0.01mm. A constant sample mass of 15 g was used for compression testing.

The manual press was initially used to validate the concept. However, the lengthy analysis time, the potential for operator-induced variability and the need for higher forces justified the use of the electric press for the final method definition, ensuring efficiency and consistency in the assessment process.

Figure 22: (left) Manual hydraulic and (right) DORST TECHNOLOGIES EP16 used for the development of the methodology to assess the $CBVC_{P0}$ with the uniaxial die method developed in this study.

3.8 Materials

The tungsten carbide-cobalt (WC-Co) and tungsten carbide (WC) powders used in this thesis were provided by CERATIZIT Luxembourg S.à r.l.. Hard metal powder is a composite of WC powder, a metallic binder (cobalt), and various additives such as grain growth inhibitors and carbon or metallic tungsten. These components are combined in an attritor mill with wax and a solvent, then spray-dried to produce Ready-To-Press (RTP) granules. For all experiments excluding the kneading curves, the RTP granules undergo thermal treatment to eliminate the wax, resulting in "de-binded" powders. In contrast, WC powders are monophasic and do not contain any metallic or organic binder. Figure 23 illustrates the differences between WC, RTP, and a single hard metal granule.

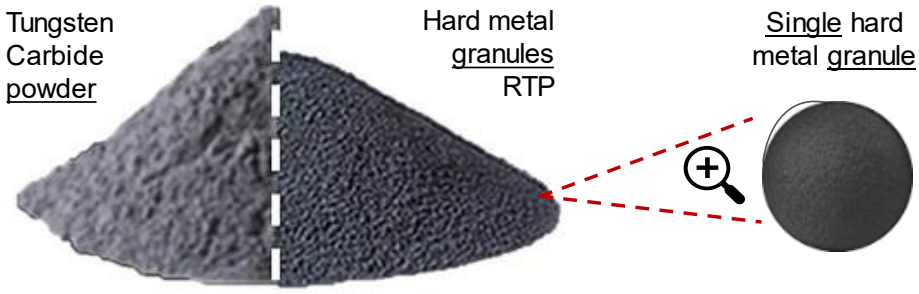

Figure 23: Schematic depicting the physical characteristics of tungsten carbide powder and hard metal granules.

The main system of this thesis is a nano grain size WC-Co powder with low cobalt content (<0.2wt.%). In Figure 24 and Table 1, SEM images and the basic powder properties including grain size, tap and pycnometer density of the de-binded RTP are displayed. The powder called "nano" was used for the kneading curves, capillary corrections, Herschel–Bulkley model, Benbow–Bridgwater model, for the $CBVC$ determination by theoretical calculation, density method, titration method and Reddy's model. Additionally, it was used to develop the uniaxial die press method for $CBVC$ determination.

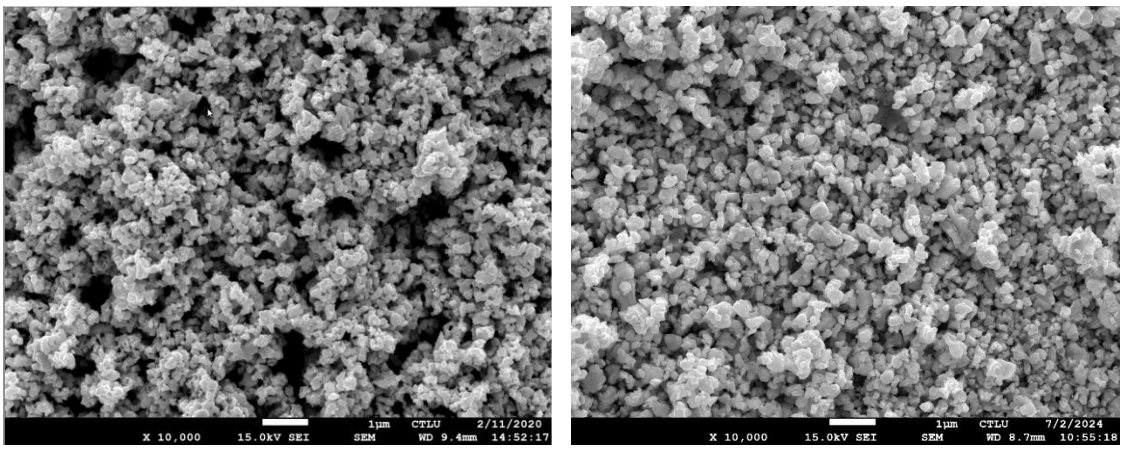

Figure 24: SEM images of the dewaxed WC-Co systems (left) Nano and (right) Micro.

The nano system was mixed with a proprietary binder at a fix binder-powder concentration (52.6 vol.% of binder) for the kneading curves, capillary corrections, Herschel–Bulkley model, and Benbow–Bridgwater model. For the $CBVC$ determination by organic binder titration method and for Reddy's model, the same binder composition was used but at several concentrations. In addition, a WC-Co system labelled as micro was used as a comparison system for the kneading curves (mixed with proprietary binder at 52.6 vol.% of binder) and for $CBVC$ determination by oil titration.

Table 1: Overview of the essential properties of the studied nano and micro grain size hard metal powder systems.

Powder class	WC content (wt.%)	WC size (nm) *	BET (m^2/g)	Pycnometer density (g/cm^3)	Tap density (g/cm^3)
Nano	99.8	200	5.91	14.52 ± 0.04	3.42
Micro	99.6	500	3.82	14.88 ± 0.03	3.41

* Indicate the particle size of the hard phase (WC) prior to attritor milling. This quantity was not measured directly; it was obtained from the material description provided by the producer.

Two types of organic binders were utilized in this study. The first is pure MAKANA Linseed oil. The second is a proprietary multicomponent binder system provided by the industrial partner, which comprises a blend of polymers, surfactants, and various additives. The pycnometer densities are 0.93 g/cm^3 for linseed oil and 0.94 g/cm^3 for the proprietary binder. The use of linseed oil provides a comparative baseline for studying a wide range of powders, each of which may require different organic binder compositions for optimal processing.

To investigate the impact of grain size on the $CBVC$ several WC powders with a range of grain sizes were selected from the catalogue of the industrial partner. A comprehensive summary of the properties of these powders is provided in Table 2. The powder class will be used as labels in the results section to identify each system and it derives from the Sauter mean diameter.

Table 2: Basic properties of tungsten carbide powders with varying grain size.

Powder class	d10 (µm)	d50 (µm)	d90 (µm)	Sauter Mean Diameter, d[3,2] (µm)	BET (g/m^2)	Pycnometer density (g/cm^3)	Tap density (g/cm^3)
056	0.10	0.39	1.49	0.56	3.26	15.25 ± 0.03	2.71
065	0.16	0.56	1.28	0.65	2.26	15.50 ± 0.03	3.15
080	0.27	0.68	1.62	0.80	1.52	15.43 ± 0.06	5.01
205	1.11	2.10	3.57	2.05	0.41	15.67 ± 0.06	5.81
376	2.32	4.19	6.44	3.76	0.28	15.70 ± 0.05	6.74
702	3.79	8.51	16.63	7.02	0.16	15.68 ± 0.04	6.67

4 RESULTS

4.1 Paste flow

4.1.1 Differential scanning calorimetry

In the following section, the DSC curve of the proprietary binder is discussed. Specific details such as the binder composition and temperature axis are omitted due to confidentiality agreements with the industrial partner. Generally, the system comprises a multicomponent binder ensuring superior wettability of sub-micron grain size WC-Co powder. In addition, its properties enable defect-free shaping and feature a multi-stage de-binding process.

Figure 25 illustrates that the endothermic and exothermic reactions are dominated by two phase transitions, attributed to the melting or crystallization of the main constituents. In addition, the system exhibits a broad phase transition due to its multi-component nature.

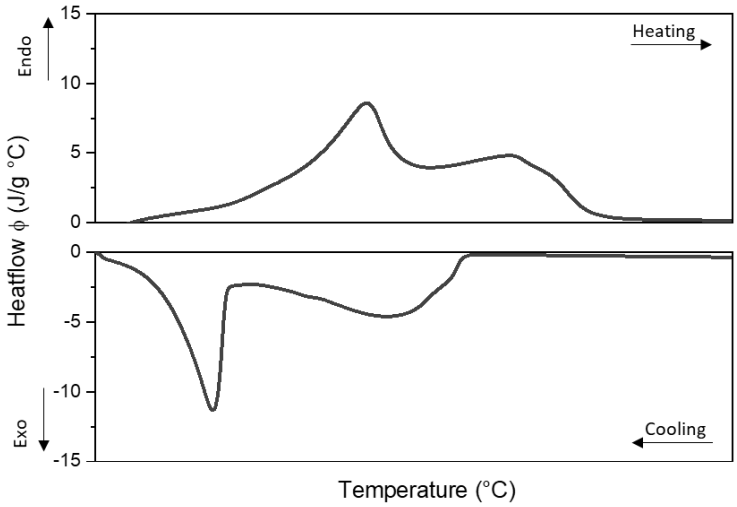

Figure 25: Differential scanning calorimetry of the proprietary binder.

4.1.2 Kneading curves, the effect of grain size on mixing

The kneading process involves mixing the powder (WC-Co or WC) and organic binders to form a paste. As the process progresses, the paste's viscosity decreases due to the binder's dispersion on the powder surface. Frank Händle proposed the "kneading curve" method to assess the effect that kneading time has on the rheological properties of the paste. He used a kneader that had a screw extruder coupled at the bottom, with this, the paste can be sampled in function on time and the pressure is recorded [77].

He applied this method to aluminium oxide (Al2O3), silicon carbide (SiC), and titanium dioxide (TiO2) feedstocks and identified a point at which the extrusion pressure does not change any longer in function of time. The constant pressure signifies that the mixer cannot disperse the organic binder on the powder surface any better under the given mixing conditions. The optimal mixing time for each system was 30, 45, and 80 minutes, respectively [77].

The kneading curve concept aims to investigate how the rheological properties evolve during the mixing process. This evolution is dependent on a multitude of factors, including the characteristics of the powder-organic binder, the type of mixer employed, and various process parameters.

During this PhD project, a modified version of the kneading curve was implemented for two distinct powder systems: nano and micro powders with 52.6 vol% of proprietary binder. Given the extended mixing durations required by these systems, sampling intervals of 45 and 60 minutes were chosen. The mixing process was executed in a LINDEN kneader capable of accommodating approximately 80-litre volume of paste. For each sample, a flow curve was measured in a capillary rheometer, with the testing conducted at 30 °C across a shear rate range spanning from 2 to 30 s^{-1}. The viscosity was determined from pressure and piston speed data using Eq. 6. The capillary geometry had a length of 32 mm and a diameter of 2 mm. Given the similarity in testing conditions, the raw or apparent viscosity can serve as a comparative metric between systems. This allows for an assessment of the ease of mixing and helps in determining the optimal mixing duration for extrusion for each feedstock. The optimal duration is indicated by minimal changes in viscosity between consecutive flow curves.

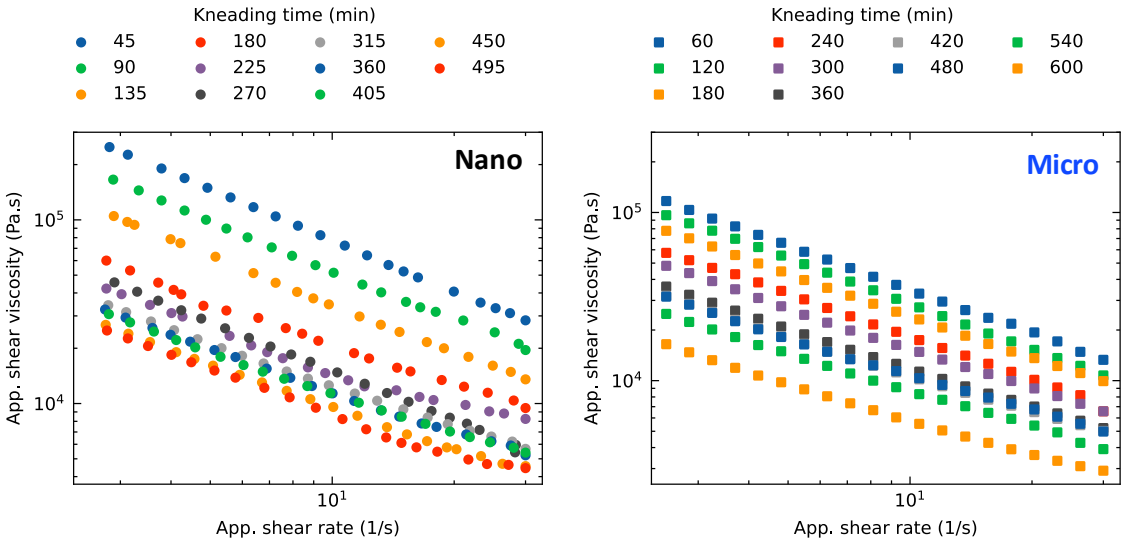

Figure 26: Kneading curve of nano (left) and micro system (right) with 52.6 vol% of the proprietary binder at 30 °C.

An interesting observation emerges when comparing the kneading curves of the nano (Figure 26, left) and micro (Figure 26, right) systems. During the initial two hours of mixing, the viscosity of the nano system exhibits higher values (Figure 27). However, this disparity diminishes after three hours of mixing, and the flow curves manifest similar magnitudes with comparable decreases over time.

This observation elucidates that, owing to the reduced grain size, the initial incorporation of the organic binder within the interparticle spaces proves to be more challenging in the nano system. Nevertheless, with prolonged mixing, both feedstocks can yield comparable flow properties, highlighting the impact of particle size on the dynamics of binder incorporation.

Moreover, the optimum kneading duration for consistent extrusion properties is established by analysing the viscosity at a fixed shear rate of 12 s^{-1} (Figure 27). This shear rate closely approximates the actual shear rates encountered during the industrial extrusion process for these systems. The findings demonstrate that a minimum mixing time of 7 hours is necessary to achieve apparent viscosities bellow 10000 Pa·s which are considered to be in the processing range for industrial extrusion. When comparing these outcomes with those reported for ceramic powder, which reached their optimal state within a maximum of 1 hour [77], the nano and micro system's intricate and multifaceted nature becomes evident.

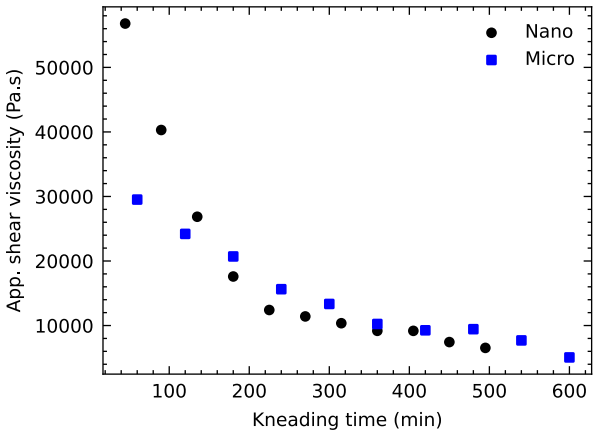

Figure 27: Viscosity change in function of kneading time for nano and micro systems. Tested at 12 s^{-1} and 30 °C.

4.1.3 Capillary corrections

Capillary corrections were applied to obtain the true flow characteristics of a paste formulated with a nano powder system and the proprietary binder at a concentration of 50.8 vol.%. Extrusion was conducted at 30 °C with a shear rate sequence of twenty logarithmically spaced points ranging from 2 to 48 s^{-1}. The correction sequence adhered to GOTTFERT's recommendations for systems with viscosities exceeding 1 Pa·s, namely Bagley, Mooney, followed by Weissenberg-Rabinowitsch corrections [53].

4.1.3.1 Bagley correction

To rectify the influence of the non-homogeneous flow from the barrel to the capillary, flow curves using geometries with a constant diameter of 2 mm and increasing lengths of 10, 20 and 40 mm were used to draw flow curves. In this section, the figures are colour-coded according to die geometry: blue (10mm), orange (20mm), and green (30mm). Triangular markers indicate raw data, circular markers represent Bagley-corrected results, and square markers denote the zero-capillary-length method.

Each point on the pressure versus piston speed curve is derived from four independent flow curves. The error bars in the y-coordinate represent the standard deviation of these four tests at each piston speed. Since the rheometer does not apply exactly the same shear rate for every die geometry, a linear interpolation of pressure values to a fixed shear rate was performed to normalize all die geometries to a set of shear rates.

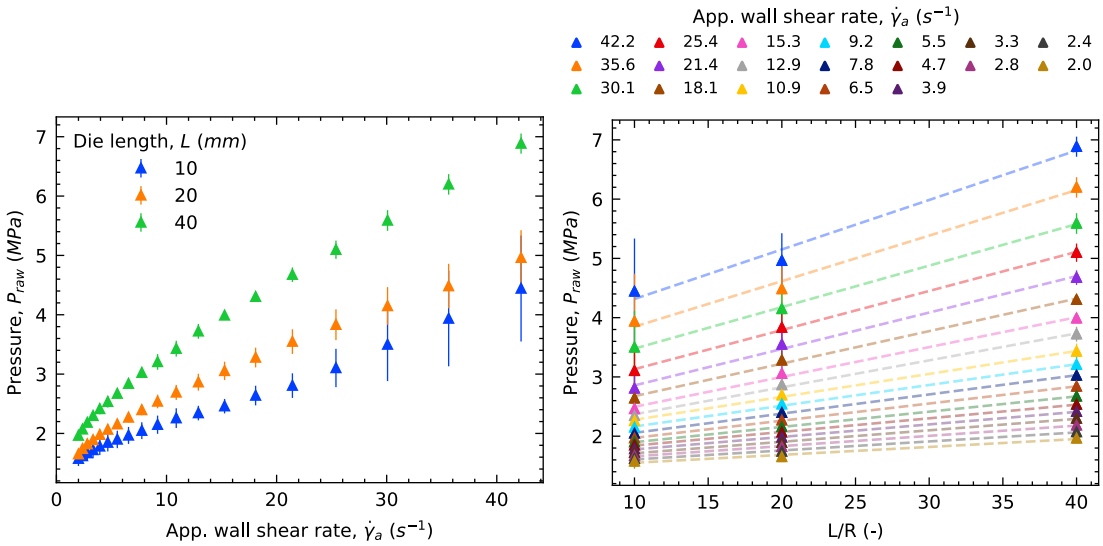

Figure 28: (left) Extrusion pressure curve for several capillaries and (right) Bagley plot.

Figure 28 (left) illustrates the effect of die length on extrusion pressure. Longer lengths correspond to higher recorded pressures and the variability in the data increases for shorter dies at shear rates exceeding 20 s^{-1}. By plotting raw pressure against the L/R ratio (Figure 28, right), a clear linearity emerges, allowing for the determination of the entry pressure effect from the intercept with the y-axis (Eq. 8).

The contribution of the entry effect can now be separated from the overall pressure drop and is depicted as a function of the shear rate in Figure 29 (left). An alternative method commonly employed in industry to assess the entry effect involves recording a flow curve using a "zero-length" capillary. To compare both approaches, four flow curves were generated using such a geometry. Since constructing a truly zero-length capillary is physically unfeasible, we utilized one with a diameter of 2 mm and a length of 0.2 mm.

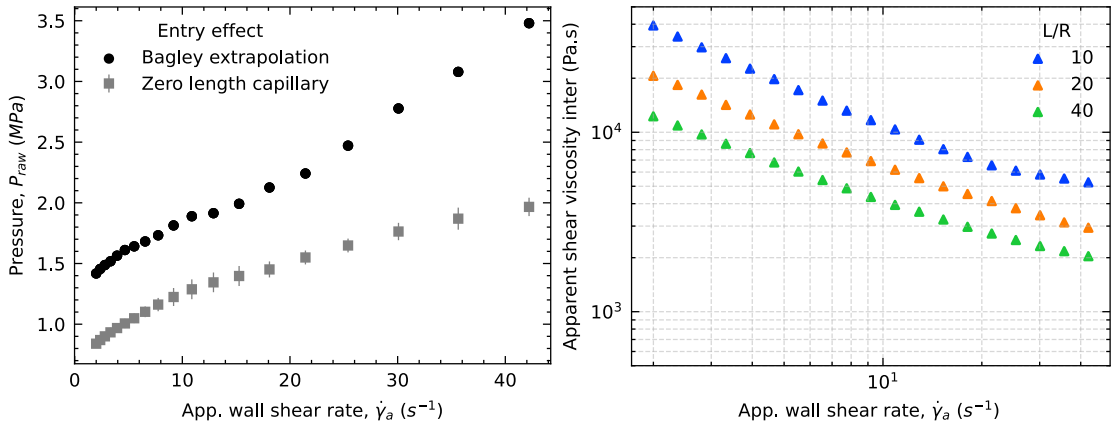

Figure 29: (left) Comparison between entry pressure correction methods and (right) flow curves of the uncorrected extrusion data.

The comparison between the two methods is illustrated in Figure 29 (left), with the Bagley extrapolation method yielding higher pressure values for the entry effect. In Figure 29 (right), the apparent shear viscosities for the three capillaries with varying lengths are presented. We can see that the viscosity depends on the capillary length, which is not true because the viscosity is a material property and should not vary with this parameter. Therefore, it is referred to as apparent shear viscosity, to get the true shear viscosity these values were corrected using both the Bagley extrapolation (Figure 30, left) and the zero-length correction (Figure 30, right).

Figure 30 (left) demonstrates that the Bagley-corrected shear viscosities overlap for most of the tested shear rates. There is minor variability at the first and last data points, at lower shear rates this is attributed to the rheometer's limitation to control slow speeds and at higher shear rates due to the higher variability of the pressure data. Overall, despite the small variability and taking into consideration the complexity of the multi-component system under study, the Bagley correction could be successfully implemented. Conversely, the simpler method of using a zero-length capillary fails to effectively account for the entry effect.

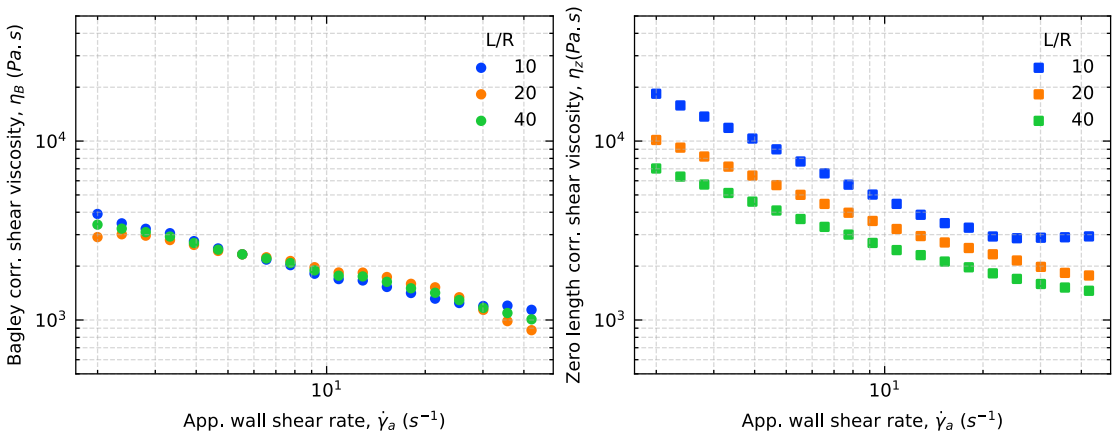

Figure 30: (left) Bagley corrected flow curves and (right) zero-length capillary corrected flow curves.

4.1.3.2 Mooney correction

To measure wall slip velocities using the traditional Mooney approach, flow curves were recorded with capillaries of constant L/D ratios but different diameters. The selected geometries had an L/D of 20 and diameters of 2, 1.5, and 1.75 mm. Similar to the Bagley correction, each point in Figure 31 (left) is derived from four independent flow curves, with error bars representing the standard deviation at each shear rate. Pressure values were interpolated to a fixed shear rate sequence across all capillaries.

Figure 31 (left) illustrates the pressure dependence on capillary diameter. Generally, as the diameter decreases ($1/R$ increases), the recorded pressure increases. This effect is more

pronounced at higher shear rates, whereas at lower shear rates, the geometries with a diameter of 1.5 and 1.75 mm display similar pressure readings.

Using Eq. 11, the shear rate is plotted against $1/R$ for each shear stress (Figure 31, right) to determine the slip velocity from the slopes. The presence of negative slopes indicates that the Mooney analysis fails to describe the wall slip for this paste. Similar issues have been observed by other researchers when applying this method to complex fluids like elastomers [78,79] or pastes [62,80,81].

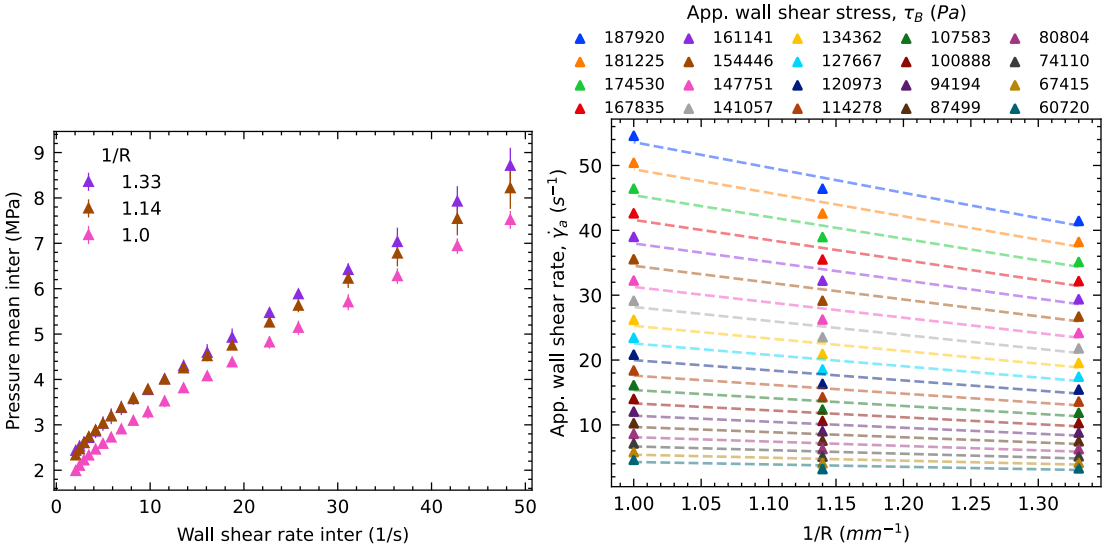

Figure 31: (left) Extrusion pressure curve for several capillaries with constant L/R of 20 with varying diameters of 2, 1.75 and 1.5 mm and (right) Mooney plot.

4.1.3.3 Weissenberg–Rabinowitsch correction

Given that the paste under study is non-Newtonian, the assumption of a parabolic velocity profile in the capillary is invalid. Consequently, the Weissenberg–Rabinowitsch (WR) correction was applied to the average of the three Bagley-corrected flow curves. According to Eq. 13, the true shear rate for a power law fluid is determined from the fit of a plot where the natural logarithm of the apparent shear rate ($ln(\dot{\gamma}_a)$) is plotted against the natural logarithm of the true shear stress at the wall ($ln\,(\tau_{true})$). Due to the inability to perform the Mooney correction to account for wall slip, the apparent shear rate ($\dot{\gamma}_a$) was utilized. A polynomial fit is employed on the average of the Bagley-corrected data (see Figure 32, left) to derive the fitting parameters of Eq. 13: $a = 0.2$ and $b = 0.2$. These parameters facilitate the calculation of dy/dx, which is then used in the WR relationship (Eq. 12) as outlined in section 2.3.1.3 to determine the true wall shear rate ($\dot{\gamma}_{true}$), subsequently enabling the calculation of the true viscosity (η_{true}). Figure 32 (right) put together the outcomes of solely applying the Bagley correction with those of employing both Bagley and WR corrections. Notably, the true shear rates are marginally higher when compared to the raw values, resulting in a slight decrease in the final shear viscosity.

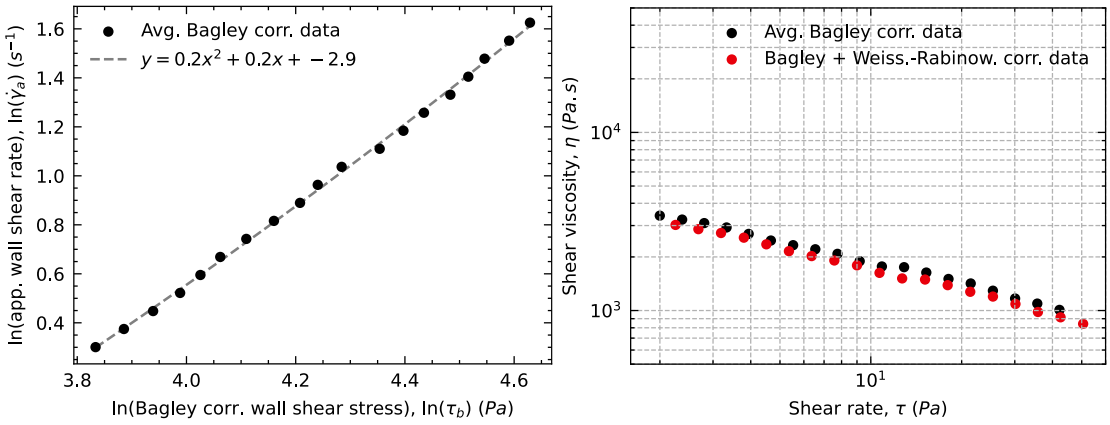

Figure 32: (left) Weissenberg–Rabinowitsch correction and (right) WR correction applied to the average of the Bagley corrected flow curves.

4.1.4 Herschel–Bulkley model

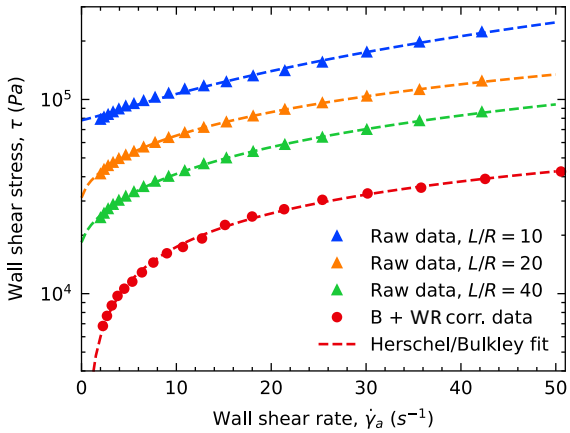

Figure 33: Herschel–Bulkley fit to raw and corrected flow curves. Same colours and symbols as in Figure 28(left), Figure 29 (right) and Figure 32 (right).

The Herschel–Bulkley model effectively describes the flow properties of the pastes within the tested shear rate range. This model was applied to the apparent data from dies with L/R ratios of 10, 20, and 40 (as shown in Figure 29, right), and to the average of the Bagley plus Weissenberg–Rabinowitsch corrected flow curves (indicated by red markers in Figure 32).

The fitting parameters derived for the dashed lines in Figure 33 are summarized in Table 3. The fit was applied to the uncorrected data solely for comparison, emphasizing the significant discrepancies between the uncorrected flow curves and the true material behaviour. The tested nano paste exhibits a yield shear-thinning flow behaviour, with a flow behaviour index (λ) of 0.48 and a consistency index (k) of 6646 Pa·s. The yield stress (τ_0) is extrapolated from the lowest shear rate (2 s^{-1}) within the given range (0-3000 Pa). Testing at lower shear rates would provide a more accurate yield stress value, but the rheometer used was already operating at its minimum speed limit for reliable data acquisition.

Table 3: Parameter from the Herschel–Bulkley model fitted to data in Figure 33. The error stems from the square root of the diagonal of the covariance from the fit and the experimental data.

Sample	Yield stress, τ_0 (Pa)	Consistency coefficient, k (Pa.s)	Flow behaviour index, λ (-)
L/R = 10	78142 ± 1802	2212 ± 407	1.1 ± 0.1
L/R = 20	31195 ± 684	6907 ± 354	0.69 ± 0.02
L/R = 40	18375 ± 531	4152 ± 252	0.74 ± 0.02
Avg. B+WS Corr.	0 ± 2000	6676 ± 800	0.48 ± 0.03

4.1.5 Benbow–Bridgwater model

The same experimental data from section 4.1.3.1 is now analysed following the Benbow-Bridgwater (BB) model. In Figure 34 (left) the extrusion pressure is now plotted as function of the extrudate velocity instead of the shear rate. The extrudate velocity is calculated with the piston speed and geometrical parameters based on the assumption that the volumetric flow rate in the barrel is equal to that in the capillary Figure 34 (right) presents the pseudo-Bagley plot from which the wall shear stress and the yield stress at each speed can be determined from the slope and intercepts respectively.

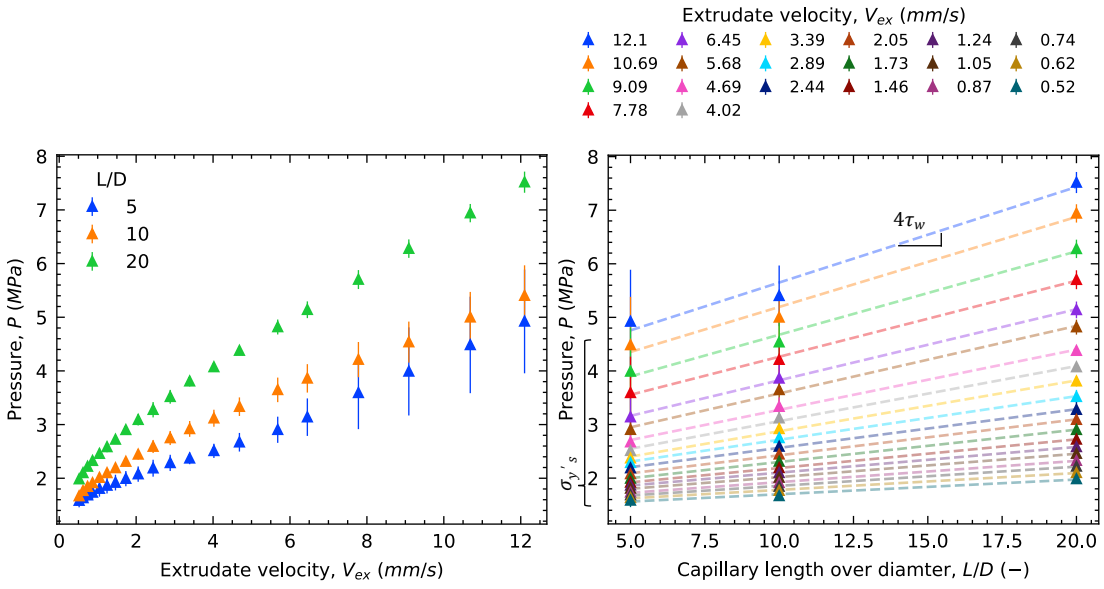

Figure 34: (left) and (right) pseudo-Bagley plots.

In Figure 35 (left) the yield stress (σ_y) and wall shear stress (τ_w) are plotted in function of the extrudate velocity according to the six-parameter model (Eq. 18). The static parameters (σ_0, τ_0) and the velocity-dependent parameters for capillary entry (α, m) and die land (β, n)

are determined using a non-linear least squares optimization implemented with the Python library SciPy.

The fitting parameters together with the experimental conditions are presented in Table 4 where they are compared with results from other researchers who also applied this model to clay and WC-Co paste. Table 4 presents the fitting parameters along with the experimental conditions of the nano system compared with results from other researchers. Figure 35 (right) compares all pastes from Table 4 by fitting the parameters to Eq. 18, a capillary of L/D of 10 is assumed and the data is extended for the shear rate tested by each researcher.

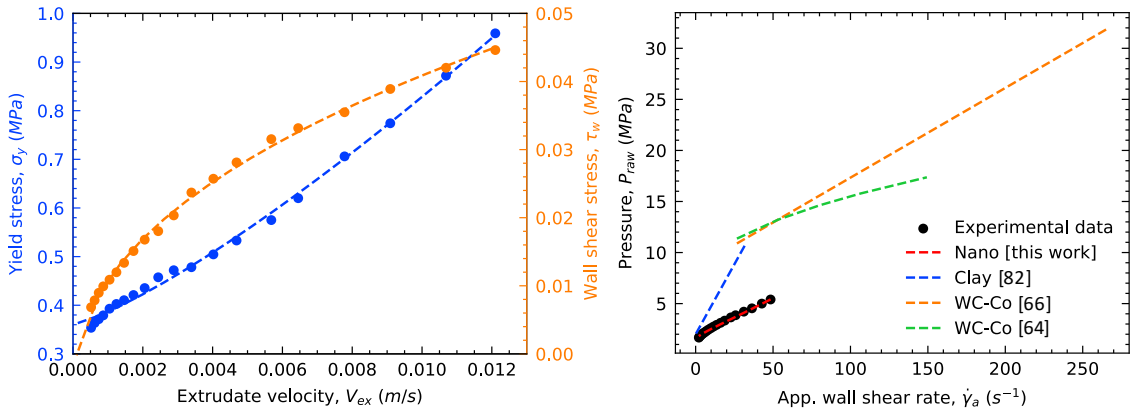

Figure 35: (left) Least-square regression to obtain the six fitting parameters of Eq. 18, and (right) fitted parameters from Table 4 to Eq. 18 for several pastes.

The nano paste exhibits a relatively low initial yield stress (σ_0,), comparable to that of the clay paste. This suggests that extrusion is likely to occur readily when a load is applied from static conditions, in contrast to the other WC-Co pastes present in Table 4. In general, it is advantageous to have some yield stress because it promotes compaction at the onset of extrusion, potentially leading to improved dimensional accuracy of the part. The near-zero wall shear stress (τ_0) indicates excellent lubricating properties of the paste, with minimal friction on the die wall. The high values of α and m imply a strong velocity dependence of pressure in the capillary entry region, while β and n values are low, suggesting a lower velocity dependence within the capillary itself.

The exact reason for the considerably lower extrusion pressure exhibited by the nano paste when compared to the other systems (Figure 35 (right)) cannot be easily discussed, as many factors influence the paste's resistance to flow. However, it is noteworthy that the paste with smaller grain size shows lower viscosity, despite all pastes being used to produce similar products (rods by extrusion) on an industrial scale. This could be due to two factors: either the proprietary binder has lower viscosities and better wetting properties, or the excess of organic binder relative to the $CBVC$ is higher for the nano system.

Table 4: Comparison of fitting parameters and experimental conditions for several pastes

Sample	T	D/D_0	L's	V_{ex}'s	σ_0	α	m	τ_0	β	n
Nano	30	2/14	10-40	0.5-12	0.36	155	1.3	0	0.36	0.44
Clay [82]	30	3/25	4-49	0.1-12	0.32	2.5	1	0.016	18	1
WC-Co [66]	30	3/25	0-40	10-100	1.83	15.2	1	0.02	4.25	1
WC-Co [64]	33	3/25	0-36	10-56	1.3	2.4	0.49	0.025	0.79	0.46

Temperature T (°C), capillary diameter over barrel diameter D/D_0 (mm/mm), capillary length range $L's$ (mm), extrudate velocity range $V_{ex}'s$ (mm/s), initial bulk stress σ_0 (MPa), α (MPa s^m m^{-m}), m (-), initial bulk yield shear stress τ_0 (MPa), β (MPa s^n m^{-n}), n (-).

4.2 Critical binder volume concentration: traditional methods

The material in section 4.2 was orally presented at the Euro PM 2023 Congress and Exhibition in Lisbon. It has been featured in the conference proceedings (peer-reviewed paper) with the title "Comparative Analysis of Methods for Determining the Critical Binder Volume Concentration in Hard Metal Pastes" [5].

The determination of the $CBVC$ is crucial as it is a key component in numerous mathematical models that estimate the viscosity of highly concentrated suspensions [14,83]. It also marks a significant milestone in optimizing the ratio of powder to binder for paste preparation. Importantly, a general agreement among specialists suggests that the best processing conditions for injection moulding are typically attained with a binder excess of 2 to 5 vol.% above the $CBVC$ [10,23,33,84]

Particle arrangements vary between powders and pastes. In a powder, the packing density is affected by interparticle forces such as friction and particle bridging, preventing optimal particle packing [83]. On the other hand, in a paste, the mixing process results in the reorganization of both binder and particles. The binder enters the interparticle spaces, functioning as a lubricant and facilitating closer particle proximity than in a binder-less powder, forming in this way a continuous material.

The $CBVC$ delineates the maximum particle packing that can be achieved while preserving material continuity [14]. It signifies the point at which the binder can sustain particle cohesion, creating a continuous mass. However, at the $CBVC$, the binder quantity is insufficient to lubricate the particles during movement against each other. Consequently, the maximum packing fraction is attained when the viscosity of a concentrated suspension approaches its maximun [83].

The packing density (ϕ) of a particle system is pressure-dependent. As pressure increases, the system gradually compacts until it reaches a maximum packing density (ϕ_m). This maximum value is unique to each granular system. The ϕ_m for a particular system indicates the stage at which particles can come closer without experiencing deformation or breakage.

For spherical and uniformly distributed particles, such as glass beads with a diameter of 10 mm, the maximum packing density (ϕ_m) can be attained solely through a tapping mechanism, as gravitational forces surpass the friction between particles. However, as the particle size diminishes, higher forces are required to achieve (ϕ_m). A threshold is reached where the tapping force alone is insufficient to attain (ϕ_m), particularly for smaller and irregularly shaped particles. In these cases, the application of a compressive force becomes the exclusive method to approach ϕ_m in powders.

The connection between the maximum packing fraction and the $CBVC$ is as follows: ϕ_m denotes the highest possible particle packing for a given system. The empty space within

this configuration corresponds to the $CBVC$, symbolizing the minimum quantity of binder needed to occupy the voids at the granular medium's maximum packing density.

Several methods are available for evaluating the $CBVC$ of powder systems. These include monitoring torque readings [20,24,85], calculating activation energy [33], and measuring density [10] and viscosity [21,86]. This section outlines the results derived from various traditional methods used for determining the $CBVC$. These methods include theoretical calculations, the density method, the titration method, and Reddy's model, all applied to the nano WC-Co system.

4.2.1 Theoretical calculation

In Eq. 23, the critical particle volume concentration ($CPVC$) is defined as the ratio of the tap density (ρ_{tap}) to the pycnometer density (ρ_{pycno}) of the binder-free powder. This ratio serves as an indication of the void space between particles. The determination of the critical binder volume concentration ($CPVC$) is accomplished using Eq. 24 [10,33]. In the context of this work, when the critical value is determined by the theoretical calculation (Eq. 24), the $CBVC$ will be accompanied by the subscript "theo" as $CBVC_{theo}$.

$$CPVC = \frac{\rho_{\text{tap}}}{\rho_{pycno}} \qquad \textbf{Eq. 23}$$

$$CBVC_{theo} = 1 - CPVC \qquad \textbf{Eq. 24}$$

The present investigation utilizes carbide powder in the form of RTP granules, wherein the tap density measurement characterizes the interstitial space between granules rather than individual nano-sized carbide particles. The determined $CBVC_{theo}$ value is 76.4 vol.%, obtained by measuring the tap and pycnometer density of the de-bindered RTP following Eq. 1 and Eq. 2.

The RTP granules are spherical agglomerates of WC, Co and paraffin. After the thermal removal of the paraffin, only WC and Co powder, with no organic binder remains. Post de-binding, the powder retains its spherical shape, influencing its packing ability during tapping. To enhance precision, the tap density was re-evaluated using crushed de-bindered RTP (via mortar and pestle), resulting in a slightly reduced $CBVC_{theo}$ value of 73.3 vol.%.

Regardless of whether the powder was agglomerated into spheres or not, it displayed high $CBVC_{theo}$ values. This is likely because the tapping forces alone are insufficient to rearrange the particles close to the optimal particle packing arrangement.

In the other method that will be presented, we observed that when the powder is mixed with an organic binder, it alters the powder's packing. In the early stages of mixing, the

binder transmits shear forces, breaking up powder agglomerates and reducing voids. This decreases particle-particle distances, resulting in denser packing arrangements, which helps in getting more accurate $CBVC's$. Consequently, the theoretical method is unsuitable for determining $CBVC$ of nanoscale systems.

4.2.2 Density method

The density methodology is based on the assumption that an increase in solid loading (powder) may result in the binder inadequately encapsulating solid particles, leading to voids within the bulk material. Consequently, the feedstock's measured density would be lower than the theoretical density [31,85].

German et al. [10] delineate different regions of a loading curve. In Figure 36 (left), density measurements are illustrated as organic volume content increases. The dashed line represents the calculated theoretical line following the mixing rule, derived from the pycnometer-measured densities of pure components at 0 vol.% organic binder (pure powder) and 100 vol.% organic binder mixture (pure binder). The circular markers represent actual density measurements of the binder-powder mixture. The $CBVC$ is anticipated when the measured density diverges from the mixing rule. A column with diagonal lines denotes the hypothetical optimal solid loading above the critical point, where binder excess promotes particle lubrication and enhanced flow properties.

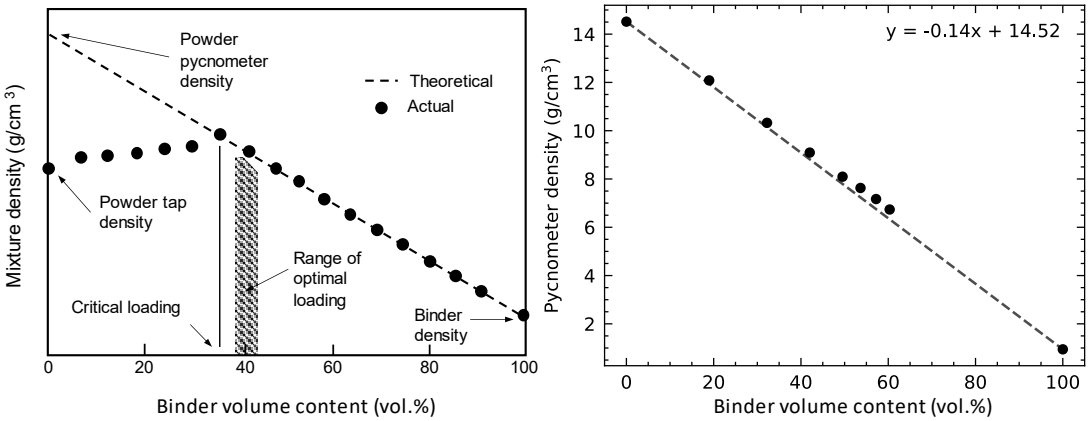

Figure 36: (left) The loading curve. The experimental departure from the theoretical density corresponds to the critical loading. Adapted and redrawn from [10], and (right) density of the feedstock as a function of organic binder content. The dashed line represents the theoretical densities based on a simple mixing rule.

To apply this method to the nano system, several mixtures with varying amounts of proprietary binder were prepared and the pycnometer density was measured for each concentration. In the presented results in Figure 36 (right), no noticeable distinctions were evident between the theoretical and experimental density values. Therefore, the density

method proved ineffective for the examined system in this research. This can be solely attributed to the capability of the employed measurement method (pycnometric measurement with helium as the working gas) to account for any voids in the system.

These findings align with those presented by Abajo et al. [23], who linked the imprecision of this method to the markedly irregular morphology (angular shape) of the powder particles and the existence of fine particles (1.94-5.49 µm) in a low viscosity binder system. In contrast, Hidalgo et al. [31] explored critical loading using torque and density measurements on Invar 36 feedstock. They noted an approximately 5 vol.% difference in the $CBVC$ value depending on the technique employed, with values of 32.5 and 37.5 vol.% derived from torque and density measurements, respectively.

4.2.3 Titration method

As the organic binder content increases, the powder bulk transitions from a free-flowing powder to a paste-like flow. To document this physical transition during the paste formation process, a camera was positioned on the visor of the kneader, and the mixing process was recorded as a video. From this video, characteristic images at different organic volume percentages were extracted to construct Figure 37, providing visual insights into the influence of varying linseed oil content on the behaviour of the bulk material.

Figure 37 shows that at 46.8 vol.% of linseed oil, the bulk material predominantly maintains a cohesive "dry" powder state with discernible lumps. However, with an increase in the ratio of organic binder (from 51.2 vol.% to 52.4 vol.%), the binder effectively binds more metal particles together in the form of agglomerates, resulting in a visually wetter appearance of the bulk material and an increase in torque reading towards a maximum value (Figure 38, left). The maximum torque reading (at 53.5 vol.%) corresponds to the formation of a coherent or continuous mass in the mixer, commonly referred to as a paste, where the binder content is sufficient to hold most powder particles together. However, the lack of binder results in increased particle-particle friction and, consequently, the highest torque readings because of inefficient lubrication.

Incremental incorporation of additional binder leads to a reduction in torque owing to an increase in the particle-particle distance (Figure 2) and enhanced lubrication, providing advantages for the processing stage. Various studies have indicated that an optimal binder loading for the injection process lies within a binder excess of 2 to 5 vol% above the critical value [10,23,33,84]. Beyond this optimal range, the properties of the paste tend towards those of pure organic binder, transforming into a low-viscosity slurry-like material.

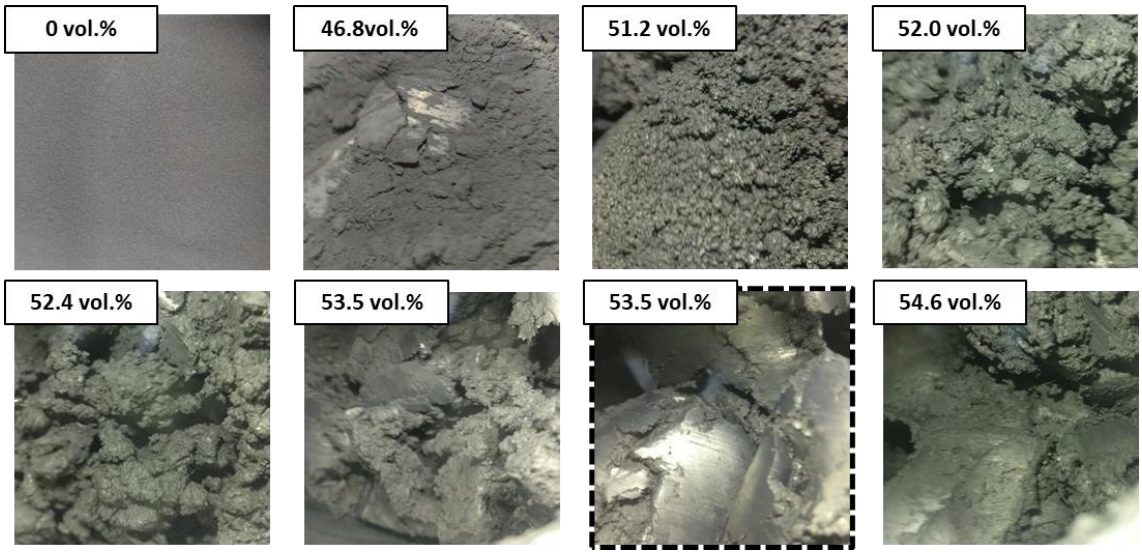

Figure 37: Titration with linseed oil at 30 °C on dewaxed hard metal powder with a nano grain size. Visuals depict a progression of images showcasing increasing linseed oil content, ranging from 0 to 54.6 vol.%. The image enclosed by a black dashed frame is the $CBVC$, corresponding to 53.47 ± 0.4 vol.%.

Figure 38 presents the outcomes of the titration experiments with linseed oil at 30 and 80 °C. In the plots, the y-data represents the average torque readings during a 5-minute kneading period, and the error bars depict the fluctuation, indicating the minimum and maximum torque recorded for each concentration within the time window. The $CBVC_{titra}$ correspond to the concentration that records the maximum average torque reading.

The titration curves reveal three distinct regions, each region will be described for the case of linseed oil at 30 °C (Figure 38, left): (1) a stable region with minimal torque fluctuation up to 51.2 vol.% oil content, indicating the predominance of a powder-like form, (2) an intermediate region from 51.2 vol.% to 53.47 vol.% marked by a significant torque increase and higher variability, attributed to the binder's impact on powder particle agglomeration and paste formation, and (3) a region beyond the critical point where torque and variability decrease, signalling reduced frictional forces due to excess binder. Ultimately, the maximum average torque reading and, therefore, the $CBVC_{titra}$ is estimated to lie within the 53.47 ± 0.4 vol.% range. The standard error reported for the $CBVC_{titra}$ arises solely from the titration step size of the previous and subsequent points around the maximum and not from repetitions of the experiment.

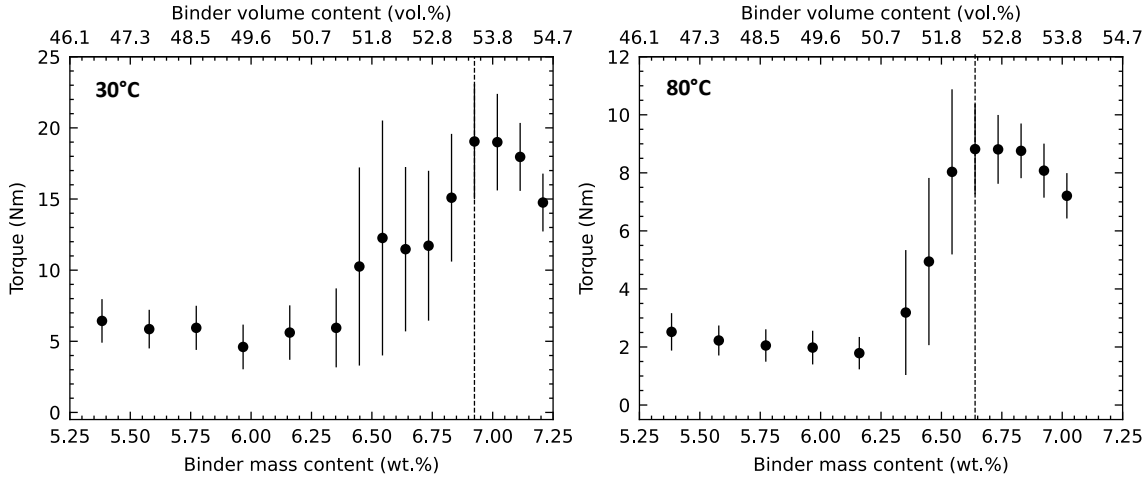

Figure 38: Titration with linseed oil performed on dewaxed hard metal powder with a nano grain size. Average torque readings over a 5-minute duration are plotted against the organic content. The dashed vertical lines denote the $CBVC_{titra}$. (left) at 30 °C resulting in 53.5 ± 0.4 vol.% and (right) at 80 °C equals 52.3± 0.4 vol.%.

Analogous to the titration with oil, the $CBVC_{titra}$ was now determined using the proprietary binder mixture as a titration media at 80 °C for the same hard metal system (Figure 39). The highest torque reading corresponds to 49.3 ± 0.3 vol.% (5.95 ± 0.05 wt.%) of organic binder. The error is indicative of the binder addition step size. Additionally, the transition from powder to paste was observed to align with the highest torque reading, offering visual confirmation that the $CBVC_{titra}$ falls within the proposed range.

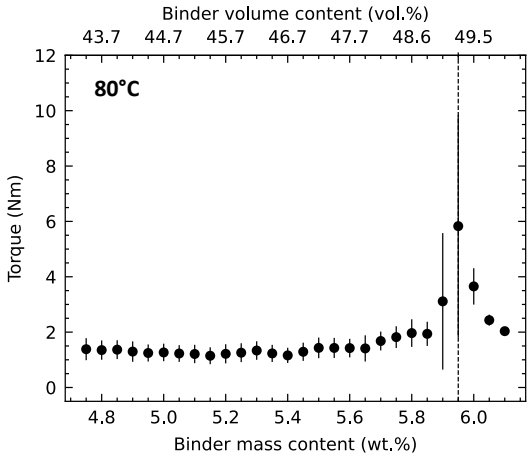

Figure 39: Titration with proprietary binder performed on dewaxed hard metal powder with a nano grain size at 80 °C. Average torque readings over a 5-minute duration are plotted against the organic content. The $CBVC_{titra}$ (49.3 ± 0.3 vol.%) is denoted by a dashed vertical line.

A notable difference of 3.0 vol.% in the organic content at the $CBVC_{titra}$ was observed when comparing the oil titration results with those obtained using the proprietary binder at 80 °C. In addition, the temperature increase of 50 °C in the oil titration experiments caused a decrease in the $CBVC_{titra}$ of 1.2 vol.%. The variations in the results are attributed to the difference in viscosity and wettability of the titration media for each experiment. These results underscore the substantial influence of binder properties on $CBVC_{titra}$ determination.

For the sake of comparison, the oil titration experiment was performed on the micro system. The test was performed at 30 °C with a greater titration step size of 0.8 vol.%. The average torque is presented in Figure 40 in the same way as for the nano system.

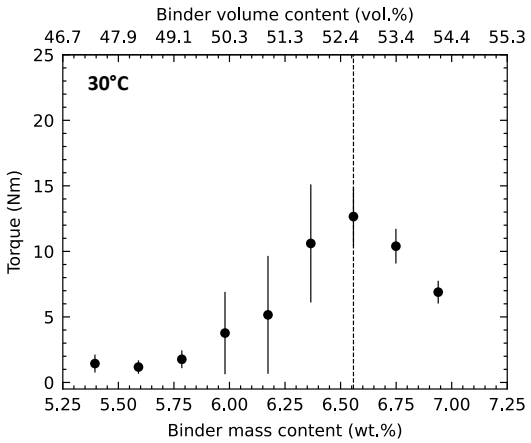

Figure 40: Titration with proprietary binder performed on dewaxed hard metal powder with a micro-grain size at 30 °C. Average torque readings over a 5-minute duration are plotted against the organic content. The $CBVC_{titra}$ (52.6 ± 0.8 vol.%) is denoted by a dashed vertical line.

The micro system exhibits a $CBVC_{titra}$ of 52.6 ± 0.8 vol.%, which is slightly lower than that of the nano system under identical experimental conditions. Additionally, the torque value at $CBVC$ is also lower for the micro system. Given the similar chemical nature of both systems, we can infer that a paste made with the micro system would require less organic binder to achieve similar rheological properties as one made with the nano system.

Furthermore, the torque readings indirectly measure viscosity by recording resistance to flow and mixing. The higher torque values of the nano system suggest that a paste with this powder would probably have higher viscosities compared to the micro system (assuming the same organic binder and quantity). This disparity is attributed to the difference in grain size.

4.2.4 Reddy's model

Reddy et al. [86] propose a method to determine the critical binder volume content by measuring the viscosity (η) at a fixed shear rate and temperature for several binder volume contents (BVC). The $CBVC_{Reddy}$ can be determined from the slope following Eq. 25. Assuming optimal mixing is achieved (as indicated by the asymptotic behaviour of viscosity in the kneading curve), Reddy's model offers a distinct advantage over the titration method by providing a $CBVC$ value independent of mixing parameters.

In addition, this method enables the estimation of the viscosity of the pure binder or binder without powder (η_b). Following Eq. 25, the critical powder volume content ($CPVC$) is equal to $1 - CBVC$, meaning that η_b can be derived from the y-intercept.

$$\eta \cdot BVC = \eta \cdot CBVC + \eta_b \cdot CPVC \qquad \textbf{Eq. 25}$$

This methodology requires the preparation of a minimum of three paste batches with varying binder content, all ensuring a binder excess above the $CBVC$ so that the feedstock

has good flow properties to enable the measurement of its viscosity. In this investigation, five batches of 2000 g were prepared and analysed using the proprietary binder composition. The binder content across these batches spanned from 48.6 to 52.1 vol.%, with increments of 0.9 vol.%. The viscosity measurements were conducted using a capillary rheometer (PURPOISE P9) equipped with a hard metal die featuring an orifice diameter of 1.5 mm and a length of 30 mm at 32 °C.

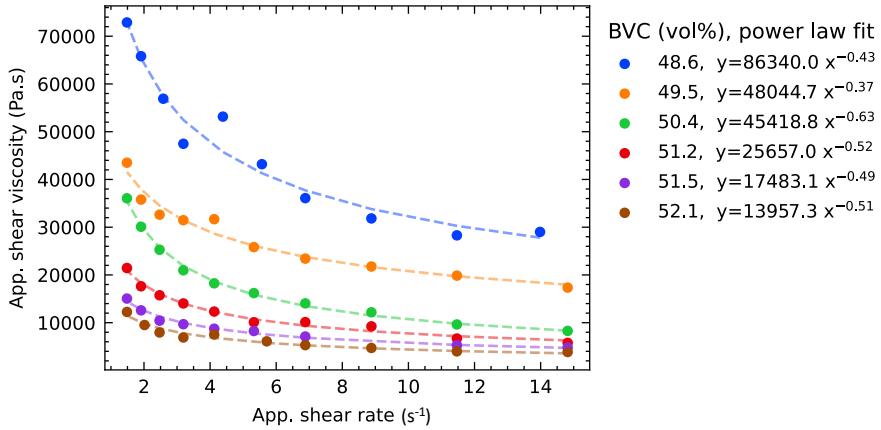

Figure 41: Flow curves obtained from a capillary rheometer at 32 °C with a die length of 30 mm and a diameter of 1.5 mm. The test involved a sequence from high to low shear rates, including an initial pre-compaction step.

For this method, determining viscosity at a single shear rate is sufficient. However, flow curves were generated for each of the five concentrations to explore the impact of shear rate on the critical value, spanning shear rates from 1 to 15 s^{-1}. The outcomes are presented in Figure 41, where shear thinning dominates the flow properties across the studied concentration range. The data aligns well with a power law, as evidenced by the fitting parameters in the legend.

For the same system, Figure 39 demonstrated a decrease in the average torque reading after 49.3 vol.% of organics, where torque served as an indirect viscosity indicator. In contrast, Figure 41 precisely illustrates lubrication's impact on the feedstock's viscosity as the organic content exceeds the critical value.

Figure 42 (left) presents the Reddy plot derived from viscosity measurements at a single shear rate (11.5 s^{-1}) for all concentrations. The $CBVC_{Reddy}$ is determined from the slope of the linear fit employing Eq. 25. Similarly, in Figure 42 (right), the analysis is reiterated for each shear rate shown in Figure 42 (left). Comparing the fluctuations in $CBVC$ values in Figure 42 (right) with results from other methods indicates that $CBVC$ determined via Reddy's model is largely independent of shear rate within the tested range. The difference from the lowest to the highest shear rate tested is less than 0.3 vol.%. Consequently, the

average $CBVC_{Reddy}$ is established at 47.97 ± 0.08 vol.% were the error stems solely from the standard deviation of the $CBVC$ determined at various shear rates and not from repeating the complete experience several times.

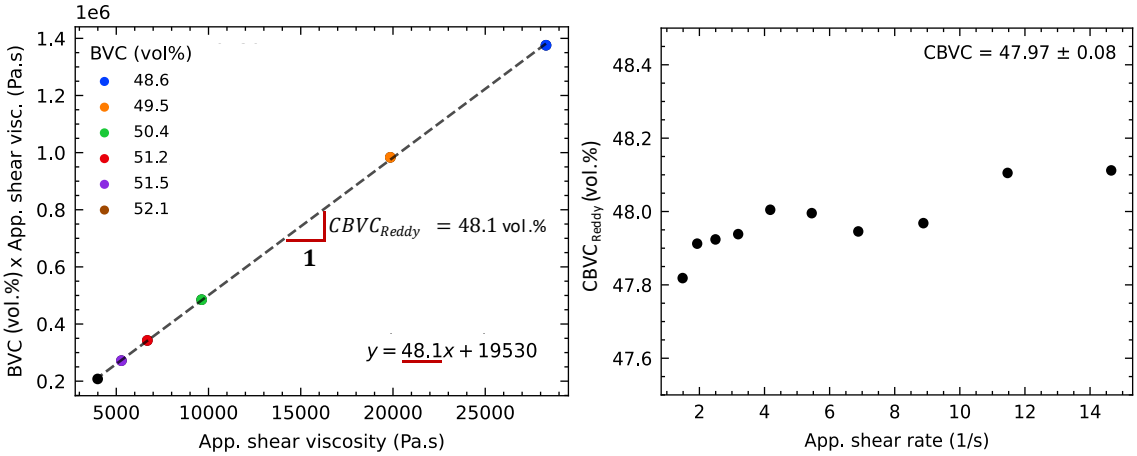

Figure 42: (left) Reddy analysis conducted at a shear rate of 11.5 s^{-1}, using the same colour legend as depicted in Figure 41, and (right) $CBVC_{Reddy}$ calculated for every shear rate evaluated.

Furthermore, Figure 43 (left) illustrates an exponential decrease in viscosity correlating with an increase in binder volume content. This trend suggests that the viscosity should eventually approach that of the pure organic binder (η_b = 376 Pa·s). Additionally, Figure 43 (right) demonstrates that the density of the powder-binder system adheres to a simple mixing rule, exhibiting a linear decrease in density as the Binder Volume Content (BVC) increases.

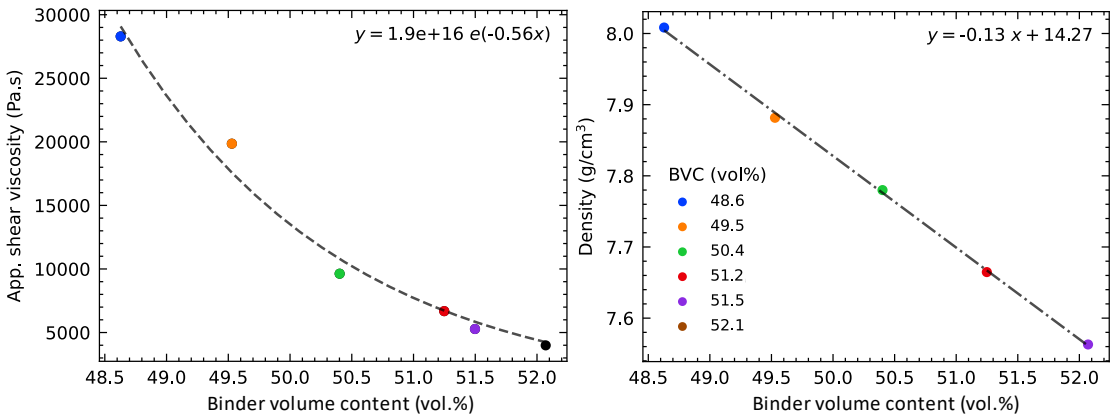

Figure 43: (left) Influence of the increase of binder content on the viscosity at a shear rate of 11.5 s^{-1}. Shared marker colour legend with Figure 41, and (right) Pycnometer density in function of the binder content. Shared marker colour legend with Figure 41.

Table 5: Overview of the critical binder volume concentration determined through different methodologies for the nano-sized hard metal powder system.

Method	Theoretical calculation	Oil titration (30 °C)	Oil titration (80 °C)	Binder titration (80 °C)	Reddy's model (32 °C)
CBVC (vol.%)	76	53.5 ± 0.4	52.3 ± 0.4	49.3 ± 0.3	47.97 ± 0.08

4.3 Uniaxial die pressing for determining the critical binder volume concentration

The material encompassing sections 4.3 to 4.3.4 was featured in a paper published in the Powder Technology Journal. The paper is titled "Assessing Critical Binder Volume Concentration Using Uniaxial Die Pressing: An Alternative Approach" [87].

This section introduces a novel approach for calculating the Critical Binder Volume Concentration ($CBVC$) of powder systems. This method employs both press and pycnometer density measurements to determine the $CBVC$ by examining the pressure-related behaviour of powder compaction within a confined cavity, highlighting the balance between the powder internal friction and packing capacity. We corroborate the technique by comparing it with the previously presented methods and applying it to the nano powder system combined with two different organic binders, linseed oil and a proprietary binder. The present approach determines the optimal packing fraction more efficiently and requires less material than traditional $CBVC$ methods. Additionally, we introduce a zero-pressure density (ρ_{P0}) concept and foresee its potential use with other types of powders, including ceramics and metals.

As previously discussed, the maximum packing density (ϕ_m) is a characteristic of the granular system and has a direct correlation with the $CBVC$. In the previous section, the $CBVC$ values using the theoretical calculation, oil titration, binder titration, and the implementation of Reddy's model (Table 5) lead to different results for the same hard metal system. Interestingly, each method produces a different $CBVC$ value, highlighting the necessity for a careful strategy in interpreting, comparing, and applying this crucial parameter across various research.

In its loose state, each powder has an initial particle arrangement with voids between the particles. This state is characterized by the apparent density, which is the density of the bulk powder when gently poured without the application of external forces. To transition into a paste, the volume content of the organic binder (BVC) must exceed the $CBVC$ ($BVC > CBVC$). The application of pressure can reduce the volume of these voids as it overcomes the frictional forces that hinder the transition to a denser state. Consequently, density increase can be achieved via two main strategies: increasing the pressure for a mixture with a fixed powder and binder volume content, or augmenting the binder quantity while keeping the pressure and volume constant (only the volume of voids decreases). The interaction between these two options offers insights into the minimum binder quantity required to fill the interparticle space when most particles are in contact. However, both strategies are complex due to factors such as the powder's internal friction and the specific properties of

the organic binder. This interaction can be examined using a press to compact a powder binder mixture at several concentrations.

As outlined by Boursier et al. [88], the compaction process of solid particles and organic binder is primarily governed by two factors: the deformation of binder bridges between particles and the friction among solid particles. As illustrated in Figure 44 (left), the binder, due to prior mixing, is dispersed among the particles, forming bridges. However, during compaction, as the solid particles draw nearer to each other, the binder is relocated towards the interstitial spaces until direct contact between particles is established, leading to friction between solid particles (Figure 44, right). In this study, we leverage this mechanism to ascertain the $CBVC$ by examining the densification process occurring during compression (the collapse of binder bridges and friction between solid particles).

Yarton et al. [89] conducted a study on the influence of lubrication on densification and ejection during the pressing of metal compacts. Their research centred on the impact of stearic acid on copper powder, studying pressures ranging from 0-746 MPa and lubricant concentrations between 0-33 vol.%. Their results demonstrated a consistent reduction in voids with an increase in lubricant content, thereby establishing a direct relationship between lubrication and compact density. The ideal lubricant content for compressing their system was found to be 1-2 vol.%.

Zheng et al. [90] investigated the impact of adding polyethylene glycol binder to alumina powder on compaction efficiency. Their study revealed that the binder serves as a lubricant, enhancing particle rearrangement and achieving higher packing densities at lower pressures.

Traditionally, Reddy's model evaluates materials resembling paste with high binder content and approaches the $CBVC$ from above ($BVC > CBVC$) by recording flow curves of pastes with decreasing binder content [86]. The $CBVC$ values derived from Reddy's model are valuable for practical applications because they are directly based on the flow properties of pastes. However, a significant disadvantage is the high cost associated with measuring multiple flow curves using extruders or capillary rheometers.

In summary, a method is needed to determine the CBVC that addresses the limitations and inaccuracies of theoretical approaches, is straightforward to perform, and yields $CBVC$ values independent of the binder type. The method proposed in this study concentrates on powders with binder contents below the $CBVC$, akin to granular or powder-like materials. This method is based on pressure curves recorded during powder compression. The $CBVC$ is derived by extrapolating to zero pressure conditions following the rearrangement and compaction of particles. This results in a $CBVC$ value that represents the lowest achievable

limit for all practical applications (termed as $CBVC_{P0}$, this quantity is introduced in the following section).

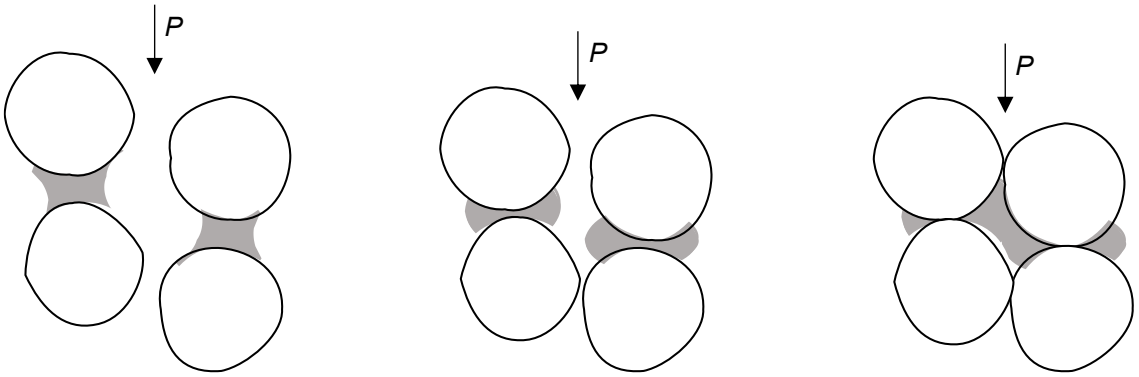

Figure 44: Influence of pressure on the displacement of particles (white) and organic binder (grey) in a confined cavity.

4.3.1 The mechanism involved during compression

Figure 45 illustrates the reconfiguration of particles (depicted in white) and binder (shown in grey) during the compression cycle within a confined cavity. Initially, the mixture consists of loosely packed powder particles wetted by the organic binder as shown in Figure 45 (a). The mixture of powder and organic binder, which is below the $CBVC$, displays a distribution of organic binder along with voids both within and between particles (represented in blue),

When placed into the cavity, the mixture initially has a height of h_0 that gradually reduces to h_t over time due to the pressure applied by the upper punch. At lower pressures, the compaction process causes the rearrangement of particles and the expulsion of air, leading to a decrease in volume within the cavity and an increase in compressed density.

With the increase of pressure, the creation and breakup of binder bridges, along with air expulsion, become the primary mechanisms driving compaction. During the compression phase, the particles in the mixture are rearranged, leading to the systematic elimination of voids and the achievement of a particular compressed density (refer to Figure 45 (d)). However, when an excess of the organic binder is present and the pressure continues to rise, a tertiary mechanism takes place. The binder within the compressed segment starts to be pushed out towards the surface of the pressing tool, a process referred to as squeeze-out.

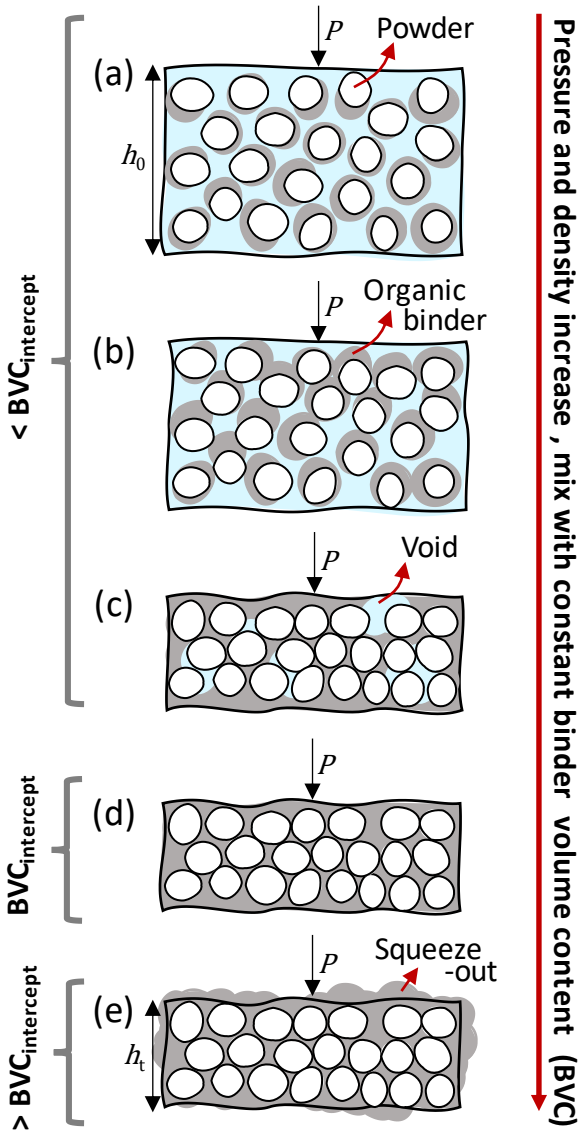

Figure 45: Possible configurations of particles during the compression phase in a uniaxial die press. The rectangular boundary represents the die structure; the WC-Co powder is symbolized by white circles, the organic binder is represented by the grey segment, and the blue region signifies the space filled with air. As the downward pressure increases, the height decreases, promoting the creation of binder bridges between particles and friction among solid particles.

This happens when the majority of voids are already occupied by the binder, but the pressure keeps increasing, leaving no alternative for the binder to move except towards the compact surface and within the tolerances between the cavity and the upper/lower punch, similar to water being squeezed out from a sponge under pressure (see Figure 45 (e)).

It is suggested that increasing the organic binder's concentration (BVC) within a mixture improves the compound's compressibility by diminishing the internal friction among particles. This implies that as BVC increases, the necessary pressure reduces due to lubrication, eventually reaching the $CBVC$ at zero pressure (P=0, i.e., $CBVC_{P0}$). At this point, it is assumed that the organic binder occupies all the voids between particles, resulting in maximum densification.

4.3.2 Experimental model – Introduction

The approach outlined here is designed to determine the minimum amount of organic binder necessary to attain the highest packing fraction (ϕ_m). This approach is established on a number of fundamental assumptions, such as the incompressibility of the oil, the homogeneousness of the mixture, and the absence of deformation or fracturing of tungsten

carbide grains during the mixing or compression process. The diagrams in Figure 46 provide a schematic depiction of the collected data, which will serve to illustrate the experimental model.

In order to determine the $CBVC$ using this method, we utilize density data obtained from two separate techniques: uniaxial die pressing, which offers a view into the density under load or compressed density curves, and pycnometer measurements, which set the theoretical density curve. Figure 46 (a) graphically illustrates the compressed density (ρ_c) as a function of the applied pressure (P), calculated from data collected through upper punch position and force sensor measurements during the compression process. These density values are computed by dividing the mass of the powder-binder within the cavity m by the die top view area A and die height h, as per Eq. 26.

$$\rho_c = \frac{m}{h \cdot A} \qquad \textbf{Eq. 26}$$

In order to determine the compaction pressure (P_c), the first step involves transforming the compression force (F_c) data into pressure by using the ratio of the force to the die top view area (A), as illustrated in Eq. 27.

$$P_c = \frac{F_c}{A} \qquad \textbf{Eq. 27}$$

The procedure continues with the measurement of pycnometer density for both the pure powder (0 vol.% organics) and the organic binder (100 vol.% organics) system, black circles in Figure 46 (b). If the system adheres to a basic mixing rule (where the density is linearly dependent on the ratio of each component), a linear regression between these two data points represents the theoretical density. The black markers and the dashed trendline in Figure 46 (b) depict the graph of binder volume content versus pycnometer density (y_1). This linear fit sets the maximum achievable density at each concentration and outlines the mixing rule as per Eq. 28.

$$y_1 = m_1 \cdot BVC + b_1 \qquad \textbf{Eq. 28}$$

The graphical analysis in Figure 46 (c) is derived from the combination of data from Figure 46 (a) and (b), putting together both the compression and theoretical density curves. This visual interpretation reveals the correlation between the compression curve data and the organic volume content and density.

To elucidate the correlation between binder content and pressure, a linear regression model is employed on constant pressure values across diverse binder concentrations, as denoted

by the grey dashed lines in Figure 46 (c), in accordance with Eq. 29. These grey dashed lines in the graph symbolize isobars, suggesting that at constant pressure, an increase in the amount of organic binder will eventually lead to a point where the compressed density aligns with the pycnometer density ($y_1 = y_2$). Furthermore, as the pressure exerted by the upper punch increases, particles tend to move closer, reducing the volume of binder required for the compressed and pycnometer densities to coincide, as higher pressures result in less interstitial space between particles.

$$y_2 = m_2 \cdot BVC + b_2 \qquad \textbf{Eq. 29}$$

The intercepts obtained from the extrapolations along the isobars, which are subject to variation based on organic content, are referred to as binder volume content intercepts ($BVC_{intercepts}$). These $BVC_{intercepts}$ fundamentally signify the pressure (P) boundary at which the compressed density matches the pycnometer density ($y_1 = y_2$). Following this, we determine the $BVC_{intercepts}$ with Eq. 30. Linear extrapolations are used, but they may not accurately represent the material's behaviour, particularly at higher binder concentrations. This is evident in the following step:

$$BVC_{intercept} = \frac{b_2 - b_1}{m_1 - m_2} \qquad \textbf{Eq. 30}$$

The intercepts ($BVC_{intercepts}$) from Figure 46 (c) are now plotted as a function of pressure, as shown in Figure 46 (d). This graph contains two distinct regions: a non-linear section at lower pressures, which illustrates the initial phase of particle reorganization and air expulsion from the compact, and a linear section at higher pressures, which depicts the elastic deformation of the compact (including the elastic deformation of the grains) in a specific arrangement. As outlined in Eq. 31, a linear fit is applied to the latter section.

As previously mentioned, the deviation of the $BVC_{intercepts}$ from the dashed line illustrates the material's non-linear behaviour under compression. The extrapolation of this linear section to the y-axis (marked by a red cross in Figure 46 (d) at $P = 0$) can be interpreted as the minimum amount of organic binder required to achieve the theoretical $CBVC_{theo}$ (pycnometer/tap density) at zero pressure following particle rearrangement. Therefore, in Eq. 31, as P approaches 0, the $BVC_{\text{intercept}}$ is equal to $CBVC_{P0}$.

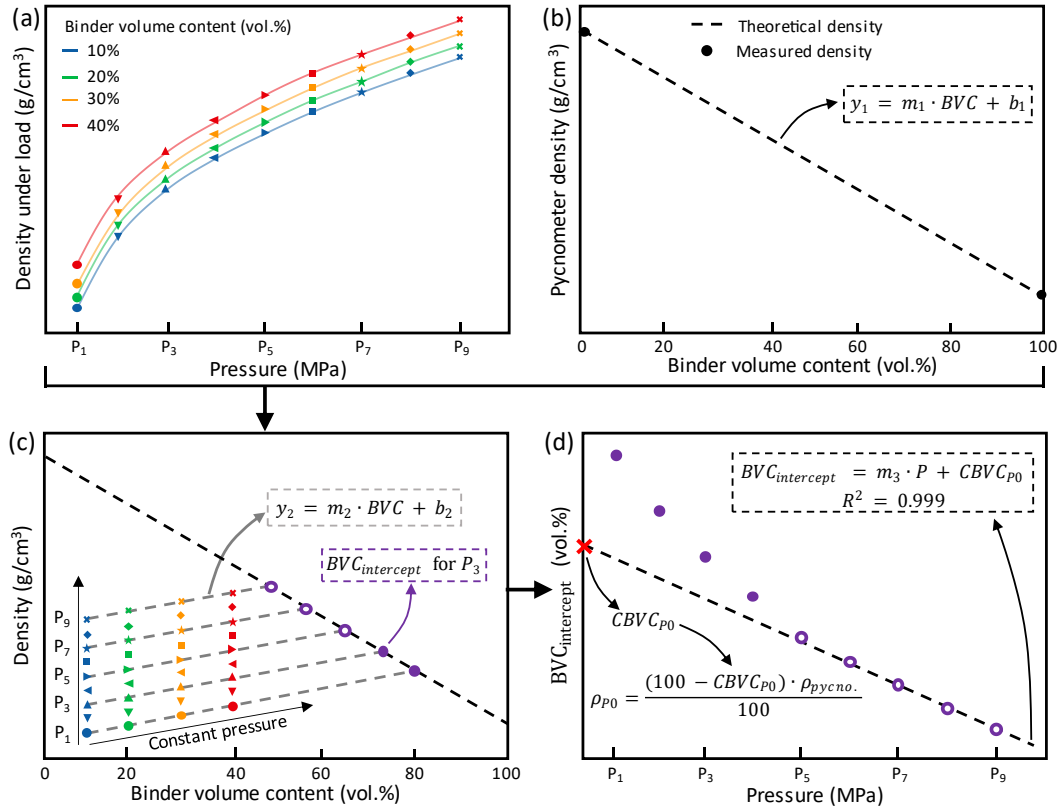

Figure 46: Conceptual representation of the suggested method. (a) compression curves at varying organic content, (b) pycnometer density and the linearity of the mixing rule, (c) pressure data restructured, and a linear regression is applied to constant pressure values to ascertain the $BVC_{intercepts}$, and (d) extrapolations are made from the isobars for each pressure to determine the $CBVC$. For more details, see text.

$$BVC_{intercept} = m_3 \cdot P + CBVC \qquad \textbf{Eq. 31}$$

It is crucial to understand that for a given concentration, the density under load (excluding elastic deformation) cannot exceed the calculated density line of the material (Figure 46 (b)) during the densification process, as outlined in the experimental section ($y_2 \leq y_1$). Therefore, the evaluation occurs at the intercept in Figure 46 (c).

The decrease of the slope in Figure 46 (d) implies that this section would become horizontal if the compact were non-compressible. However, the presence of a slope (m_3) signifies the ongoing compressibility of the compact (elastic effects) and probably the existence of residual voids.

Furthermore, these intercepts in Figure 46 (c) are determined based on the assumption of a void-free particle arrangement, as illustrated in Figure 45 (d). While some areas may contain voids, as depicted in Figure 45 (c), it is assumed that such void spaces are insignificant at the $BVC_{\text{intercepts}}$. This scenario more accurately mirrors the structure of the

compact, akin to the previous example of perfectly packed 10 mm spheres, demonstrating an ideal distribution of binder and particles with no voids.

In Figure 46 (d), the method used to differentiate between linear and non-linear regions significantly influences the derived $CBVC_{P0}$, which is inferred from the y-intercept of the linear regression. It is essential to establish strict criteria to identify this transition across various datasets. The criterion adopted is detailed below.

The data was examined from higher to lower pressures (P_{max} to P_0), starting with a set of data points for linear regression (e.g., from point P_{max} to $P_{max-100}$). The coefficient of determination (R^2) is computed for this fit. This process repeats incrementally through successive data points ($P_{max-101}$, $P_{max-102}$, ... to P_0), recalculating R^2 for each new linear regression. The transition point is determined where R^2 falls below 0.999, ensuring accuracy and consistency in identifying the linear region, which is essential for determining $CBVC_{p0}$.

4.3.3 Zero-pressure density

For any specific type of particle, one can compute a theoretical maximum packing fraction. However, in experimental settings, this maximum packing fraction is rarely achieved when the volume is diminished, for instance, through compaction in a press. In the context of pastes, i.e., when a liquid phase (binder) is introduced to the particles, the packing fraction of the solid phase initially decreases due to the space taken up by the liquid phase. When the volume is reduced, such as in a press, the lubrication effect of the binder allows particles to move closer together than they could without it. This implies that under high pressures, a packing fraction close to the maximum packing fraction could be attained. Upon releasing the pressure, the so-called zero-pressure density is achieved, which is greater than the density that can be reached in the absence of a liquid phase during the compaction process (Figure 46 (d)).

The zero-pressure density is of paramount importance for applications as it is independent of the type of the liquid binder phase. In the context of the hard metal powder system discussed in this study, this means that the binder's sole purpose is to enable the achievement of that final packing fraction and, consequently, the zero-pressure density.

The zero-pressure density value is considered to be more universal and applicable to systems beyond hard metal powders. When the uniaxial pressure method presented is employed, the zero-pressure density, denoted as ρ_{P0}, can be straightforwardly calculated using the $CBVC_{P0}$ as follows:

$$\rho_{P0} = \frac{(100 - CBVC_{P0})}{100} \cdot \rho_{pycno} \qquad \textbf{Eq. 32}$$

4.3.4 Experimental model – Validation

The experimental model was implemented on the nano WC-Co powder system using two distinct organic binders: linseed oil and a proprietary binder. The sequence of mixing and pressing was done in duplicate for each binder type to evaluate the reproducibility of the method. The results of the first and second mixing are illustrated in Figure 48 and Figure 49 for linseed oil, providing an assessment of the impact of mixing, weighting, and dosing on the determined $CBVC_{P0}$. Additionally, within each iteration of mixing (e.g., the first mixing), pressing was performed twice at each concentration using new material, thereby isolating the variability solely attributable to the pressing process (e.g., top and bottom of Figure 48).

The same procedure was employed for the proprietary binder, which involved two separate mixing iterations and the pressing of two compacts in each (Figure 50 and Figure 51). For each binder, the final $CBVC_{P0}$ values reported represent the average and standard deviation of the four compressions.

In Figure 48 (left), compression curves are displayed for five concentrations of linseed oil, ranging from 10 to 30 vol.% in increments of 5 vol.%. A clear and significant correlation is evident from the data: an increase in the concentration of the organic binder leads to a noticeable increase in densification at the same applied pressure. This phenomenon is mainly due to the lubricating properties of the binder. Acting as a lubricant, the organic binder reduces friction between WC and Co powder particles during compression. This reduction in friction facilitates particle movement, enabling them to form a denser structure at lower applied pressures as the organic content increases.

At low pressures, the primary mechanism driving the compression curve is the rearrangement of particles. This leads to a decrease in void volume as particles move closer together, and a corresponding increase in density, particularly noticeable at lower pressures [91]. As particles approach each other, frictional forces become more prominent, hindering further densification of the powder for each unit of pressure applied. This is evident as a linear segment with a positive slope at higher pressures (refer to Figure 48 and Figure 49, left) [91].

It is important to note that the material being studied is expected to exhibit minimal elastic deformation. Additionally, the chances of particle fragmentation, plastic deformation, or cold welding are low. These assumptions are supported by the high hardness of the powder, which makes the mentioned scenarios unlikely under the current experimental conditions.

In Figure 48 (middle), the data has been reorganized according to the experimental model. The chosen concentration and pressure range approach the squeeze-out region without crossing it. It is critical not to exceed this limit because exceeding it would force the binder out of the compact (see Figure 47). This would decrease the concentration of the organic binder in the compact, causing noticeable slope changes in the compression curves at higher pressures. Squeeze-out is also visible when the compact is removed from the die, as the upper punch will be coated with the expelled organic binder. Any data affected by this event has been excluded to keep the integrity of the analysis.

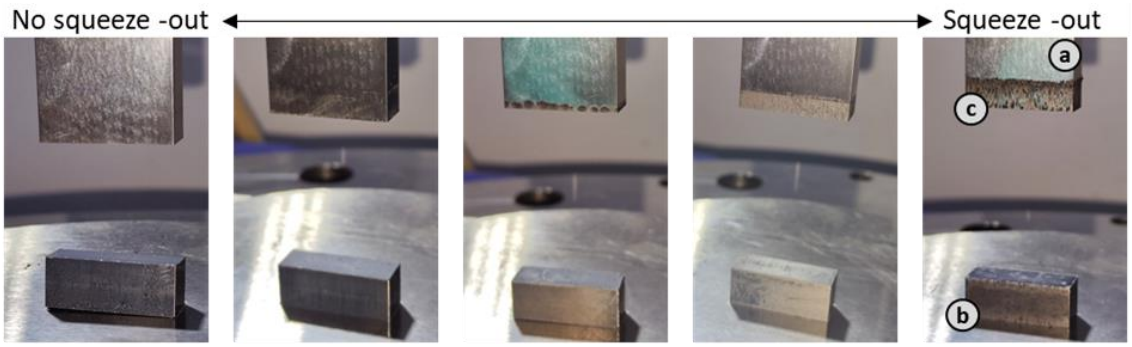

Figure 47: The diagram provides a detailed view of the binder extrusion levels seen during the compression process. It specifically shows (a) the top punch, (b) the compressed compact, and (c) traces of expelled binder. The series starts with the image on the far left, where the top punch is shown to be clean after compression, indicating no squeeze-out. Progressing towards the right, there is a subtle increase in the evidence of binder loss or squeeze-out, underscoring the variations in compaction and binder retention.

The theoretical density curve in Figure 48 (middle) is based on pycnometer density measurements at 0 and 100 vol.% of organic binder. Only two points are enough to draw the theoretical line because, in the previous chapter, it was proven the linearity of the intermediate concentrations for this system [5].

The uniaxial press produces over 2000 pressure-displacement data pairs in a single compression cycle. For clarity, only nine such pairs are shown in Figure 48 (middle). The analysis uses 730 data pairs, ranging from 10 to 740 MPa, starting at 10 MPa, to ensure that a linearity is present at lower pressures across organic binder content. These 730 binder volume concentration intercepts contribute to the construction of Figure 48 (right). From the y-intercept of the linear portion of this graph (purple markers), the $CBVC_{P0}$ was found to be 46.7 ± 0.1 vol.% using linseed oil. The process was repeated with a proprietary binder as the organic medium (Figure 50 and Figure 51), resulting in a slightly lower value of 45.8 ± 0.1 vol.%.

The reported result is an average value, accompanied by the standard deviation. The spread which stems from repeating the complete experiment twice for each organic binder is low. However, a significant difference is observed at lower pressures in Figure 48 and Figure

50 (middle); the proprietary binder displays steeper slopes in the isobar profiles ($m_{2's}$) which is attributed to its slightly better lubrication on the WC-Co powder compared to linseed oil. As the pressure escalates, this effect gradually diminishes. This change leads to lower intercepts of binder volume content, resulting in a marginally decreased $CBVC_{P0}$ for the proprietary binder.

In section 4.2.3 [5], we investigated the $CBVC$ for the same system using different techniques and under various conditions (Table 5). A consistent finding was the substantial overestimation of $CBVC$ when using the titration method compared to the proposed method. This overestimation mainly stems from the inherent delays present in the titration technique. It is important to note that the determination of $CBVC$ via titration is prone to fluctuations based on the binder system's wetting ability for the specific powder, the mixing temperature, the mixing speed, the titration step size and the time between each titration step [85].

When we compare the outcomes for the proprietary binder using Reddy's model from section 4.2.4 [5] with the results from the current experimental approach, we notice a deviation of about 2 vol.%. Reddy's model is centred on paste, while our technique starts with powder that has a low organic content below the $CBVC$. On the other hand, Reddy's model is employed at higher binder concentrations above $CBVC$ to ensure the material is adequately extrudable for analysis. This fundamental disparity in starting points explains the anticipated variation between the two methods, as validated by our experimental findings which yield lower values with the suggested method.

It is worth mentioning that while Reddy's model is also precise, it is labour-intensive as it requires the formulation and blending of several batches with different concentrations and optimal extrusion properties. In contrast, our method provides a faster and simpler alternative, demanding less material and time due to its continuous nature.

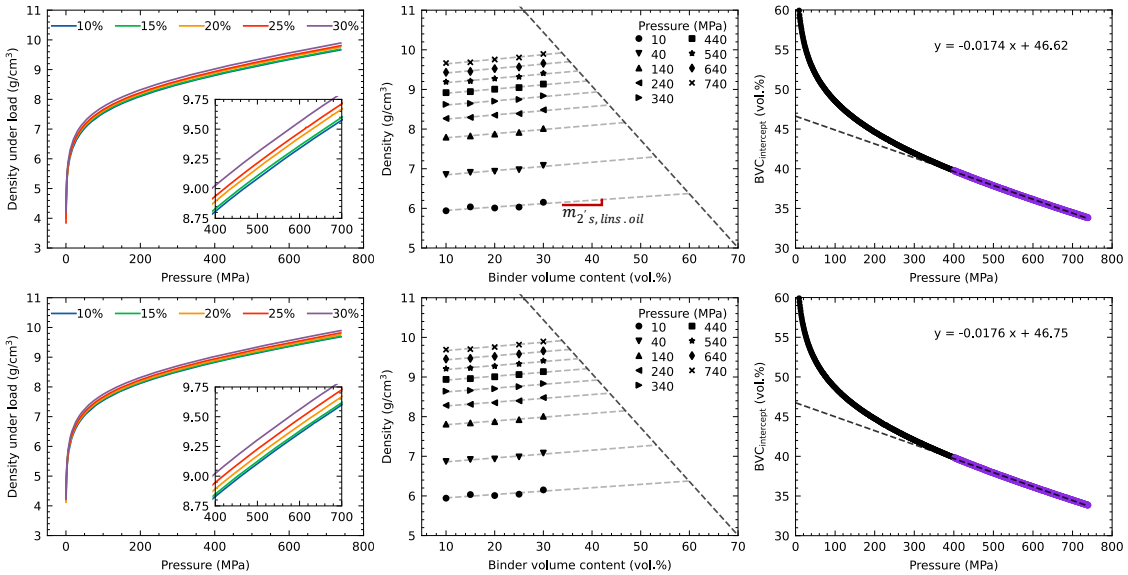

Figure 48: First mixing iteration of WC-Co powder with linseed oil. This figure presents the outcomes for determining the $CBVC_{P0}$ using the experimental model on fresh samples from the same mixing cycle. For each concentration, two compacts were pressed (the top is compact one and the bottom compact two). The average $CBVC_{P0}$ was determined to be 46.7 ± 0.1 vol.%. For clarity, only nine pressures are shown in the middle figure.

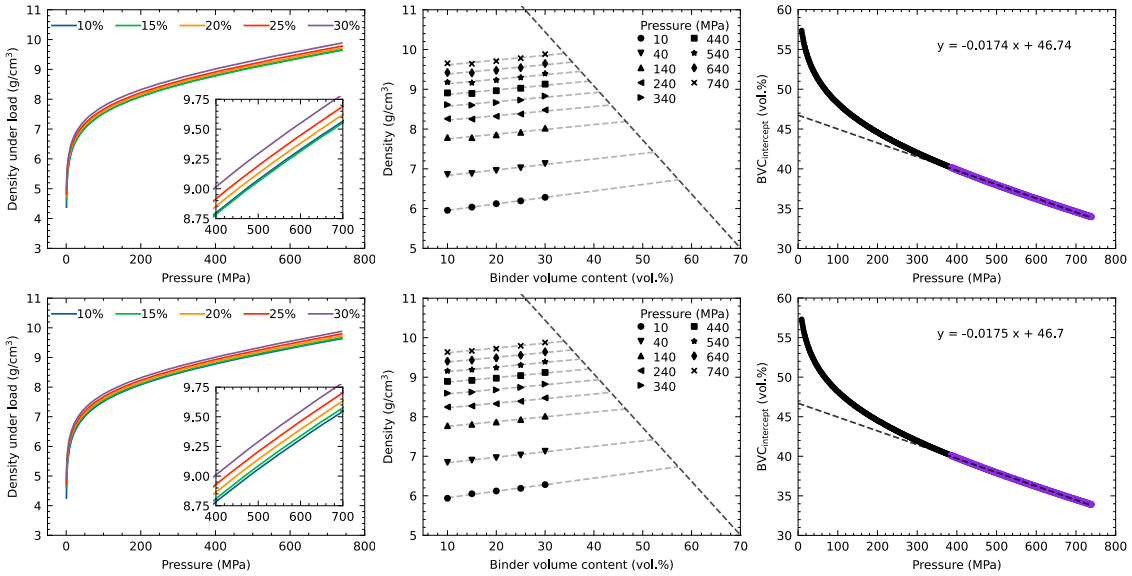

Figure 49: Second mixing iteration of WC-Co powder with linseed oil. This figure presents the outcomes for determining the $CBVC_{P0}$ using the experimental model on fresh samples from the same mixing cycle. For each concentration, two compacts were pressed (the top is compact one and the bottom compact two). The average $CBVC_{P0}$ was determined to be 46.7 ± 0.1 vol.%. For clarity, only nine pressures are shown in the middle figure.

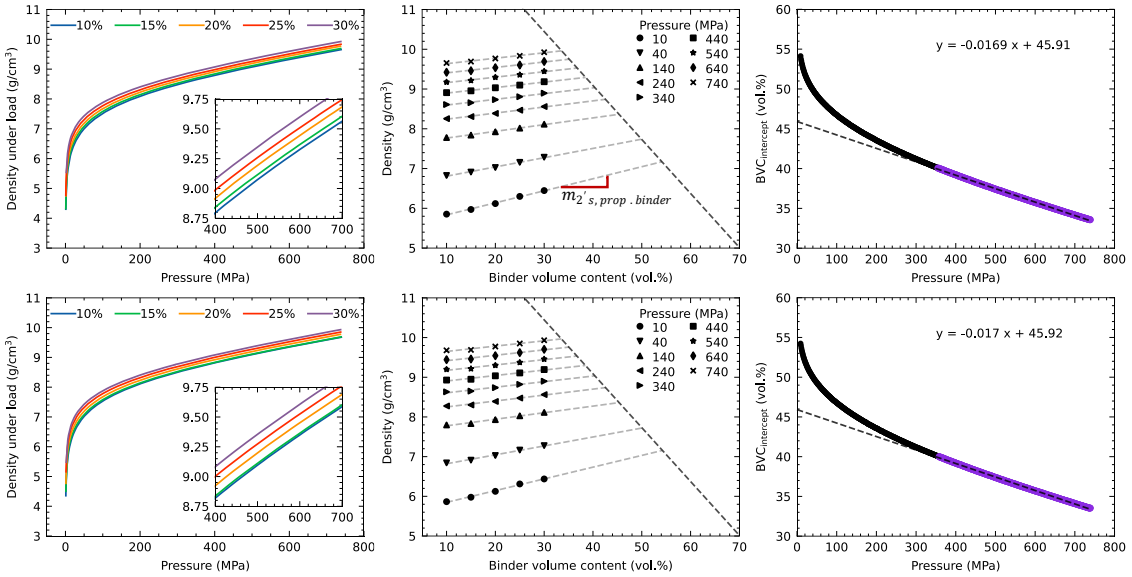

Figure 50: First mixing iteration of WC-Co powder with the proprietary binder. This figure presents the outcomes for determining the $CBVC_{P0}$ using the experimental model on fresh samples from the same mixing cycle. For each concentration, two compacts were pressed (the top is compact one and the bottom compact two). The average $CBVC_{P0}$ was determined to be 45.9 ± 0.1 vol.%. For clarity, only nine pressures are shown in the middle figure.

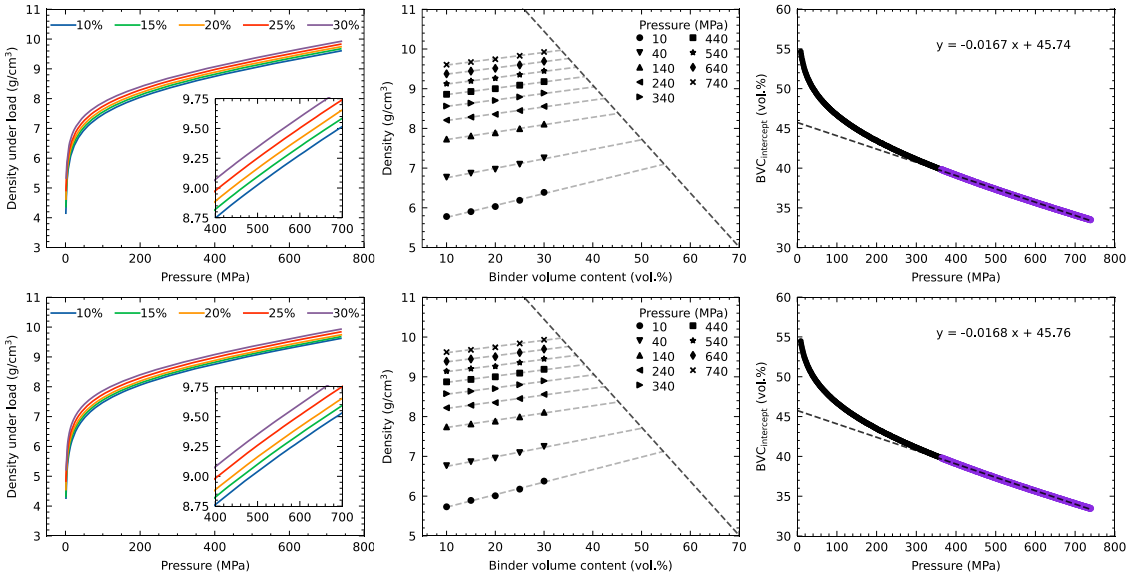

Figure 51: Second mixing iteration of WC-Co powder with the proprietary binder. This figure presents the outcomes for determining the $CBVC_{P0}$ using the experimental model on fresh samples from the same mixing cycle. For each concentration, two compacts were pressed (the top is compact one and the bottom compact two). The average $CBVC_{P0}$ was determined to be 45.7 ± 0.1 vol.%. For clarity, only nine pressures are shown in the middle figure.

4.3.5 Additional insights on $CBVC_{P0}$ method

4.3.5.1 Optimizing $CBVC_{P0}$ determination using different presses

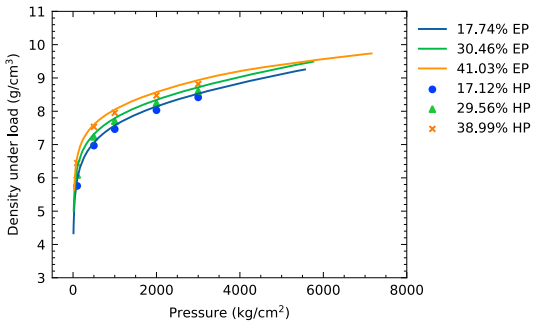

Figure 52: Compressed curves comparison between a manual hydraulic press (HP) and an automatic electric press (EP) for the nano RTP powder with linseed oil.

The $CBVC_{P0}$ determination can be conducted with any press capable of measuring compression force, as illustrated in Figure 52, which compares data from a manual hydraulic press (HP) and an automatic electric press (EP) for the nano system with linseed oil.

Both presses utilized the same die geometry, but the hydraulic press featured a floating die with a fixed upper punch. In contrast, the electric press was programmed to create a symmetric density gradient by moving the cavity and lower punch as the upper punch descended, generating the lower density region in the middle of the compact. Although the compacts from each press exhibited different density gradients, this did not affect the $CBVC_{P0}$ determination since density calculations were based on the height of compression.

For the manual press, each circular marker represents a single compression of a 15 g powder-binder mixture, requiring numerous compressions to plot the curve for a single concentration, thus demanding significant time and materials. The manual press was limited to 350 MPa, insufficient for higher-pressure testing necessary for analyzing the linear portion of the presented data. Therefore, the electric press, capable of exerting up to 750 MPa and equipped with automatic speed control, was used to investigate the densification behaviour at higher pressures.

Figure 52 demonstrates that results are reproducible regardless of the press type used and that the method is not influenced by different density gradients resulting from the two pressing techniques or press type. Consequently, due to its efficiency and reliability, the electric press was chosen as the standard for $CBVC_{P0}$determination.

4.3.5.2 Impact of compressing speed on $CBVC_{P0}$ determination

Maintaining a constant compression speed with a manual press is challenging due to variability in the operator's actions. In contrast, an electric press can consistently control compression speed. To evaluate the effect of compression speed, a third mixture was prepared and the $CVBC_{P0}$ determination was conducted at speeds of 2 mm/s and 5 mm/s

using an electric press for the nano system with linseed oil. In this iteration, only three concentrations were considered (10, 20, and 30 vol.%).

The standard speed for all experiments in this thesis was 2 mm/s. The $CVBC_{P0}$ values were 46.81 ± 0.1 for a compression speed of 2 mm/s and 46.74 ± 0.1 for 5mm/s. No significant difference in compaction capacity was observed, indicating similar compaction behaviour at the range of speeds tested. However, it is anticipated that at higher speeds (e.g., 30 mm/s), the powder's packing capacity could be negatively affected due to insufficient time for particle rearrangement, potentially leading to an increased $CBVC$.

4.3.5.3 Linearity of density under load in function of organic binder

One assumption of the uniaxial die method is that density under pressure increases linearly with organic content. However, Yarnton et al. [89] demonstrated that this is not true for concentrations below 5 vol.% by studying the lubrication effect of stearic acid on copper powder. Based on his findings, the validity of linearity at higher concentrations was questioned. By looking at the plots where isobars are extrapolated to determine the $BVC_{\text{intercepts}}$, the linearity has to be heavily extrapolated to the theoretical line at lower pressures compared to higher pressures. This raises the question of whether the data also behaves linearly at lower pressures in the zone of higher concentrations. To investigate this, experiments were conducted at higher binder contents.

The $CBVC$ determination procedure was repeated on the nano system using linseed oil as the titration medium. As shown in Figure 53, the tested concentrations were 10, 20, 30, 35, 40, 45, and 47 vol.%. In this experiment, the maximum compression pressure was not constant but was set to the highest possible value just before squeeze-out occurred for each concentration.

Figure 53 (left) shows the packing fraction as a function of pressure for each concentration, highlighting the point at which press and pycnometer densities equalize, beyond which squeeze-out occurs. In Figure 53 (middle), the data is rearranged as described in section 4.3.2. Linear behaviour at isobars is observed only for pressures exceeding 340 MPa, while at lower pressures (<340 MPa) and higher concentrations, the data exhibit non-linear behaviour.

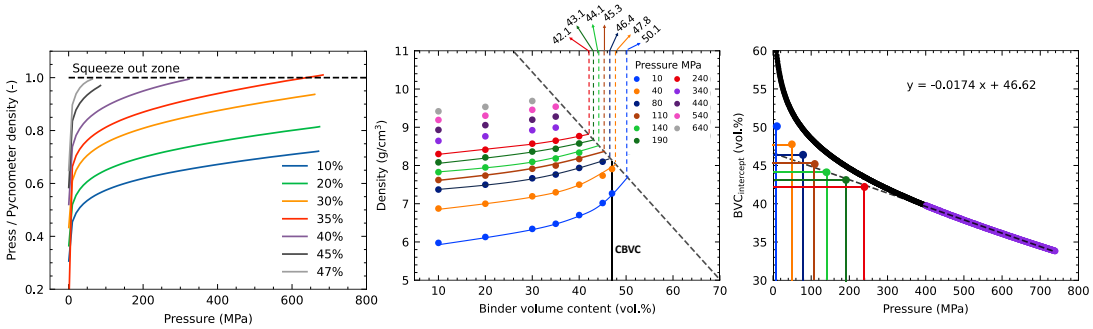

Figure 53: Linearity in $CBVC_{P0}$ curves.

The solid lines in Figure 53 (middle) are manually drawn to approximate the data. By extrapolating this data at constant pressure with a non-linear line towards the theoretical density fit, the $BVC_{\text{intercepts}}$ now align more closely with the initial linear fit seen in Figure 53 (right), it is expected that if a correct model is fitted to the data the $BVC_{\text{intercepts}}$ should coincide with the dashed line from Figure 53 (right). In addition, it is visible that the non-linearity in Figure 53 (middle) decreases with increasing pressure, which helps to identify the departure point in Figure 53 (right). The linearity observed at high pressures in Figure 53 (right) can primarily be attributed to elasticity, while the non-linearity at lower pressures is due to the inherent initial loose pack characteristic of powder systems.

4.4 The Role of Tungsten Carbide Grain Size on Powder Packing

The influence of grain size on the compressibility of several powders was assessed with the uniaxial die method by determining the $CBVC_{P0}$ for six WC powders with increasing grain size from 0.2 to 4.45 µm. The basic powder properties are displayed in Table 2, and in Figure 54 the grain size distribution as measured by laser diffraction is presented. The cumulative size distribution, shown in Figure 54 (right), provides the diameters d10, d50, and d90, which indicate that x% (e.g., x = 10%) of particles are smaller than the corresponding diameter in a polydisperse distribution. The Sauter mean diameter, representing the volume-to-surface ratio and thus the mean diameter of a polydisperse distribution is calculated from the size distribution in Figure 54 (left). For clarity, different powder systems are referred to by their powder class in subsequent discussions.

Pure WC powder is used instead of hard metal powder (WC-Co) to isolate the effect of particle size on packing capacity. Using commercial hard metal grades would complicate the study due to the varying grain sizes and Co phase quantities tailored for specific final properties. These variations introduce multiple variables (WC grain size, Co grain size, and WC-Co ratio), which would prevent a systematic study focused solely on WC particle size.

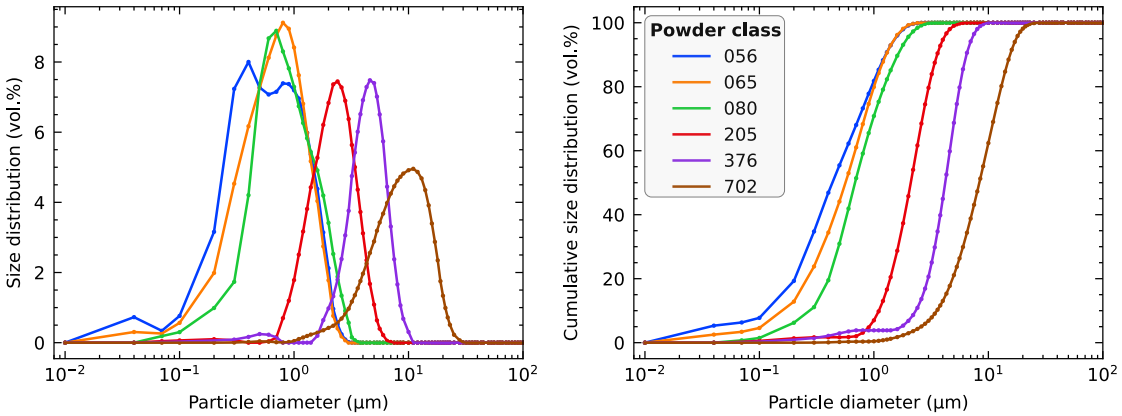

Figure 54: Volumetric grain size distribution (left) and cumulative volumetric size distribution (right) of the WC powders examined in this study.

In Figure 55 a scanning electron image for each powder is displayed, the WC grain increases from nano (top left) to micro (bottom right). The particles have an irregular shape with increasing Sauter mean diameter from 0.56 to 7.02 µm.

It is crucial to highlight that the pressing method utilizes the pycnometer densities from Table 2 to establish the theoretical density line for various WC-oil mixtures, employing a straightforward mixing rule (refer to Figure 56, middle). The $BVC_{\text{intercepts}}$, depicted in Figure 56 (right), denote the points where the theoretical density line intersects with the linear fits of the isobars. These intersections are directly influenced by the pycnometer

densities considered. Analysis of the pycnometer densities in Table 2 reveals a discernible trend: pycnometer density increases with larger WC grain size.

According to the literature [1], the theoretical density for WC is 15.7 g/cm^3, applicable when the powders consist solely of WC. Deviations from this theoretical value can be attributed to two primary factors. Smaller particles offer a larger surface area (visible in the BET measurements), which may heighten the likelihood of metal oxidation, thereby reducing density. Conversely, coarser particles may exhibit densities surpassing the theoretical value, possibly due to incomplete carburization resulting in W_2C or W, consequently increasing density. However, both phenomena may coexist within the examined powder system, differing in their magnitudes.

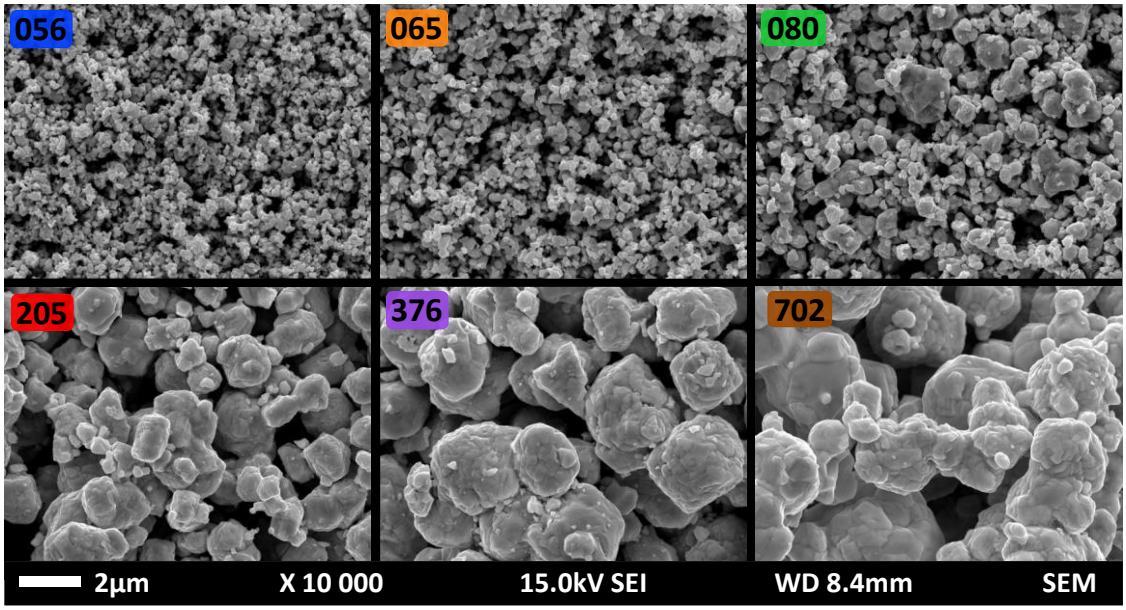

Figure 55: SEM of WC powders examined in this study.

Figure 56 illustrates the results of the pressing method. The graphs reveal patterns consistent with those reported in section 4.3.2. As the BVC increases, the compression process for each WC system achieves higher density states (Figure 56, middle). From these data, the $BVC_{intercepts}$ are obtained, showing an initial decrease during the densification phase involving particle rearrangement, followed by a linear region at higher pressures (Figure 56, right). These findings confirm that the method proposed in section 4.3 is applicable across a wide range of WC grain sizes.

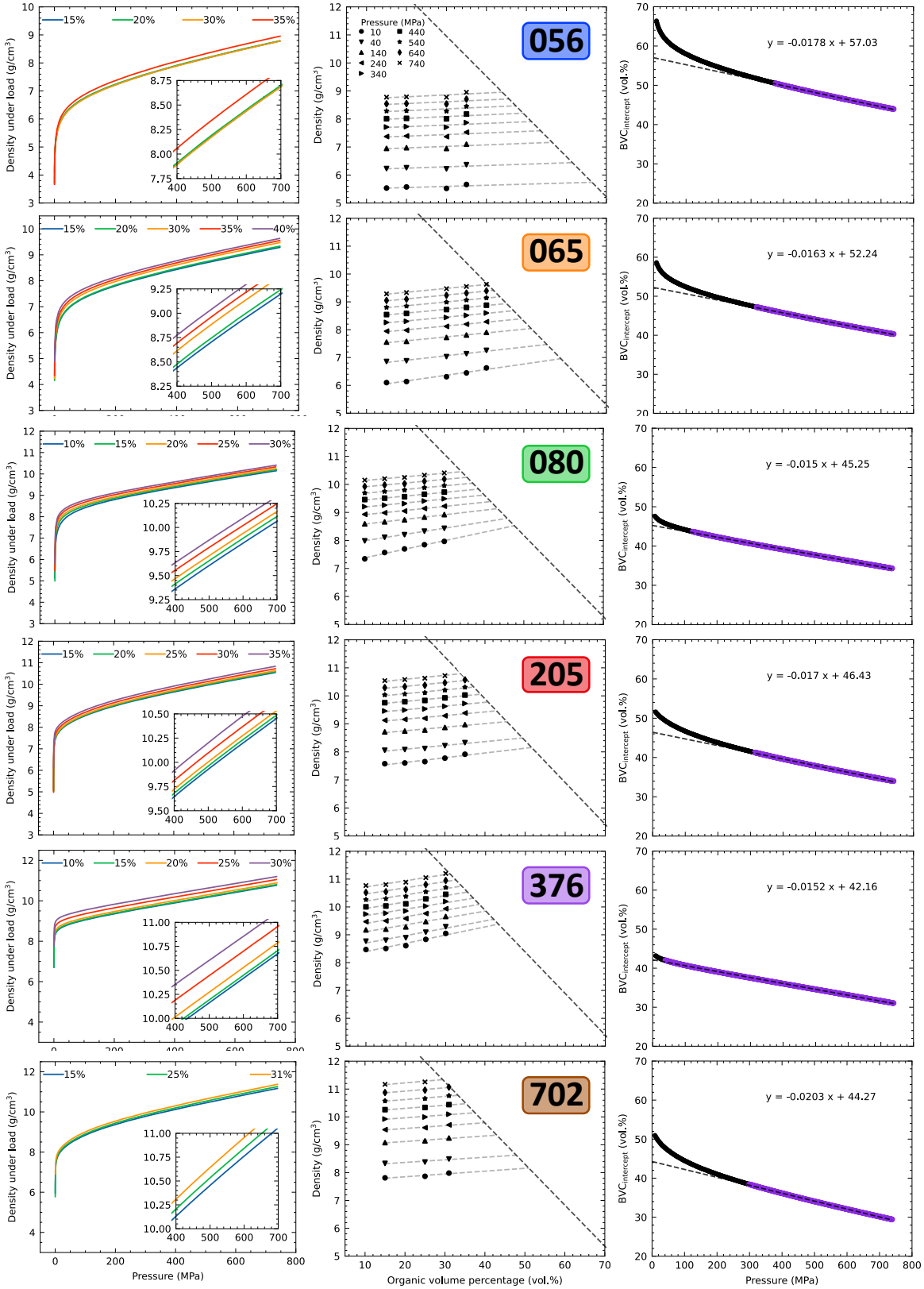

Figure 56: $CBVC_{P0}$ with linseed oil for WC powder with varying grain size.

A noteworthy observation arises when comparing the linear region in Figure 56 (right), indicated by the purple markers. For powders 080 and 376, the linearity of $BVC_{intercepts}$ starts at low pressures (120 and 40 MPa respectively), which contrasts with other systems (>300 MPa). This suggests that initial particle rearrangement occurs readily at low pressures, requiring less force to achieve higher packing densities.

Examining the cumulative particle size distributions in Figure 54 (right), powder 376 includes particles sized between 0.5-1 µm. The presence of these smaller particles likely improves packing ability at lower pressures, as they can move more easily and fill spaces between larger particles, leading to higher packing fractions at lower pressures.

However, it is important to note that the accuracy of laser diffraction measurements decreases for particles smaller than 0.1 µm. Given this limitation, it is possible that powder 080 also contains smaller particles that aid in achieving the $BVC_{intercepts}$ linearity at lower pressures, although they are not represented in the cumulative size distribution due to the measurement constraints.

Table 6 provides a summary of the results obtained from the press method and theoretical calculation. Both methods show a decrease of the $CBVC$ as the grain size increases. Notably, the theoretical calculation overestimates significantly the $CBVC$ and the disparity if greater at lower grain sizes. This is because as the grain size increases the frictional forces between powder particles reduce and the powder can pack better under the influence of tapping force alone. Conversely, for the smaller grain sizes, to decrease the free space higher forces need to be applied to densify the bulk [92]. Therefore, the packing density and $CBVC_{theo}$ obtained through theoretical calculation offers an inadequate representation of the packing density achieved during paste formation. These findings are consistent with the results presented in the section 4.2 for WC-Co powder systems [5].

Table 6: Summary of $CBVC$ as determined for different WC grain sizes.

Method	056	065	080	205	376	702
$CBVC_{Theo}$	82.22	79.68	67.53	63.39	57.07	57.46
$CBVC_{P0}$	57.03	52.24	45.25	46.43	42.16	44.27

Figure 57 shows the influence of grain size distribution, expressed by a mean diameter and the BET, on the $CBVC$ for WC powders with different grain sizes commonly used in the hard metal industry. The outcome shows a large influence of nano-sized WC grains on the acquired $CBVC's$ caused by interparticle contact phenomena such as interparticle friction.

As the mean grain size increases and the BET decreases, the $CBVC$ appears to be less dependent on the WC grain size. This outcome indicates that the processability of large grain-sized WC-based paste systems is very similar to one another under the condition that the organic binder type is identical for such systems.

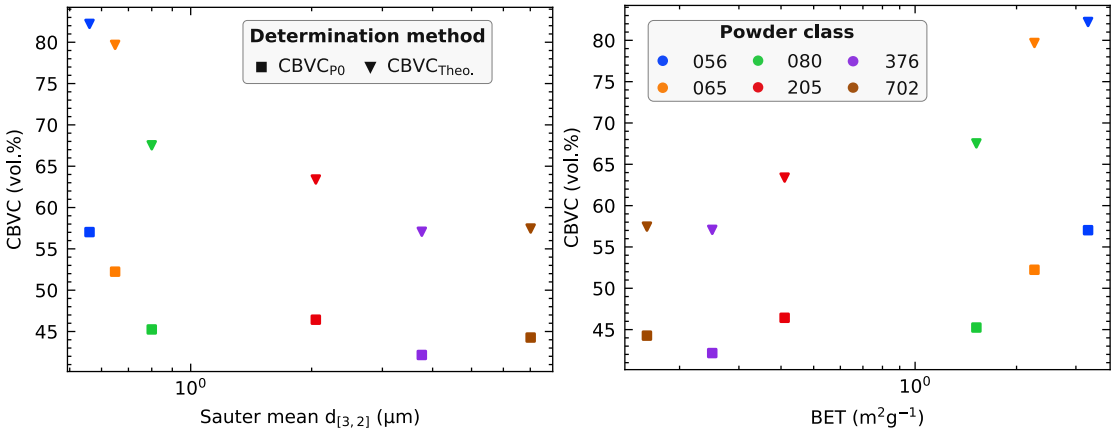

Figure 57: $CBVC_{P0}$ and $CBVC_{Theo}$ in function of WC grain size.

This study's findings elucidate the impact of grain size on feedstock preparation. On an industrial scale, even minor fluctuations in powder grain size due to natural variability in manufacturing processes can significantly affect powder packing efficiency. Variations in grain size exert a more pronounced influence on the rheological properties of feedstock in systems with smaller grains. Thus, $CBVC_{P0}$ could serve as a method to evaluate incoming powder batches for their packing ability. This information can guide process adjustments, such as binder quantity modification, to maintain consistent processing parameters.

5 CONCLUSION

Investigating the rheological properties of a system that received limited prior study, particularly a nano-grain-sized hard metal paste with low cobalt content, has contributed to identifying crucial factors affecting its flow properties. The reduced grain size of the material has posed significant challenges in both characterization and processing, adding to the complexity of the system. These challenges drove the need for deeper understanding and innovation, leading to the modification and development of characterization techniques. This effort culminated in a novel method for assessing critical binder volume content ($CBVC_{P0}$) and the definition of the zero-pressure density (ρ_{P0}).

5.1 Paste flow

The flow behaviour of the paste, composed of nano powder and the proprietary binder, was analysed via capillary rheometry. At 30°C, the paste exhibited shear thinning behaviour, making the Herschel-Bulkley model a suitable fit for the extrusion data.

The Bagley correction, which accounts for the pressure drop due to non-homogeneous flow as the feedstock travels from the barrel to the die, was successfully applied. The outcome showed that the entry effect significantly contributes to the overall pressure drop during extrusion. In contrast, the use of a zero-length capillary to correct for the entry effect proved ineffective for this system. Only the Bagley correction could predict the behaviour accurately. Given the non-Newtonian flow behaviour of the system, the Weissenberg-Rabinowitsch correction was applied to account for the non-parabolic velocity profile of the feedstock. These corrections allowed for a more accurate determination of the true viscosity by adjusting the apparent shear stress and shear rate.

Applying the Mooney correction to characterize wall slip resulted in negative velocities, indicating the inapplicability of this method. This is likely due to the paste extruding partially as plug flow, suggesting a considerable presence of slip where a thin layer of low-viscosity binder coats the capillary surface. This observation aligns with the near-zero initial bulk yield stress (τ_0) from the Benbow-Bridgwater model, confirming the excellent lubrication properties of the paste.

The six-parameter Benbow-Bridgwater (BB) model accurately describes the paste flow and was used to compare paste properties with those reported by other researchers for similar industrial applications (extrusion of rods). Despite the presence of sub-micron grain size of the powder in the paste, the system's viscosity was relatively low. This phenomenon was attributed to either the lower viscosity and better wetting properties of the proprietary binder or the higher binder quantity relative to the $CBVC$ of the nano system.

5.2 Traditional methods for *CBVC* determination

The $CBVC$ is a key parameter for enhancing paste properties, representing the threshold at which the bulk material transitions from behaving like a powder to behaving like a paste. In paste processing, knowing the optimal binder content is crucial for formulating a feedstock with optimal characteristics. At concentrations higher than $CBVC$, particle-particle lubrication starts to happen. However, an excess of binder is required to form a paste that can ease the flow when the system is subjected to am external force.

This study investigated the $CBVC$ using various methods, including theoretical calculation, oil titration, binder titration, and Reddy's model. The findings indicate that theoretical and oil titration methods consistently overestimate $CBVC$ compared to binder titration and Reddy's model. The discrepancies in oil titration are attributed to differences in wettability and viscosity between the oil and the proprietary binder. However, binder titration and Reddy's model produce similar results. It is important to note that the accuracy of titration methods depends on the size of the binder addition step, while Reddy's model, although more labour-intensive, is independent of this factor.

The results obtained in section 4.2 underscore the need for careful interpretation of $CBVC$ based on the method used and highlight the importance of utilizing the actual binder system that will be used for processing in titration experiments since the results considerably vary upon the properties of the titration media Finally, the micro system showed a lower $CBVC_{titra}$ when compared to the nano system.

5.3 Proposed *CBVC* determination technique

Variations in $CBVC$ results obtained with diverse methods suggest that each method determine different particle arrangements. Section 4.3 introduced a technique that yields the minimum $CBVC$ value compared to other methods, denoted as $CBVC_{P0}$. This value is perceived as being less pendent of the binder type. Furthermore, this quantity is linked to the densest packing, a physical property of the powder that determines the optimal particle arrangement for practical applications.

The usage of a uniaxial die press helps to approach to the maximum packing arrangement of the powder. It is worth noting that the ideal binder content for industrial applications will be higher than the $CBVC_{P0}$, as filling all free voids with an organic binder at maximum packing density would not coincide with the ideal conditions for extrusion or injection moulding, since a surplus of binder is required for efficient lubrication during processing.

This technique demands less material than Reddy's model and circumvents potential complications arising from intricate extrusion behaviour. Moreover, in contrast to conventional titration methods, it exhibits less sensitivity to mixing parameters such as temperature, blade speed, and titration quantity. The uniaxial die press method assumes that particle deformation is strictly elastic within the tested pressure range. The applicability of this method is validated for nano-sized WC-Co hard metal powders with a low metallic binder content.

5.4 Influence of WC grain size on $CBVC_{P0}$

In section 4.4, the applicability of the $CBVC_{P0}$ technique was extended to a broader range of powders. The methodology was successfully applied to six pure tungsten carbide (WC) powder with varying grain sizes which have Sauter mean diameters ranging from 0.56 to 7.02 µm. A clear dependency of $CBVC_{P0}$ on grain size was observed: as the grain size approached submicron levels, the $CBVC_{P0}$ significantly increased; for powders with coarser grain sizes, the $CBVC_{P0}$ remained more constant, fluctuating around 44.5 vol.%. Additionally, the results showed that a minor portion of smaller grain sizes in a powder system significantly reduced the $CBVC_{P0}$ and enable the achievement of higher packings at lower pressures.

6 OUTLOOK

The topics discussed here could serve as content for further investigation.

- The established rheological models can be utilized for simulating the flow of nano hard metal paste. This simulation will aid in optimizing extrusion processes by predicting flow behaviour under various conditions, leading to improved process control and material properties.
- Future research could focus on developing and testing new binder compositions tailored to specific powder systems, further enhancing the paste's flow behaviour and processing performance. More specifically, the effect of grafted polymers on the rheological properties and processability of hard metals paste compared to conventional surfactants.
- Future research could broaden the $CBVC_{P0}$ methodology to hard metals with larger grains or varying cobalt contents and investigate the notion of zero-pressure density for other types of powders, including ceramics and metals. It could also be applied to several batches of the same powder to determine if this parameter captures the normal variability of industrial-scale powder production and evaluate if it can serve as a quality control measure.

7 PUBLICATIONS

Journal papers

A. Medina Peschiutta, M. Just, R. Useldinger, J. Baller, The zero-pressure density and its determination on hard powders with varying particle size: a novel characterization technique, (2024) Preparing draft for submission in an open access journal.

A. Medina Peschiutta, M. Just, R. Useldinger, J. Baller, Assessing critical binder volume concentration using uniaxial die pressing: An alternative approach, *Powder Technol.* 443 (2024) 119968. https://doi.org/10.1016/j.powtec.2024.119968.

M. Just, A. Medina Peschiutta, F. Hippe, R. Useldinger, and J. Baller, "Determination of the angle of repose of hard metal granules," *Powder Technol.*, vol. 407, no. July, p. 117695, 2022, doi: 10.1016/j.powtec.2022.117695.

M. Just, A. Medina Peschiutta, F. Hippe, R. Useldinger, and J. Baller, "Gravitational mass flow measurements of various granular materials in relation to an extended Bond number," *Int. J. Refract. Met. Hard Mater.*, vol. 112, no. October 2022, p. 106142, 2023, doi: 10.1016/j.ijrmhm.2023.106142.

Conference papers

A. Medina Peschiutta, M. Just, R. Useldinger, and J. Baller, "Comparative Analysis of Methods for Determining the Critical Binder Volume Concentration in Hard Metal Pastes," in *Euro PM 2023 Congress and Exhibition*, 2023, doi: 10.59499/EP235764669.

M. Just, A. Medina Peschiutta, Useldinger, and J. Baller, "Maximum in mass flow rates of hard metal granules through circular orifices in relation to the angle of repose", in *Euro PM 2023 Congress and Exhibition*, 2023. doi: 10.59499/EP235765170.

M. Just, A. Medina Peschiutta, F. Hippe, R. Useldinger, and J. Baller, "Gravitational mass flow measurements of various granular materials in relation to an extended Bond number," in *20th Plansee Seminar*, Reutte 2022.

Posters

M. Just, A. Medina Peschiutta, F. Hippe, R. Useldinger, and J. Baller, "Understanding the flow of hard metal powders and pastes", in *MRT/DPhyMS PhD day and DPPM General Assembly*, Luxembourg 2022. doi: 10.13140/RG.2.2.27687.93608.

M. Just, A. Medina Peschiutta, Useldinger, and J. Baller, "Maximum in mass flow rates of hard metal granules through circular orifices in relation to the angle of repose", in *Euro PM 2023 Congress and Exhibition*, 2023. doi: 10.13140/RG.2.2.21641.25447.

8 REFERENCES

[1] E. Lassner, W.-D. Schubert, Tungsten - Properties, Chemistry, Technology of the Element, Alloys, and Chemical Compounds, 1st ed., Springer, New York, 1999. https://doi.org/https://doi.org/10.1007/978-1-4615-4907-9.

[2] S. W. H. Yih, W. Chun T., Tungsten Sources, Metallurgy, Properties, and Applications, 1st ed., Plenum Press, London, 1979.

[3] H.M. Ortner, P. Ettmayer, H. Kolaska, The history of the technological progress of hardmetals, Int. J. Refract. Met. Hard Met. 44 (2014) 148–159. https://doi.org/10.1016/j.ijrmhm.2013.07.014.

[4] G.S. Upadhyaya, Cemented Tungsten Carbides: Production, Properties and Testing, 1st ed., William Andrew, New Jersey, 1999.

[5] A. Medina Peschiutta, M. Just, R. Useldinger, J. Baller, Comparative Analysis of Methods for Determining the Critical Binder Volume Concentration in Hard Metal Pastes, in: Euro PM 2023 Congr. Exhib., European Powder Metallurgy Association, Lisbon, 2023. https://doi.org/10.59499/EP235764669.

[6] A.B. Ariawan, S. Ebnesajjad, S.G. Hatzikiriakos, Paste extrusion of polytetrafluoroethylene (PTFE) fine powder resins, Can. J. Chem. Eng. 80 (2002) 1153–1165. https://doi.org/10.1002/cjce.5450800617.

[7] R.M. German, A. Bose, Binder and polymer assisted powder processing, ASM International, Ohio, 2020.

[8] C. Kukla, S. Cano, C. Holzer, J. Gonzalez-Gutierrez, Influence of stearic acid in feedstocks for FFF and PIM, in: Euro PM 2019 Congr. Exhib., European Powder Metallurgy Association, Maastricht, 2019.

[9] P. Cao, M.D. Hayat, Design strategy of binder systems and feedstock chemistry, in: Feed. Technol. React. Met. Inject. Molding, Elsevier, Auckland, 2020: pp. 43–85. https://doi.org/10.1016/b978-0-12-817501-9.00002-8.

[10] R.M. German, A. Bose, Injection Molding of Metals and Ceramics, Metal Powder Industries Federation, New Jersey, 1997.

[11] M. Bek, J. Gonzalez-Gutierrez, C. Kukla, B. Maroh, L.S. Perše, Rheological Behaviour of Highly Filled Materials for Injection Moulding and Additive Manufacturing : Effect of

Particle Material and Loading, Appl. Sci. 10 (2020) 7993. https://doi.org/10.3390/app10227993.

[12] J. Gonzalez-Gutierrez, Indirect Additive Manufacturing Techniques for Metal Parts: Binder-Based Additive Manufacturing Techniques, Encycl. Mater. Met. Alloy. (2021) 319–329. https://doi.org/10.1016/B978-0-12-819726-4.00100-9.

[13] S. Cano, A. Gooneie, C. Kukla, G. Rieb, C. Holzer, J. Gonzalez-Gutierrez, Modification of interfacial interactions in ceramic-polymer nanocomposites by grafting: Morphology and properties for powder injection molding and additive manufacturing, Appl. Sci. 10 (2020). https://doi.org/10.3390/app10041471.

[14] M.M. Rueda, M.C. Auscher, R. Fulchiron, T. Périé, G. Martin, P. Sonntag, P. Cassagnau, Rheology and applications of highly filled polymers: A review of current understanding, Prog. Polym. Sci. 66 (2017) 22–53. https://doi.org/10.1016/j.progpolymsci.2016.12.007.

[15] L. Ammosova, S. Cano, S. Schuschnigg, C. Kukla, K. Mönkkönen, M. Suvanto, J. Gonzalez-Gutierrez, Effect of metal particle size and powder volume fraction on the filling performance of powder injection moulded parts with a microtextured surface, Precis. Eng. 72 (2021) 604–612. https://doi.org/10.1016/j.precisioneng.2021.06.014.

[16] T. Hanemann, R. Heldele, Modern Alchemy : Ceramic Feedstock Optimization by Surfactant Screening, Process Eng. 87 (2010) 38–41.

[17] J. Gonzalez-Gutierrez, Y. Thompson, D. Handl, S. Cano, S. Schuschnigg, P. Felfer, C. Kukla, C. Holzer, C. Burkhardt, Powder content in powder extrusion moulding of tool steel: Dimensional stability, shrinkage and hardness, Mater. Lett. 283 (2021) 128909. https://doi.org/10.1016/j.matlet.2020.128909.

[18] J. Bricout, J.C. Gelin, C. Ablitzer, P. Matheron, M. Brothier, Influence of powder characteristics on the behaviour of PIM feedstock, Chem. Eng. Res. Des. 91 (2013) 2484–2490. https://doi.org/10.1016/j.cherd.2013.02.023.

[19] P. Thomas-Vielma, A. Cervera, B. Levenfeld, A. Várez, Production of alumina parts by powder injection molding with a binder system based on high density polyethylene, J. Eur. Ceram. Soc. 28 (2008) 763–771. https://doi.org/10.1016/j.jeurceramsoc.2007.08.004.

[20] E. Hnatkova, B. Hausnerova, P. Filip, Evaluation of powder loading and flow properties of Al2O3 ceramic injection molding feedstocks treated with stearic acid, Ceram. Int. 45 (2019) 20084–20090.

https://doi.org/10.1016/j.ceramint.2019.06.273.

[21] F. Liu, K. Chou, Determining critical ceramic powder volume concentration from viscosity measurements, Ceram. Int. 26 (2000) 159–164. https://doi.org/10.1016/S0272-8842(99)00035-8.

[22] Z. Chen, K. Ikeda, T. Murakami, T. Takeda, Effect of particle packing on extrusion behavior of pastes, J. Mater. Sci. 35 (2000) 5301–5307. https://doi.org/10.1023/A:1004834526344.

[23] C. Abajo, A. Jiménez-Morales, J.M. Torralba, Solid loading optimisation of extremely irregular particles, in: Euro PM 2014 Congr. Exhib., European Powder Metallurgy Association, Salzburg, 2014. https://www.epma.com/publications/euro-pm-proceedings/product/euro-pm2014-powder-injection-moudling-modelling-and-processing.

[24] J. Hidalgo, A. Jiménez-Morales, J.M. Torralba, Torque rheology of zircon feedstocks for powder injection moulding, J. Eur. Ceram. Soc. 32 (2012) 4063–4072. https://doi.org/10.1016/j.jeurceramsoc.2012.06.023.

[25] M.E. Sotomayor, B. Levenfeld, A. Várez, Powder injection moulding of premixed ferritic and austenitic stainless steel powders, Mater. Sci. Eng. A. 528 (2011) 3480–3488. https://doi.org/10.1016/j.msea.2011.01.038.

[26] J.M. Torralba, J. Hidalgo, A. Jiménez-Morales, Powder injection moulding: Processing of small parts of complex shape, Int. J. Microstruct. Mater. Prop. 8 (2013) 87–96. https://doi.org/10.1504/IJMMP.2013.052648.

[27] X. Kong, T. Barriere, J.C. Gelin, Determination of critical and optimal powder loadings for 316L fine stainless steel feedstocks for micro-powder injection molding, J. Mater. Process. Technol. 212 (2012) 2173–2182. https://doi.org/10.1016/j.jmatprotec.2012.05.023.

[28] M.E. Sotomayor, A. Varez, B. Levenfeld, Influence of powder particle size distribution on rheological properties of 316L powder injection moulding feedstocks, Powder Technol. 200 (2010) 30–36. https://doi.org/10.1016/j.powtec.2010.02.003.

[29] M.H.I. Ibrahima, N. Muhamadband, A.B. Sulongb, Rheological Investigation of Water Atomised Stainless Steel Powder for Micro Metal Injection Molding, Int. J. Mech. Mater. Eng. 4 (2009) 1–8. https://www.researchgate.net/publication/279580099_Rheological_investigation_of_water_atomised_stainless_steel_powder_for_micro_metal_injection_molding.

[30] B. Hausnerova, B.N. Mukund, D. Sanetrnik, Rheological properties of gas and water

atomized 17-4PH stainless steel MIM feedstocks: Effect of powder shape and size, Powder Technol. 312 (2017) 152–158. https://doi.org/10.1016/j.powtec.2017.02.023.

[31] J. Hidalgo, A. Jiménez-Morales, T. Barriere, J.C. Gelin, J.M. Torralba, Water soluble Invar 36 feedstock development for μPIM, J. Mater. Process. Technol. 214 (2014) 436–444. https://doi.org/10.1016/j.jmatprotec.2013.09.014.

[32] J. Hidalgo, A. Jiménez-Morales, T. Barriere, J.C. Gelin, J.M. Torralba, Capillary rheology studies of INVAR 36 feedstocks for powder injection moulding, Powder Technol. 273 (2015) 1–7. https://doi.org/10.1016/j.powtec.2014.12.027.

[33] J.M. Contreras, A. Jiménez-Morales, J.M. Torralba, Experimental and theoretical methods for optimal solids loading calculation in MIM feedstocks fabricated from powders with different particle characteristics, Powder Metall. 53 (2010) 34–40. https://doi.org/10.1179/003258909X12450768327225.

[34] C. Dimitri, S. Mohamed, B. Thierry, G. Jean-claude, Influence of particle-size distribution and temperature on the rheological properties of highly concentrated Inconel feedstock alloy 718, Powder Technol. 322 (2017) 273–289. https://doi.org/10.1016/j.powtec.2017.08.049.

[35] J.M. Contreras, A. Jiménez-Morales, J.M. Torralba, Fabrication of bronze components by metal injection moulding using powders with different particle characteristics, J. Mater. Process. Technol. 209 (2009) 5618–5625. https://doi.org/10.1016/j.jmatprotec.2009.05.021.

[36] S.M. Majdi, A.A. Tafti, V. Demers, G. Vachon, V. Brailovski, Effect of powder particle shape and size distributions on the properties of low-viscosity iron-based feedstocks used in low-pressure powder injection moulding, Powder Metall. 0 (2021) 1–11. https://doi.org/10.1080/00325899.2021.1959696.

[37] R. Côté, M. Azzouni, V. Demers, Impact of binder constituents on the moldability of titanium-based feedstocks used in low-pressure powder injection molding, Powder Technol. 381 (2021) 255–268. https://doi.org/10.1016/j.powtec.2020.12.008.

[38] O. Ghanmi, V. Demers, Molding properties of titanium-based feedstock used in low-pressure powder injection molding, Powder Technol. 379 (2021) 515–525. https://doi.org/10.1016/j.powtec.2020.10.068.

[39] A. Fayyaz, N. Muhamad, A.B. Sulong, J. Rajabi, Y.N. Wong, Fabrication of cemented tungsten carbide components by micro-powder injection moulding, J. Mater. Process. Technol. 214 (2014) 1436–1444.

https://doi.org/10.1016/j.jmatprotec.2014.02.006.

[40] B. Blackham, S. Blackburn, N. Rowson, I. Al-Dawery, The Effect Of Solids Loading On The Performance Of Extrusion Feedstock Of Cemented Carbide, in: Euro PM 2012 Congr. Exhib., European Powder Metallurgy Association, Basel, 2012. https://www.epma.com/publications/product/ep12326.

[41] S.N.A. Shahbudin, S.Y.M. Amin, M.H. Othman, M.H.I. Ibrahim, Critical powder loading and the rheology of Nanosized cemented carbide with titanium carbide as grain growth inhibitor for injection molding, Int. J. Integr. Eng. 10 (2018) 114–118. https://doi.org/10.30880/ijie.2018.10.04.019.

[42] S.Y.M. Amin, N. Muhamad, K.R. Jamaludin, A. Fayyaz, H.S. Yunn, Characterization of the Feedstock Properties of Metal Injection-molded WC-Co with Palm Stearin Binder System, Sains Malaysiana. 43 (2014) 123–128. https://www.researchgate.net/publication/288221346_Characterization_of_the_Feedstock_Properties_of_Metal_Injection-molded_WC-Co_with_Palm_Stearin_Binder_System.

[43] B. Hausnerová, P. Sáha, J. Kubát, Capillary Flow of Hard-Metal Carbide Powder Compounds, Int. Polym. Process. 14 (1999) 254–260. https://doi.org/10.3139/217.1556.

[44] B. Hausnerova, P. Sáha, J. Kubát, T. Kitano, J. Becker, Rheological behaviour of hard-metal carbide powder suspensions at high shear rates, J. Polym. Eng. 20 (2000) 237–266. https://doi.org/10.1515/POLYENG.2000.20.4.237.

[45] A. Fayyaz, N. Muhamad, A.B. Sulong, H.S. Yunn, S.Y.M. Amin, J. Rajabi, Micro-powder injection molding of cemented tungsten carbide: Feedstock preparation and properties, Ceram. Int. 41 (2015) 3605–3612. https://doi.org/10.1016/j.ceramint.2014.11.022.

[46] Anton-Paar, Basics of viscometry, (n.d.). https://wiki.anton-paar.com/ca-en/basic-of-viscometry/ (accessed January 25, 2024).

[47] S. Goodyer, Measuring polymers using a rotational rheometer in oscillatory mode, Anton-Paar. (n.d.). http://www.t-p-a.org/archive/papers/15052013/Measuring_Polymers_using_a_Rotational_Rheometer_in_Oscillatory_Mode.pdf (accessed January 29, 2024).

[48] T.G. Mezger, The Rheology Handbook, 5th ed., Vincentz Network GmbH, Hanover, 2020. https://doi.org/10.1108/prt.2009.12938eac.006.

[49] A. Rock, R.E. Hincapie, M. Tahir, N. Langanke, On the Role of Polymer Viscoelasticity

in Enhanced Oil Recovery: Extensive Laboratory Data and Review, Polymers (Basel). 12 (2020) 2276. https://doi.org/https://doi.org/10.3390/polym12102276.

[50] F.A. Morrison, Understanding Rheology, 1st ed., Oxford University Press, New York, 2001. https://global.oup.com/ushe/product/understanding-rheology-9780195141665?cc=us&lang=en&.

[51] T.G. Mezger, The Rheology Handbook, 4th ed., Vincentz Network, Hanover, 2010. https://doi.org/10.1108/ijppm.2010.07959dab.003.

[52] C.W. Macosko, Rheology: Principles, Measurements and Applications, WILEY-VCH, New York, 1996. https://doi.org/10.1016/s0032-5910(96)90008-x.

[53] GOTTFERT, Corrections of Capillary Rheometer Experiments, (n.d.). https://www.goettfert.com/application-knowledge/rheo-info/for-capillary-rheometer/corrections-of-capillary-rheometer-experiments (accessed June 24, 2024).

[54] F.A. Morrison, Notes on Capillary Flow Corrections, 2006.

[55] M. Li, L. Tang, R.G. Landers, M.C. Leu, Extrusion process modeling for aqueous-based ceramic pastes-part 1: Constitutive model, J. Manuf. Sci. Eng. 135 (2013) 1–8. https://doi.org/10.1115/1.4025014.

[56] A.Y. Malkin, A. V. Baranov, M.E. Vickulenkova, Experimental estimation of wall slip for filled rubber compounds, Rheol. Acta. 32 (1993) 150–155. https://doi.org/10.1007/BF00366678.

[57] A. Gansen, M. Řehoř, C. Sill, P. Polińska, S. Westermann, J. Dheur, J.S. Hale, J. Baller, Experimental separation of the onset of slip and sharkskin melt instabilities during the extrusion of silica - filled , styrene – butadiene rubber compounds, Rheol. Acta. 62 (2023) 15–30. https://doi.org/10.1007/s00397-022-01376-7.

[58] A. Gansen, J. Hennicker, C. Sill, J. Dheur, J.S. Hale, J. Baller, Melt Instability Identification Using Unsupervised Machine Learning Algorithms, 308 (2023) 2200628. https://doi.org/10.1002/mame.202200628.

[59] S. Westermann, J. Dheur, A. Gansen, Ř. Martin, C. Sill, P. Poli, J.S. Hale, J. Baller, Investigation of the Sharkskin melt instability using optical Fourier analysis, 137 (2020) 48806. https://doi.org/10.1002/app.48806.

[60] M. Mooney, Explicit Formulas for Slip and Fluidity, J. Rheol. (N. Y. N. Y). 2 (1931) 210–222. https://doi.org/10.1122/1.2116364.

[61] C.I. Hicks, H. See, The rheological characterisation of bread dough using capillary

rheometry, Rheol. Acta. 49 (2010) 719–732. https://doi.org/10.1007/s00397-010-0441-1.

[62] N. Ghahramani, G.C. Georgiou, E. Mitsoulis, S.G. Hatzikiriakos, J.G. Oldroyd's early ideas leading to the modern understanding of wall slip, J. Nonnewton. Fluid Mech. 293 (2021) 104566. https://doi.org/10.1016/j.jnnfm.2021.104566.

[63] B.L. Blackham, The development of a binder system and process for the manufacture of large diameter tungsten carbide drill blanks, University of Birmingham, 2015. http://etheses.bham.ac.uk/5592/.

[64] H. Ayton, Modelling the Extrusion of a Hard-Metal Paste, University of Cambridge, 2020. https://doi.org/https://doi.org/10.17863/CAM.70213.

[65] J. Benbow, J. Bridgewater, Paste flow and extrusion, Oxford Univ. Press. 41 (1993) 1995.

[66] H. Ferstl, Extrusion and drying of a hardmetal paste, University of Cambridge, 2013. https://doi.org/10.17863/CAM.11761.

[67] R.B. Wilmot, R. Barbist, H. Ferstl, C. Gruber, W. Brandstatter, M.J. Patel, D.I. Wilson, Characterisation and Design of Wax-Based Hard Metal Extrusion Processes, in: 17th Plansee Semin. Int. Conf. High Perform. P/M Mater., Plansee Holding AG, Reutte, 2009.

[68] Granutools, GranuPack: High resolution tapped density analyzer, (n.d.). https://www.granutools.com/en/granupack (accessed June 19, 2024).

[69] N. Wonderling, G. Tambourine, Density: Helium Pycnometry, PennState Mater. Reseach Institude. (n.d.). https://www.mri.psu.edu/materials-characterization-lab/characterization-techniques/density-helium-pycnometry (accessed June 19, 2024).

[70] Anton-Paar, Laser diffraction for particle sizing, (n.d.). https://wiki.anton-paar.com/uk-en/laser-diffraction-for-particle-sizing/#c38942 (accessed June 20, 2024).

[71] R.C. Silva, Experimental Characterization Techniques for Solid-Liquid Slurry Flows in Pipelines : A Review, Processes. 10 (2022) 597. https://doi.org/10.3390/pr10030597.

[72] P.B. Kowalczuk, J. Drzymala, Physical Meaning of the Sauter Mean Diameter of Spherical Particulate Matter Physical meaning of the Sauter mean diameter of spherical particulate matter, Part. Sci. Technol. 34 (2019) 645–647. https://doi.org/10.1080/02726351.2015.1099582.

[73] Anton-Paar, BET Theory, (n.d.). https://wiki.anton-paar.com/en/bet-theory/ (accessed June 21, 2024).

[74] M. Naderi, Surface Area: Brunauer–Emmett–Teller (BET), in: S. Tarleton (Ed.), Prog. Filtr. Sep., Academic Press, London, 2015: pp. 585–608. https://doi.org/10.1016/B978-0-12-384746-1.00014-8.

[75] G.W.H. Hohne, W.F. Hemminger, H.-J. Flammersheim, Differential scanning calorimetry, Springer, Berlin, 2014. https://doi.org/10.3139/9781569906446.007.

[76] G.W.H. Höhne, W. Hemminger, H.J. Flammersheim, Differential Scanning Calorimetry: An introduction for Practitioners, Springer, Berlin, 1996. https://doi.org/10.1007/978-3-662-03302-9_5.

[77] F. Händle, The Art of Ceramic Extrusion, Mühlacker, 2019. https://doi.org/10.1007/978-3-030-05255-3.

[78] S. Wiegreffe, Untersuchungen zum Wandgleitverhalten von EPDM und SBR, Kautschuk Und Gummi, Kunststoffe. 44 (1991) 216–221.

[79] L. Malagutti, F. Mollica, V. Mazzanti, Error amplification in capillary viscometry of power law fluids with slip, Polym. Test. 91 (2020) 106816. https://doi.org/10.1016/j.polymertesting.2020.106816.

[80] P.J. Martin, D.I. Wilson, A critical assessment of the Jastrzebski interface condition for the capillary flow of pastes, foams and polymers, Chem. Eng. Sci. 60 (2005) 493–502. https://doi.org/10.1016/j.ces.2004.08.011.

[81] Z. Jastrzebski, Entrance effects and wall effects in an extrusion rheometer during the flow of concentrated suspensions, Exp. Tech. 6 (1967) 445–454.

[82] L.J. Wells, S.A. Nightingale, G.M. Spinks, The effect of temperature on the extrusion behavior of a polymer/ceramic refractory paste, J. Mater. Sci. 40 (2005) 315–321. https://doi.org/10.1007/s10853-005-6084-4.

[83] J. Gonzalez-Gutierrez, I. Duretek, C. Kukla, A. Poljšak, M. Bek, I. Emri, C. Holzer, Models to predict the viscosity of metal injection molding feedstock materials as function of their formulation, Metals (Basel). 6 (2016) 129. https://doi.org/10.3390/met6060129.

[84] J.W. Oh, R. Bollina, W.S. Lee, S.J. Park, Effect of nanopowder ratio in bimodal powder mixture on powder injection molding, Powder Technol. 302 (2016) 168–176. https://doi.org/10.1016/j.powtec.2016.08.051.

[85] J.J. Reddy, M. Vijayakumar, T.R.R. Mohan, P. Ramakrishnan, Loading of Solids in a

Liquid Medium: Determination of CBVC by Torque Rheometry, J. Eur. Ceram. Soc. 16 (1996) 567–574. https://doi.org/10.1016/0955-2219(95)00165-4.

[86] J.J. Reddy, N. Ravi, M. Vijayakumar, A simple model for viscosity of powder injection moulding mixes with binder content above powder critical binder volume concentration, J. Eur. Ceram. Soc. 20 (2000) 2183–2190. https://doi.org/10.1016/S0955-2219(00)00096-0.

[87] A. Medina Peschiutta, M. Just, R. Useldinger, J. Baller, Assessing critical binder volume concentration using uniaxial die pressing: An alternative approach, Powder Technol. 443 (2024) 119968. https://doi.org/10.1016/j.powtec.2024.119968.

[88] A. Boursier, G. Grimaldi d'Esdra, E. Lintingre, C. Frétigny, F. Lequeux, L. Talini, Cold compression of ceramic spray-dried granules: Role of the spatial distribution of the binder, Ceram. Int. 46 (2020) 9680–9690. https://doi.org/10.1016/j.ceramint.2019.12.235.

[89] D. Yarnton, T.J. Davies, The effect of lubrication on the pressing of metal powder compacts, Powder Metall. 6 (1963) 1–22. https://doi.org/10.1179/pom.1963.6.11.001.

[90] J. Zheng, J.S. Reed, Particle and Granule Parameters Affecting Compaction Efficiency in Dry Pressing, J. Am. Ceram. Soc. 458 (1988) 456–458. https://doi.org/10.1111/j.1151-2916.1988.tb07546.x.

[91] E. Klar, P.K. Samal, Compacting and Shaping, in: Powder Metall. Stainl. Steels, ASM International, 2007: pp. 39–58. https://doi.org/10.31399/asm.tb.pmsspmp.t52000039.

[92] G. Lumay, F. Boschini, K. Traina, S. Bontempi, J.C. Remy, R. Cloots, N. Vandewalle, Measuring the flowing properties of powders and grains, Powder Technol. 224 (2012) 19–27. https://doi.org/10.1016/j.powtec.2012.02.015.